

Old Dominion University

ODU Digital Commons

Mechanical & Aerospace Engineering Theses & Dissertations

Mechanical & Aerospace Engineering

Fall 2023

Fabrication of Smooth SAC305 Thin Films via Magnetron Sputtering and Evaluations of Microstructure, Creep, and Electrical Resistivity

Manish Ojha

Old Dominion University, manissh23@gmail.com

Follow this and additional works at: https://digitalcommons.odu.edu/mae_etds



Part of the [Electrical and Computer Engineering Commons](#), [Materials Science and Engineering Commons](#), and the [Mechanical Engineering Commons](#)

Recommended Citation

Ojha, Manish. "Fabrication of Smooth SAC305 Thin Films via Magnetron Sputtering and Evaluations of Microstructure, Creep, and Electrical Resistivity" (2023). Doctor of Philosophy (PhD), Dissertation, Mechanical & Aerospace Engineering, Old Dominion University, DOI: 10.25777/ht3z-5a85 https://digitalcommons.odu.edu/mae_etds/373

This Dissertation is brought to you for free and open access by the Mechanical & Aerospace Engineering at ODU Digital Commons. It has been accepted for inclusion in Mechanical & Aerospace Engineering Theses & Dissertations by an authorized administrator of ODU Digital Commons. For more information, please contact digitalcommons@odu.edu.

**FABRICATION OF SMOOTH SAC305 THIN FILMS VIA MAGNETRON
SPUTTERING AND EVALUATIONS OF MICROSTRUCTURE, CREEP, AND
ELECTRICAL RESISTIVITY**

by

Manish Ojha
B.E. August 2016, Kurukshetra University
M.Sc. April 2020, Grand Valley State University

A Dissertation Submitted to the Faculty of
Old Dominion University in Partial Fulfillment of the
Requirements for the Degree of

DOCTOR OF PHILOSOPHY
MECHANICAL ENGINEERING
OLD DOMINION UNIVERSITY
December 2023

Approved by:

A. A. Elmustafa (Director)

Helmut Baumgart (Member)

Oleksandr Kravchenko (Member)

Miltos Kotinis (Member)

ABSTRACT

FABRICATION OF SMOOTH SAC305 THIN FILMS VIA MAGNETRON SPUTTERING AND EVALUATIONS OF MICROSTRUCTURE, CREEP, AND ELECTRICAL RESISTIVITY

Manish Ojha
Old Dominion University, 2023
Director: Dr. A.A. Elmustafa

SAC305 (96.5% Sn-3% Ag-0.5% Cu) is the leading alternative to the traditional Sn-Pb solder eutectic alloy owing to its low melting temperature, better compatibility with other components, and excellent mechanical/structural properties. In the realm of modern electronics, where devices are increasingly miniaturized, the design and characterization of thin solder joints become paramount. The orientation and size of the grains within the solder can influence its ability to withstand mechanical stresses. However, research on SAC thin films remains sparse, and these films present unique challenges and characteristics compared to their bulk counterparts, influenced by factors like interfaces, stresses, thickness, microstructure, and the nature of the underlying substrates.

This study investigated a method to improve the surface morphology of SAC305 thin films by depositing on various substrates, varying annealing processes modulating the substrate, and various magnetron sputtering parameters to produce smooth and continuous SAC305 thin film. A comprehensive annealing treatment was carried out in a vacuum furnace to investigate the surface morphology of the films. Various deposition parameters were tested using DC and RF power sources at different pressures and powers. This study investigates the surface morphology of SAC305 thin films deposited on four substrates: Silicon, Gallium Arsenide, Sapphire, and Glass. The most optimal surface morphology, with an average grain size of $\sim 1 \mu\text{m}$

and a thickness of $\sim 2 \mu\text{m}$, was accomplished at a pressure of 2.4 mTorr and 200-watt power deposited on Si substrate. After polishing, a uniform thickness of 1500 nm with a mean roughness (R_a) of 14.9 nm was obtained. The samples contained polycrystalline β -Sn grains at (200) diffraction planes with a preferred orientation 2θ of 30.70° . However, the XRD pattern did not indicate any Ag peaks; weak peaks of Ag_3Sn were observed at 2θ of 37.60° and 39.59° , corresponding to diffraction planes (020) and (211), respectively. The electrical resistivity of the SAC305 thin film deposited on the SiO_2 substrate and of the bulk SAC305 samples were measured as $19.6 \mu\Omega\cdot\text{cm}$ and $13.7 \mu\Omega\cdot\text{cm}$, respectively. The reported average (m) value $\approx 0.10 \pm 0.02$ of SAC305 thin films and bulk sample agrees with the previous literature data.

Copyright, 2023, by Manish Ojha, All Rights Reserved.

This dissertation is dedicated to my parents, Madhav P. Ojha & Mina Ojha, and my wife,
Tamanna Pandey.

ACKNOWLEDGMENTS

I extend my deepest gratitude to my dissertation advisor, Dr. Abdelmageed Elmustafa, for his unwavering support, trust, and dedication throughout this journey. His guidance and mentorship have been invaluable to my achievements. My sincere thanks go to my dissertation committee members: Dr. Helmut Baumgart, Dr. Oleksandr Kravchenko, and Dr. Miltos Kotinis. I am also indebted to my co-authors, Dr. Yousuf Mohammed and Dr. DS Stone, for their invaluable insights and suggestions. My appreciation extends to Dr. Wei Cao and Olga Trofimova for their supervision of various characterization techniques. I am fortunate to have worked alongside my colleagues at the ODU/ARC Nanoindentation Lab, and I cherish the camaraderie we shared. My heartfelt thanks go to my parents and extended family for their unwavering support throughout my academic journey. Lastly, my deepest gratitude is reserved for my wife, Tamanna Pandey, whose continuous support, understanding, and love have been my pillars of strength.

NOMENCLATURE

nm	nanometer
$\mu\Omega$	Micro-ohm
σ	Electrical conductivity
mN	Millinewton
m_H	strain rate sensitivity of the hardness
H	Hardness
$\dot{\epsilon}$	Strain rate
SAC305	96.5% Sn-3% Ag-0.5% Cu
Ra	Mean roughness
Rq	Root-mean-square roughness
CVD	Chemical vapor deposition
PVD	Physical vapor deposition
DC	Direct current
RF	Radio frequency
FE-SEM	Field emission-scanning electron microscope
XRD	X-ray diffraction
AFM	Atomic Force Microscope
FPP	Four-point probe
CSM	Continuous stiffness method

TABLE OF CONTENTS

	Page
LIST OF TABLES	xii
LIST OF FIGURES	xiii
Chapter	
1. INTRODUCTION	1
1.1 Background	1
1.2 Problem Statement	3
1.3 Objectives and Significance	4
1.4 Scope and Limitations	6
2. LITERATURE REVIEW	8
2.1 Overview of Soldering	8
2.1.1 Electronic Packaging	8
2.1.2 Soldering	9
2.2 Composition and Properties of Pb-Free Solder	9
2.2.1 Mechanical Properties of a Solder	11
2.2.1.1 Tensile Properties	12
2.2.1.2 Shear Strength	13
2.2.1.3 Creep Properties	14
2.2.1.4 Fatigue	14
2.2.2 Electrical Properties	15
2.3 Previous Studies on SAC Solder	16

2.4	Comparison of Thin Film and Bulk Materials	19
3.	REVIEW OF FABRICATION AND CHARACTERIZATION TECHNIQUE	22
3.1	Magnetron Sputtering.....	22
3.2	Field Emission-Scanning Electron Microscope (FE-SEM)	27
3.3	X-ray Diffraction (XRD).....	29
3.4	Atomic Force Microscope (AFM).....	31
3.5	Nanoindentation	33
3.6	Four-Point Probe (FPP).....	37
4.	FABRICATION OF SMOOTH SAC305 THIN FILM VIA MAGNETRON SPUTTERING	40
4.1	Introduction	40
4.2	Experimental Setup	42
4.2.1	Wafer Cleaning.....	42
4.2.2	Magnetron Sputtering	43
4.2.3	Annealing.....	47
4.2.4	FE-SEM	47
4.3	Results and Discussion.....	49
4.3.1	Substrate Temperature	49
4.3.2	Annealing.....	50
4.3.3	Sputtering Power.....	52
4.3.4	Sputtering Pressure	57
4.4	Conclusion.....	61
5.	FABRICATION AND CHARACTERIZATION OF MAGNETRON SPUTTERED SAC305 THIN FILMS	63

Chapter	Page
5.1 Introduction	63
5.2 Experimental Setup	65
5.2.1 Substrate.....	65
5.2.2 Polishing	65
5.2.3 FE-SEM and EDS	66
5.2.4 XRD	67
5.2.5 AFM.....	68
5.3 Results and Discussion.....	69
5.3.1 FE-SEM	69
5.3.2 XRD	70
5.3.3 Polishing.....	73
5.3.4 AFM.....	76
5.4 Conclusion.....	77
6. MECHANICAL AND ELECTRICAL CHARACTERIZATION OF MAGNETRON SPUTTERED SAC305 THIN FILMS	79
6.1 Introduction	79
6.2 Experimental Details	79
6.2.1 Nanoindentation.....	79
6.2.2 Four-Point Probe.....	81
6.3 Experimental Results.....	83
6.3.1 Nanoindentation.....	83
6.3.2 Four-Point Probe.....	94
6.4 Conclusion.....	95

Chapter	Page
7.CONCLUSION.....	96
7.1 Conclusion.....	96
7.2 Future Work.....	98
REFERENCES	99
APPENDIX.....	118
A. COPYRIGHT PERMISSIONS	118
VITA.....	120

LIST OF TABLES

Table	Page
2.1 Tensile and Shear Properties of Pb-Free Solders.....	13
2.2 Resistivity Values for Some Pb-Free Solders at Room Temperature.....	16
4.1 Deposition of SAC305 Thin Film at Various Pressures and Power	46
4.2 Annealing Process of SAC 305 Thin Film at Various Temperatures.....	47
6.1 Creep Experiments for Bulk and Thin Films.....	85
6.2 Strain Rate Sensitivity of the Hardness Results.....	94

LIST OF FIGURES

Figure	Page
1.1 Comparison of Sizes of Semiconductor Manufacturing Process Nodes with Some Microscopic Objects and Visible Light Wavelengths. Reproduction with Permission [20]	6
3.2 Schematic Diagram of Magnetron Sputtering System. Reproduced with Permission [76].....	25
3.3 Schematic Diagram of Scanning Electron Microscopy. Reproduced with Permission [81].....	29
3.4 Schematic Diagram of X-ray Diffraction. Reproduced with Permission [87].....	Error!
Bookmark not defined.	
3.5 Schematic Diagram of Atomic Force Microscope. Reproduced with Permission [89]...	Error!
Bookmark not defined.	
3.6 Schematic of a Load-Displacement Curve for Nanoindentation. Reproduced with Permission [101].....	37
4.1 Image of ATC Orion-8 Sputtering Deposition System.....	44
4.2 Hitachi S-4700 Field Emission Scanning Electron Microscope (FE-SEM).....	48
4.3 SAC 305 Deposited at (a) Room Temperature and (b) 100°C.	49
4.4 FE-SEM Images of the Thin SAC305 Films Annealed at (a) 180°C for 1 hr., (b) 180°C for 3 hr., (c) 200°C for 1 hr., (d) 200°C for 3 hr., (e) 210°C for 1 hr., (f) 210°C for 3 hr., (g) 220°C for 1 hr.	51
4.5 Investigating Variable Power Effects in Magnetron Sputtering Deposited SAC305 Thin Films at 3 mTorr Pressure and Various Power.	Error! Bookmark not defined.

4.6 FE-SEM Images of the Thin SAC305 Films Surface Area Deposited at 200W through DC and RF Power Source on Si Substrate at Various Pressure.	56
Figure	Page
4.7 Investigating Variable Pressure Effects in Magnetron Sputtering Deposited SAC305 Thin Films at 200-Watt Power and Various Pressures.....	58
4.8 FE-SEM Images of the Thin SAC305 Film Surface Area Deposited at 200W through DC and RF Power Source on Si Substrate at Various Pressures.....	60
5.1 Allied High-Tech Multi-Prep Polishing System and Automatic Fluid Dispenser.....	66
5.2 Image of XRD (Miniflex II, Rigaku, Japan).....	68
5.3 Atomic Force Microscope (AFM)	69
5.4 FE-SEM Images of the Thin SAC305 Film’s Surface Area Deposited at 2.3 mTorr Pressure through 200W RF Power on Various Substrates.....	70
5.5 (a) XRD Plot of the Thin SAC305 Films on Various Substrates. (b) Enlarged Plots.	72
5.6 FE-SEM Image SAC305 Thin Film Deposited at 200W RF Power and 2.4 Mtorr Pressure on Si Substrate. (a) the Surface Area Before Polishing. (b) Cross Section Area Before Polishing. (c) Surface Area After Polishing for 2 mins. (d) Cross Section Area After Polishing for 2 mins. Reproduced with Permission from Manish Ojha, Yousuf Mohammed, Donald Stone, and A.A. Elmustafa, JVST B 41 (5), 10.1116/6.0002949, (2023). Copyright 2023 American Vacuum Society.....	74
5.7 The EDS Spectral Analysis for the Elemental Composition of Polished SAC305 Thin Film After Ultrasonic Cleaning. (a) Mapping Surface Area, (b) Elemental Distribution of Sn, (c) Elemental Distribution of Ag, (d) Elemental Distribution of Cu. Reproduced with Permission	

from Manish Ojha, Yousuf Mohammed, Donald Stone, and A.A. Elmustafa, JVST B 41 (5), 10.1116/6.0002949, (2023). Copyright 2023 American Vacuum Society..... 76

Figure	Page
5.8 AFM Images of (30 μ m \times 30 μ m) Scan Size of Polished SAC305 Films on Si Substrate. Reproduced with Permission from Manish Ojha, Yousuf Mohammed, Donald Stone, and A.A. Elmustafa, JVST B 41 (5), 10.1116/6.0002949, (2023). Copyright 2023 American Vacuum Society.....	77
6.1 Nanoindenter XP Equipped with a Three-Sided Diamond Berkovich Probe.....	81
6.3 SAC305 Thin Film Log (H) Vs. Log ϵ Plot.....	86
6.4 Load vs. Total Depth of Penetration in a Creep Experiment for Bulk SAC305 Samples. (a) The Loading Rate (LR) is Varied Between 0.1 mN/s and 40 mN/s While the Unloading Time (ULT) and the Peak Hold Time (PHT) are Held Constant. (b) The LR and ULT are Held Constant While the PHT is Varied Between 10 and 70 sec. (c) The PHT was Set at 10 sec for a Strain Rate of 0.05 1/s. Reproduced with Permission from Manish Ojha, Yousuf Mohammed, Donald Stone, and A.A. Elmustafa, JVST B 41 (5), 10.1116/6.0002949, (2023).....	88
6.5 Load vs. Total Depth of Penetration in a CSM and Creep Experiments for Thin SAC305 Films. Reproduced with Permission from Manish Ojha, Yousuf Mohammed, Donald Stone, and A.A. Elmustafa, JVST B 41 (5), 10.1116/6.0002949, (2023). Error! Bookmark not defined.	
6.6 (a) Displacement into Surface vs. Time. (b) Load on Samples vs. Time. Reproduced with Permission from Manish Ojha, Yousuf Mohammed, Donald Stone, and A.A. Elmustafa, JVST B 41 (5), 10.1116/6.0002949, (2023).....	91

6.7 Strain Rate of the Indentation Hardness in Nanoindentation Creep and Conventional Testing of SAC305 Bulk and Thin Film Samples. Reproduced with Permission from Manish Ojha, Yousuf Mohammed, Donald Stone, and A.A. Elmustafa, JVST B 41 (5), 10.1116/6.0002949, (2023)	93
--	----

CHAPTER 1

INTRODUCTION

1.1 Background

Eutectic alloys, known for their low melting temperature and homogeneous properties, have a long history of use. The term eutectic originates from the Greek and means "easily melted." These alloys undergo a reversible transformation in which a liquid transitions into multiple solid phases at a specific temperature during cooling. This transformation occurs in systems with various elements. Eutectic alloys, such as Tin-Lead (Sn-Pb) solder, solidify entirely at a single temperature, resulting in a uniform microstructure without mushy zones or micro-shrinkage voids.

In the electronics industry, Sn-Pb eutectic solder alloy is widely used to connect electronic components to printed circuit boards (PCBs), which provide structural support and interconnections for electronic devices. The thermal stability of PCBs imposes a processing temperature limit of around 240 °C to prevent epoxy breakdown and excessive stress. The low eutectic temperature of Sn-Pb solder (183 °C) makes it an excellent choice for minimizing processing temperatures during electronic assembly. In addition, Sn-Pb solder exhibits excellent wetting behavior, adequate mechanical strength, and good electrical conductivity [1].

The environmental and health hazards associated with Pb have instigated a global movement towards lead-free electronics manufacturing. Concerns over the environmental impact of Pb gained prominence in the late 20th century, as studies revealed the harmful effects of Pb on the ecosystem and human health.

Pb is a toxic heavy metal that can contaminate soil and water, posing risks to wildlife and human populations. In humans, exposure to lead can result in various health problems, including neurotoxic effects, kidney damage, and developmental issues in children [2]. The Restriction of Hazardous Substances (RoHS) directive, implemented by the European Union in 2006, has supported lead-free electronics. The directive prohibits using certain hazardous materials, including lead, in electronic and electrical equipment (EEE) sold within the European Union [3]. The RoHS directive has been influential globally, prompting similar regulations in countries such as China (China RoHS) and South Korea (Korea RoHS).

Due to environmental and toxicological concerns, electronic industries are progressing towards lead-free solders. This shift has spurred an extensive search for Pb-free solder alloys in recent years, identifying several promising candidates suitable for various soldering applications [4-5]. The leading alternatives to the traditional Sn-Pb solder have been identified as the Sn-Ag-Cu eutectic and the Sn-Cu eutectic owing to their low melting temperature [6], better compatibility with other components [7-9], and excellent mechanical/structural properties [10]. Academic institutions and industry consortia across Europe, Japan, and the United States have recognized and deemed these alternatives suitable. Notably, the SAC305 (96.5% Sn-3% Ag-0.5% Cu) alloy, with its melting point of 217 °C, presents a distinct advantage over most Sn-Cu alloys, with a melting point of 227 °C. Furthermore, SAC305 demonstrates performance comparable to the high-Silver Tin-Silver-Copper (Sn-Ag-Cu) eutectic, albeit at a reduced cost. Consequently, following the Institute of Printed Circuit's endorsement of SAC305 as the preferred Pb-free alloy for the electronics sector, numerous enterprises in the United States have chosen SAC305 as the primary alloy for products intended for the European Union market. This

pivotal endorsement has subsequently positioned SAC305 as the preferred choice in the industry, overshadowing both the Sn-Cu and other Sn-Ag-Cu eutectics.

1.2 Problem Statement

One of the most significant challenges in microelectronic packaging involving the transition to lead-free solders has been the reliability of interconnect technology. Structural designs such as materials, integrated circuit (IC) component size and shape, electrical conductivity, and mechanical properties appeal to the demand for efficient current distribution through the chip package [11-12]. Solder joints in electronic packages are frequently exposed to a thermal cycling environment. Such exposures can occur in real-life applications and accelerated thermal cycling tests used to characterize fatigue behavior. Because of temperature variations and coefficient of thermal expansion mismatches of the assembly materials, cycling temperatures lead to deformation accumulation and evolving material properties in the solder joints. This deformation eventually initiates cracks and subsequent crack growth and failure. Therefore, a thorough understanding of solder interconnection failure mechanisms requires a focus on in-depth microstructural analysis of solder interconnections, including monitoring changes during operation and the solder's mechanical properties. Several studies have discussed mechanical and electrical properties such as tensile strength, elastic modulus, Poisson's ratio, microstructural analysis, creep properties, and conductivity of SAC305 bulk solder materials [13-17].

However, limited research exists concerning SAC305 thin films, which differ significantly from bulk materials due to interfaces, stresses, thickness, microstructure, and underlying substrates. The microelectronics industry's shift towards miniaturization has intensified the emphasis on micro-soldering. This transition has heightened concerns about the

reliability of solder joints in compact microelectronic devices [18-19]. Consequently, analyzing the microstructural, electrical, and mechanical attributes of SAC305 thin films is crucial for enhancing the durability and longevity of these solder joints.

1.3 Objectives and Significance

Designing and characterizing thin solder joints is crucial in modern electronics, especially as devices become smaller and more compact. The electronics industry's drive towards miniaturization has led to a surge in demand for smaller components and tighter device architectures. This trend is evident in the evolution of consumer electronics, where devices such as smartphones and wearables have undergone significant size reductions over the past few decades. This trend towards device miniaturization is guided by Moore's Law, formulated by Gordon Moore. This principle asserts that the size of semiconductor manufacturing process nodes diminishes by a factor of one-tenth every decade (Figure 1.1) [20]. While this law is rooted in historical observations, it also provides projected trends. However, as devices continue to miniaturize, the associated developmental costs escalate, presenting various challenges. Such increased expenditures can potentially impede innovation and have broader economic implications. Some experts, including Moore, anticipate that the law may become less relevant due to emerging physical constraints, with predictions suggesting its obsolescence by 2025. In response, the industry is investigating new and advanced chip designs.

A notable limitation of Moore's Law and similar models is their inability to forecast solder joints' longevity in electronic devices accurately. Thin solder joints are integral to this miniaturization process. They facilitate the efficient connection of components in confined spaces without compromising device functionality or reliability. Lau (1997) emphasized the importance of solder joint reliability in various assemblies, including ball grid arrays (BGAs) and

chip scale packages (CSPs) [21]. These assemblies often utilize thin solder joints to maintain electrical connectivity in compact configurations. The microstructure of these solder joints plays a pivotal role in determining their mechanical properties. The grain structure evolution in solder joints, especially in eutectic compositions, profoundly impacts the joint's mechanical strength and fatigue resistance. The orientation and size of the grains within the solder can influence its ability to withstand mechanical stresses, especially in devices where physical space is at a premium.

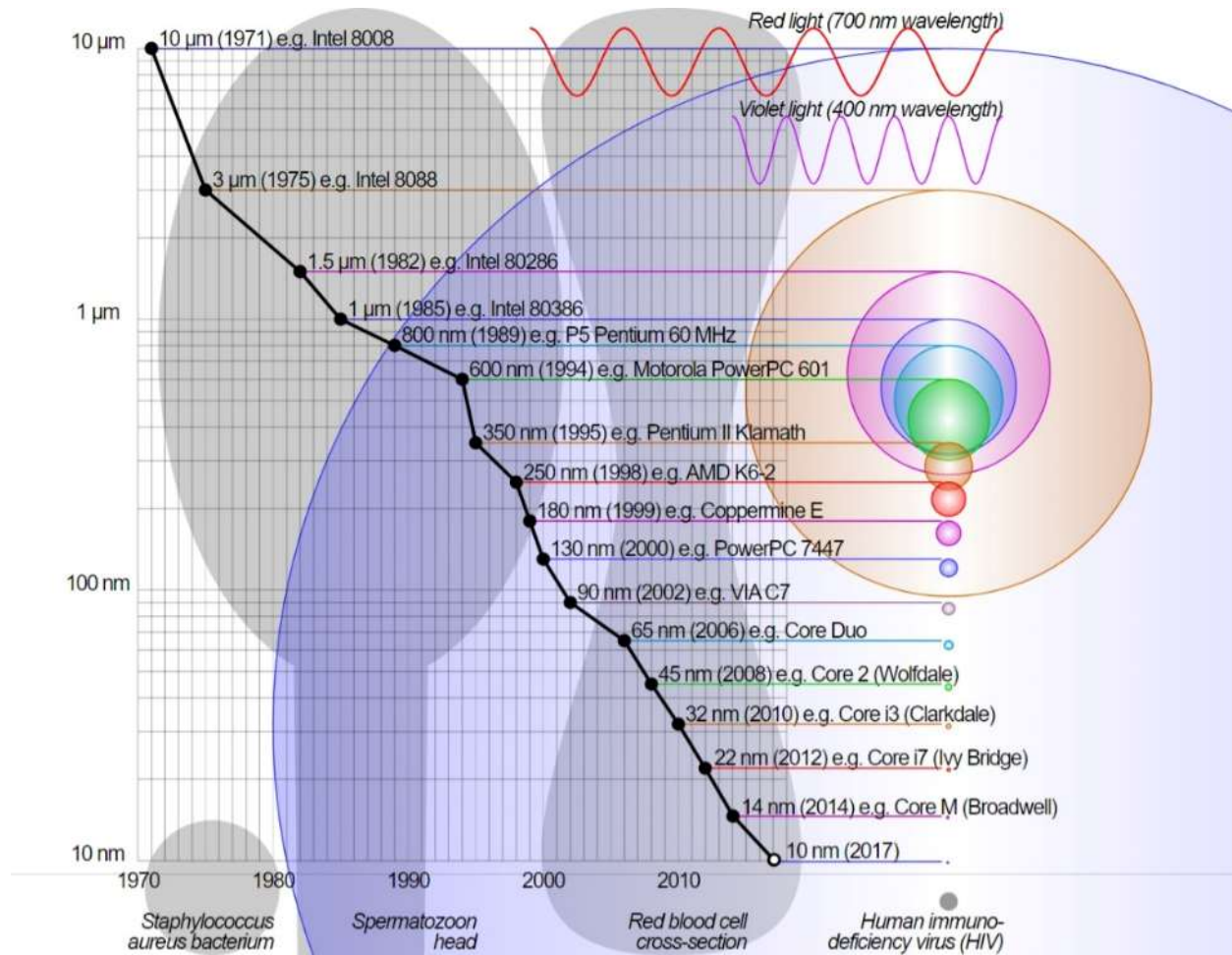


Figure 1.1 Comparison of Sizes of Semiconductor Manufacturing Process Nodes with Some Microscopic Objects and Visible Light Wavelengths. Reproduction with Permission [20]

1.4 Scope and Limitations

In the rapidly evolving field of electronics manufacturing, solder joints' integrity and performance are paramount. With the increasing demand for miniaturized electronic components, the focus on thin film solder joints, particularly those of the SAC305 alloy, has intensified. The primary objective of this research is to investigate the intricate microstructural evolution of SAC305 when it is formed as a thin film solder joint. Concurrently, the study aims

to examine the phase distribution, grain orientation, and the formation of intermetallic compounds (IMCs) within these joints, providing a comprehensive understanding of their internal dynamics. From a mechanical perspective, the study evaluated the inherent properties of these joints, focusing on their mechanical strength, Young's modulus, creep behavior, and the strain rate sensitivity (m) of their hardness. From an electrical perspective, the study evaluated the SAC305 thin film resistivity and bulk solder joints. The research compared the mechanical and electrical properties of thin films with those of bulk materials. Furthermore, recognizing the need for continual improvement in manufacturing processes, this research endeavored to innovate methodologies and techniques. These techniques could optimize the formation and overall performance of the SAC305 thin film solder joints.

To accurately measure the mechanical properties using nanoindentation and electrical resistivity using a four-point probe, the indents on the film should be less than one-third of its thickness. However, assessing the electrical and mechanical properties of SAC305 with only a few nanometers in thickness was challenging due to the substrate's influence on nanofilms and the probe's diameter.

CHAPTER 2

LITERATURE REVIEW

2.1 Overview of Soldering

2.1.1 *Electronic Packaging*

Solder is not used at the silicon IC level, representing the finest assembly level. Instead, ICs are typically attached to a carrier module before mounting on a PCB. The most prevalent method for this attachment is wire bonding, where the fine gold wire connects the chip to the module. However, with technological advancements and the need for increased input/output (I/O) density, alternative methods such as flip-chip attachment have emerged. This method connects tiny solder spheres over the chip's entire area, enhancing I/O density. In the wire bond technique, the die is positioned facing upwards and connected to the package using wires.

Conversely, the flip-chip is oriented downwards and is commonly connected using solder bumps, similar to the larger bumps used to attach BGA packages to the PCB (Figure 2.1) [22]. Unlike wire bonding, which connects one by one, flip-chip connects simultaneously. However, the application is challenging due to issues such as brittle joints from IMC formation. Two primary soldering processes at the board-level assembly are wave soldering and reflow processing. Wave soldering involves passing a PCB assembly over a solder wave, while reflow soldering uses solder paste to create joints. Reflow processing, used for surface mount technology (SMT) joints, offers advantages such as higher I/O density and dual-sided component placement on PCBs. Despite SMT joints facing more mechanical stress, their increased I/O density has made them the preferred board-level assembly method [23]. This study seeks to investigate solders, such as SAC305, for their suitability in reflow processing.

2.1.2 Soldering

Solder has been utilized for about 4,000 years, with the earliest known use traced back to Egypt in 3600 BC. Sn-Pb eutectic solders' efficiency, affordability, and reliability have made them popular since Roman times. Despite the extensive history of soldering, challenges in metallurgical bonding persist today. Soldering is crucial in microelectronics, ensuring electrical, thermal, and mechanical connections. The integrity of these solder joints is vital for the performance and reliability of electronic devices. However, there has been a concerning rise in solder-related failures over the past three decades. This increase can be attributed to technological advancements, especially in microelectronics, space exploration, and consumer electronics. These advancements have led to a surge in solder joints produced annually. Moreover, electronics are now used in more demanding environments, such as space, military, and automotive sectors, subjecting solder to extreme thermal and mechanical stresses. Traditional solder methods are struggling to meet these demands. Moreover, the electronic industry foresees growth in these challenging sectors. Recent progress in the microelectronics soldering field has been made, but the search for environmentally friendly solders and reducing joint failures remains paramount.

2.2 Composition and Properties of Pb-Free Solder

Numerous Pb-free solder alloys such as Sn-Au, Sn-In, Sn-Ag, and Sn-Bi have been documented in the literature, ranging from binary to quaternary compositions. Sn emerges as the dominant element in many of these alloys, followed closely by Indium (In) and Bismuth (Bi). Other elements in the mix include Zinc (Zn), Silver (Ag), Antimony (Sb), Copper (Cu), Magnesium (Mg), and a trace amount of Pb. Some of these alloys are merely variations of a

foundational composition. For instance, multiple Sn \pm 10Bi composition versions are differentiated by the presence or absence of elements such as Cu, Sb, and Zn.

Sn has become a primary ingredient in solder alloys for electronics due to its ability to adhere and spread across various materials with gentle fluxes. It solidifies at 231.8 °C and has two distinct forms: white Sn, stable at ambient temperatures, and gray Sn, stable below 138 °C [24]. A shift from white to gray tin, known as "tin pest," can cause the tin to expand and crack, especially in colder environments or devices that frequently change temperatures due to thermal cycling at 35 to 75 °C [25]. This expansion property of Sn is due to its unique crystal structure. Specific elements such as Sb, Bi, and Pb have been added to combat the issues of tin pests, though the exact science behind their effectiveness is still under study. In the context of the Sn-Pb mix, it is uncertain whether Pb helps prevent the tin pest or adjusts to its expansion. Another challenge with tin is its tendency to produce whisker-like growths, which can lead to electrical issues, though lead has been found to curb this growth [26].

The Sn-9Zn alloy is a promising substitute due to its melting point of 198.8 °C , close to the tin-lead eutectic point. This alloy has a dual-phase eutectic structure: a tetragonal Sn matrix and a hexagonal Zn phase with minimal tin. Once solidified, it displays a combination of large grains and a consistent two-phase eutectic pattern. This alloy's structure features layers of Sn-rich and Zn-rich phases. Notably, Sn and Zn combine with Cu in this system, forming specific metallic compounds [27].

In-Sn solders are preferred for SMT due to their lower melting point and reduced gold scavenging compared to tin-lead solders. The most common composition for SMT is In-48Sn, with a eutectic point at 117.8 °C . This alloy forms two distinct phases: indium-dominant tetragonal and tin-dominant hexagonal phases [24]. This solder exhibits layered patterns when

applied to a copper base, with the tin phase showing uniform grains. On a nickel base, the structure appears more consistent. However, over time, the solder's structure on a copper base can show significant changes [28].

The Sn-Ag binary system has a eutectic point at Sn-3.5Ag with a melting temperature of 221.8 °C . Its structure is characterized by tin and the metallic compound Ag_3Sn , appearing as slender fragments. The solidified structure of the Sn-3.5Ag eutectic binary features a predominant β -Sn phase, interspersed with dendritic formations and areas enriched with Ag_3Sn particles set within the β -Sn framework [29]. Similar to the Sn-0.07Cu variant, this solder might be susceptible to forming whisker-like growths due to its tin content, though specific data on this aspect for Sn-Ag is lacking [30].

The Sn-Cu alloy has a specific eutectic composition and solidifies at 227 °C , forming Cu_6Sn_5 intermetallic hollow rods. While there is limited data on its properties, its high tin content could lead to whisker growth or gray tin transformation. The impact of Cu on these processes remains uncertain [31].

2.2.1 *Mechanical Properties of a Solder*

Electronic devices experience mechanical stresses on their solder connections due to differing thermal expansion coefficients between components and boards. For instance, boards expand more than components as temperatures rise, causing shear strain on solder ball connections. This strain is exacerbated by frequent temperature changes, leading to cyclic shear stresses. The solder's shear modulus determines the strain, and its fatigue life indicates how many cycles it can endure before failure. Solder joints can also face tensile stress, especially during product handling or testing. Solder joints undergo cyclic loading in environments with vibrations, making their fatigue life crucial. The constant thermal expansion during device

operation can also cause static loading on solder connections, making them prone to creep at elevated temperatures.

2.2.1.1 Tensile Properties

Table 2.1 summarizes data on the elastic modulus, yield strength, ultimate tensile strength (UTS), and ductility of various alloys. The elastic modulus ranges from 23.6 GPa for In-48Sn to 50.6 GPa for Sn-3.5Ag-0.5Cu. Alloys with lower elastic moduli are favored as they produce less stress for a given strain. Strength and ductility are influenced by microstructure, strain rate, chemical composition, and thermal history. For instance, the UTS of Sn-3.5Ag varies with strain rate and aging. Strength values after aging are crucial for assessing solder durability. The UTS of solders is generally between 20-50 MPa. Still, it is affected by temperature, with some alloys experiencing significant strength loss at higher temperatures, making them prone to deformation and fatigue.

Table 2.1 Tensile and Shear Properties of Pb-Free Solders

Solder Composition	Elastic modulus (GPa)	Yield Strength (MPa)	Ultimate Tensile Strength (MPa)	Shear modulus (GPa)	References
Sn-37Pb	39		52	12	37, 40, & 41
Bi-42Sn	42	41		15.8	37, & 42
In-48Sn	23.6			8.87	37, & 42
Sn-20In-2.8Ag	36.8		46.9	14.5	43, 44, & 43
Sn-5Sb	50		20		45, & 40
Sn-3.5Ag	50	48	42.8	18.8	37, 37, 44, & 46
Sn-3.5Ag-0.5Cu	50.6	51	43		47, 47, & 48

2.2.1.2 Shear Strength

Solder joints in microelectronics often undergo shear loading. Shear strength is the maximum force a material can withstand when subjected to a force that tries to slide its layers apart. The shear strength of these alloys is influenced by strain rate and temperature, with temperature having a more pronounced effect. Notably, higher temperatures significantly drop in shear strength, often between 40-50% and 75% for the In-48Sn alloy. This temperature and strain rate sensitivity is due to the alloys' inherent properties, allowing diffusion and creep to occur, impacting their strength and ductility. The shear modulus (G) can be determined using Eq. (1) when the elastic modulus (E) and Poisson's ratio (ν) are provided [32].

$$G = \frac{E}{2(1+\nu)} \quad (1)$$

2.2.1.3 Creep Properties

Creep refers to a material's tendency to deform over time under a sustained load, especially at high temperatures. This deformation can be due to grain boundary sliding and vacancy diffusion [33]. Creep becomes crucial for materials when temperatures exceed half their melting point [34]. Creep behavior is categorized into primary, secondary, and tertiary phases. The secondary phase is particularly significant due to its consistent behavior. The creep equation for this phase involves variables, including shear strain rate, stress, and activation energy, which are influenced by the material's microstructure. The solder joints made of Sn-Bi displayed better resistance to creep at 658 °C compared to Pb-Sn joints created in the same condition [35]. Notably, the Sn-3.5Ag alloy exhibited considerably more strain before test failure than the eutectic Sn-Pb [36]. In the steady-state secondary creep region, Eq. (2) presents the most straightforward form of the creep equation [37].

$$\frac{d\gamma}{dt} = A\tau^n \exp\left(\frac{\Delta H}{RT}\right) \quad (2)$$

where $\frac{d\gamma}{dt}$ is the shear strain rate, τ is the shear stress, n is the stress exponent, ΔH is the activation energy, A is the microstructure-dependent constant, R is the universal gas constant, and T is the absolute temperature (K).

2.2.1.4 Fatigue

Fatigue measures a material's resistance to failure from cyclic loading. There are two types: isothermal fatigue, which happens at a steady temperature, and thermal fatigue, resulting from temperature changes due to materials with different thermal expansion rates. Fatigue in solder joints leads to crack initiation and crack propagation. The fatigue life is measured by the stress cycles tolerated before cracks begin and propagate. Fatigue failure can occur even if the stress is below the material's yield point because of microstructural defects that become crack

starting points. Enhancing fatigue life involves improving resistance to these crack initiation and propagation. Both fatigue and creep play roles in solder alloy failures. Recent research indicates that select Pb-free solders surpass the performance of conventional Sn-Pb solders under certain conditions. For instance, Sn-Bi alloys excel in particular thermal cycling scenarios [38]. Marshall and Walter (1987) tested Cu pins soldered and exposed to varying temperatures. Their findings revealed that solders enriched with Ag outperformed Sn-Pb and In-Sn variants [39]. Moreover, practical tests demonstrate that alloys with Ag content offer enhanced fatigue resistance.

2.2.2 *Electrical Properties*

In functioning microelectronics devices, solder acts as an electrical link, channeling all electrical currents to and from a silicon device. The solder's resistivity should be low for effective electrical connectivity, ensuring smooth current flow without excessive heating. As devices become smaller, solder's electrical resistivity becomes increasingly vital. Solder joints might heat up to 125 °C due to current flow and heat from the silicon device, making the temperature coefficient of resistivity crucial; ideally, it should be near zero up to this temperature. Generally, solder's resistivity in electronics is low, not significantly affecting circuit functionality. However, resistivity can vary based on grain size and dislocation density. For example, the Bi alloy exhibits greater resistivity than others, such as Sn. This resistivity is attributed to the fact that Bi has high resistivity (115 $\mu\Omega$ cm) in contrast to Sn (10.1 $\mu\Omega$ cm). Limited data exists on resistivity under AC conditions, but as electronic product speeds rise, AC impedance, especially at high frequencies, becomes more critical than DC resistivity. Table 2.2 presents the resistivity values of frequently used solders for microelectronics applications, measured at room temperature [24].

Table 2.2 Resistivity Values for Some Pb-Free Solders at Room
temperature

Solder alloy	Resistivity ($\mu\Omega$ cm)
63Sn-37Pb	14.4
58Bi-42Sn	34.4
48Sn-52In	14.7
96.5Sn-3.5Ag	12.3
96.5Sn-3Ag-0.5Cu	13
Ag	1.59
Cu	1.73

2.3 Previous Studies on SAC Solder

Environmental concerns and market pressure drive the shift from Sn-Pb solders to Pb-free solders in electronic systems [2-3]. The transition offers an opportunity to enhance joint reliability, especially in high-stress and high-temperature environments. These alternatives aim to surpass the properties of Sn-Pb solders, especially as the demand for lightweight, high-speed, and multifunctional portable electronics grows. Reliability in terms of thermal cycling and drop performance is crucial for these devices. Sn-Ag-Cu (SAC) alloys, particularly those near the eutectic point, are emerging as the industry's preferred choice due to their superior thermal, mechanical, and wettability properties [50]. SAC solders are emerging as a promising alternative. These alloys also form high-quality joints with various substrates, including

advanced interconnects. However, challenges arise from the extensive formation of specific IMCs, which can weaken the joint.

Sn has long been a favored component in solder alloys due to its unique properties, making it ideal for solder joints. Its relatively low melting point of 232 °C facilitates easier soldering processes without subjecting components to damagingly high temperatures [51]. Furthermore, tin's excellent wetting properties ensure a robust bond between the solder and the joined metals [52]. Its ductility allows it to deform without breaking, a crucial trait for electronic devices that may undergo physical stress. Sn's resistance to oxidation also preserves the solder joint's integrity, reducing the need for excessive flux [53]. From an environmental and health perspective, tin's non-toxic nature offers a safer alternative to lead-based solders. While not the highest, its electrical conductivity is adequate for most electronic needs [54]. Sn's ability to alloy seamlessly with metals such as silver and copper allows for solder tailored for specific tasks. Its resilience against thermal fatigue and cost-effectiveness further cement Sn's position as a primary choice in the electronics industry, especially with the increasing demand for lead-free solder alternatives [55].

Ag is preferred in solder alloys primarily due to its exceptional thermal and electrical conductivity. Among all metals, silver stands out for its ability to efficiently distribute heat across solder joints. Ag is vital during soldering and when effective heat dissipation is paramount. Furthermore, its superior electrical conductivity ensures that solder joints offer minimal resistance, optimizing the performance of electronic devices [56]. With an Ag addition of under 0.5 wt.%, the strength of the solder initially drops but then rises with increasing Ag. Beyond 0.5 wt.%, the strength directly correlates with the amount added Ag. Sn-Ag-Cu solder with high Ag content excels in tensile strength and deformation resistance, whereas lower Ag

content is better for handling ductile and thermal fatigue deformations [57]. Its excellent wettability ensures the solder spreads seamlessly, forming a dependable bond with the components [58].

Additionally, including silver can adjust the solder alloy's melting point to fit specific application requirements. Its compatibility with various metals commonly used in industries further underscores its importance. Notably, solders containing silver have demonstrated remarkable reliability in harsh environments, including elevated temperatures or intense vibrations. This combination of attributes positions silver as an invaluable asset in solder alloys, especially for applications demanding high reliability and performance [59].

One of the most notable attributes of copper is its high electrical conductivity. This characteristic ensures that solder joints made with copper facilitate efficient electrical connections, which is crucial for electronic devices and circuits. In addition to its electrical conductivity, copper's impressive thermal conductivity stands out [60]. This property ensures heat is dissipated efficiently during soldering, leading to a more reliable joint formation. Another advantage of copper in solder joints is its high compatibility with a range of solder materials. This compatibility ensures that the bond between the solder and copper is robust and dependable. Lastly, the mechanical strength that copper imparts to the solder ensures that the joint remains durable, offering longevity to the connection and reducing the likelihood of joint failures. By incorporating Cu into the Sn–Ag eutectic, notable improvement was observed in the microstructure of the joint matrix and the solder-substrate interface, successfully minimizing Sn dendrite formation [61]. After being aged at 150 °C for 72 h, the shear strength of Sn–3.5Ag joints decreased by 21%, whereas the Sn-3.6Ag-1Cu joints experienced a 12% reduction. [61].

The SAC305 solder's eutectic temperature of 217 °C is notably higher than the 183 °C of Sn-37Pb [62]. As a result, Pb-free SAC solder is not a direct substitute for Sn-Pb in advanced electronics assembly, such as SMT. However, current reflow ovens can handle SAC305's reflow temperatures of 235-255 °C [63]. Traditional Sn-Pb solders were mainly used for low-stress applications due to their softness and susceptibility to wear and creep failure [64]. In contrast, (SAC) alloy solders offer better joint strength and creep resistance with their high tin content and robust intermetallic phases [65]. These SAC alloys have shown improved shear strength, even at higher temperatures of about 150 °C , and are more resilient to temperature changes, making them suitable for advanced electronics [66]. In several ways, the ternary SAC eutectic alloy solder is superior to the binary SA eutectic solder. Notably, it has a lower eutectic temperature of 217.2 °C compared to the 221.8 °C of the binary SA. This difference in temperature, along with its slower expansion of the intermetallic layer, increased strength, and reduced wetting angle, makes it highly advantageous. The melting points of these ternary SAC alloys, especially in the Sn-rich domain, are significant for lead-free soldering.

2.4 Comparison of Thin Film and Bulk Materials

Thin films are layers of material applied to substrates, offering unique properties not found in their bulk counterparts. While thickness is a crucial feature of thin films, it is not the defining factor. The properties of thin films can vary substantially from those of bulk materials mainly because of interfaces, stresses, thickness, microstructure, and underlying substrates, making them suitable for diverse applications, for instance, optical and tribological coatings, quantum structures, and nanoscale layers [67]. Thin films are two-dimensional materials created through a layer-by-layer accumulation process, where atoms, molecules, or ions are progressively added. The deposition process of thin films involves creating sputtering particles,

such as atoms or ions, transporting them to a substrate, and then condensing them onto the substrate. This process can result in films with different structures, such as amorphous or crystalline. Two primary methods for depositing thin films are chemical vapor deposition (CVD) and physical vapor deposition (PVD). CVD involves a chemical change on a substrate surface, while PVD uses mechanical or thermodynamic processes. These deposition techniques are fundamental in industries such as microelectronics and solar panels, emphasizing the importance of the specific thickness for each application [68].

Rupp and Gauckler examined ceric dioxide's microstructures, electrical conductivity, and Gadolinia-Doped Ceria spray pyrolyzed thin films. Their findings indicated that the electrical conductivity of these films is closely tied to their grain size. Specifically, as the grain size of CeO₂ films diminishes, there is an increase in conductivity and a decrease in activation energy. Similarly, CGO films with smaller grains exhibit enhanced conductivities and lowered activation energies [69].

Ding et al. conducted an in-depth study on the mechanical properties of boron-doped p⁺-Si films, contrasting them with low-doping bulk silicon. Through static tensile tests, they assessed the stress-strain curve, fracture stress, and Young's modulus, while the mechanical resonant test was employed to determine Young's modulus. The findings revealed that the corrected average values of Young's modulus in the (110) direction for the thin films were 122 ± 2.08 GPa and 125 ± 1.17 GPa from tensile and resonant tests, respectively. Notably, these values are 26% and 28% lower than the established values for low-doping bulk silicon. Additionally, the boron-doped p⁺-Si films exhibited a linear brittle behavior at room temperature, mirroring the characteristics of bulk silicon. This study underscores the inherent differences in mechanical

properties between thin films and bulk materials, emphasizing the importance of recognizing these variances when working with thin films [70].

CHAPTER 3

REVIEW OF FABRICATION AND CHARACTERIZATION TECHNIQUE

3.1 Magnetron Sputtering

In the early seventies, the planar magnetron sputtering source was introduced and soon became a prominent method for depositing metals and optical films. However, its application in semiconductor deposition, incredibly transparent conductive oxides (wide band gap semiconductor), came later due to the stringent quality requirements for semiconducting films. A key distinction of magnetron sputtering from other film preparation techniques is its higher energy input, allowing for tailored film properties [71].

Magnetron sputtering offers several benefits over other deposition methods, such as evaporation and chemical vapor deposition. These advantages include lower substrate temperatures, excellent film adhesion, rapid deposition rates, uniform and dense films, and cost-effectiveness. Magnetron sputtering is also scalable for larger areas and can sputter various materials, even those with differing vapor pressures [72].

Penning first introduced the concept of magnetron sputtering in 1936 [73]. Still, it was not until four decades later that the planar magnetron, a cornerstone of today's magnetron sputtering deposition, was developed. The primary characteristic of a magnetron discharge is the plasma's containment near the target, achieved through the interplay of electric and magnetic fields. The magnetic field is set to influence the electrons but not the ions, resulting in efficient ionization. This ionization allows magnetron discharges to operate at lower pressures ($<10^{-2}$ Pa) or higher current densities than non-magnetic glow discharges [73]. Sputtering is a technique that creates nanomaterials by striking solid surfaces with high-energy particles, for example, plasma

or gas. This method is especially effective for crafting thin nanomaterial films. During sputtering, gaseous ions hit a target surface, releasing small atom clusters based on the energy of the incoming ions. Various sputtering methods include magnetron, radio-frequency diode, and DC diode sputtering. Typically, sputtering occurs in a vacuumed chamber where a sputtering gas is added (Figure 3.2). When a high voltage is applied to the target, electrons collide with the gas, forming gas ions. Positively charged ions rush toward the target and, upon impact, dislodge atoms from the target's surface. A notable advantage of sputtering is that the resulting nanomaterial closely matches the target material in composition with minimal impurities, and it is more cost-effective than other methods, such as electron-beam lithography. The potential distribution between the target and substrate is crucial for sputtering and film deposition, determining the energies of ions and neutrals involved in the deposition. External parameters such as working pressure, discharge power, the distance between substrate and target, substrate temperature, magnetic field design, and excitation mode (DC or RF) impact this potential distribution.

A sputtering event begins with an initial collision between incoming ions and target surface atoms. Subsequent collisions among the target surface atoms follow this event. As these collisions continue, the movement of the target surface atoms becomes more uniform, eventually leading some atoms to break away from the surface. The elastic collision theory determines the maximum energy transfer during the first collision [74]. The maximum possible energy transferred in the first collision T_m is given by

$$T_m = \frac{4M_1M_2}{(M_1+M_2)^2} E \quad (3)$$

where M_1 and M_2 are the masses of the incident ions and target atoms, respectively, and E is the energy of incident ions. In the first order of approximation, the sputter yield S is

proportional to the T_m . The sputter yield of a given target material bombarded with different elements is given by

$$S = k \frac{1}{\lambda E \cos \theta} \frac{4M_1M_2}{(M_1+M_2)^2} E \quad (4)$$

where k is a constant, which includes different target constants, λ is the mean free path (MFP) for elastic collisions near the target surface, and θ is the angle between the normal on the target surface and the direction of incidence ions. The MFP is given by

$$\lambda = k \frac{1}{\pi R^2 n_0} \quad (5)$$

where n_0 is the number of lattice atoms per unit volume and R is the collision radius.

The potential distributions for DC and RF excitations differ due to their unique ionization mechanisms. The discharge voltage for RF excitation is considerably lower than for DC due to differing processes at the target and within the plasma. The DC discharge relies on ion-induced secondary electrons at the target, necessitating higher target voltages. In contrast, the RF plasma is primarily driven by oscillating electrons, leading to more effective ionization and lower target voltages. However, the electron confinement in RF discharges is not as effective as in DC, resulting in a higher plasma density in front of the substrate for RF excitation [75]. In RF magnetron sputtering, the discharge voltages result in notably reduced deposition rates compared to DC sputtering when the discharge power is kept constant. The rate of deposition is directly related to the discharge power. This unique characteristic of magnetron sputtering offers an advantage in regulating the sputter deposition process. In contrast, DC sputtering achieves deposition rates 1.5-2 times greater than RF sputtering. While the deposition rate for DC sputtering starts at zero power, RF sputtering necessitates a starting power of at least 10 W, a phenomenon attributed to its lower discharge voltages. The ion energy largely influences the

deposition rate at the sputtering target, and the energy of reflected argon atoms is more pronounced in DC sputtering than in RF sputtering.

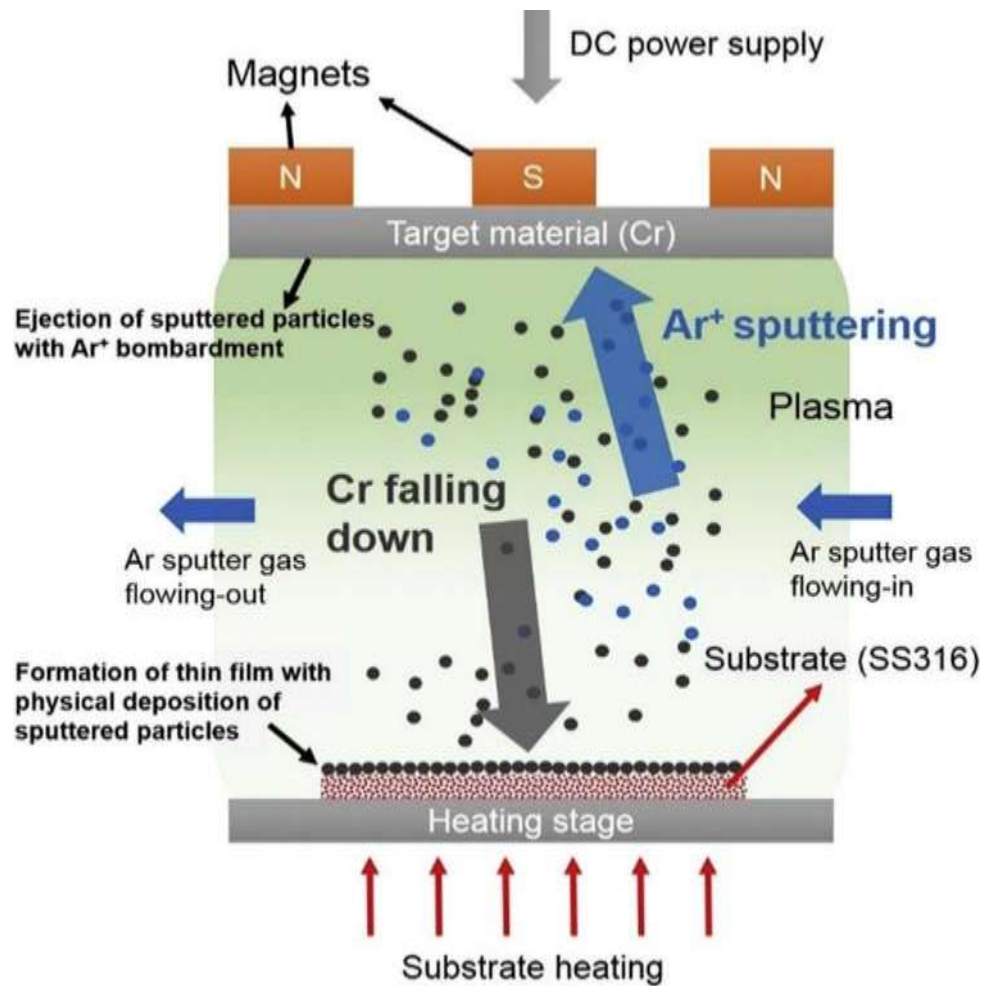


Figure 3.2 Schematic Diagram of Magnetron Sputtering System. Reproduced with Permission [76]

Zhang-Ming et al. (2000) observed that the positive ions are driven towards the cathode, leading to the sputtering of the target. Conversely, electrons and negative ions transition from the target to the substrate, significantly impacting layer growth. The plasma's extension towards the substrate is more pronounced in RF discharges. This phenomenon resulted in a more concentrated plasma adjacent to the substrate during RF excitation. The ion currents on a floating substrate remained largely stable under a pressure of 1 Pa, implying a negligible presence of charge exchange collisions. Furthermore, RF excitation showcased a current density of approximately 2.5 times that of DC, pointing to a denser plasma. The potential distribution acted as a barrier, ensuring that only electrons with sufficient energy could access the substrate, thereby maintaining a low electron current [77].

Traditionally, oxide coatings were made by reactive magnetron sputtering a metal target in an oxygen-rich environment or by RF sputtering of an oxide target. The challenges associated with both methods have been extensively documented [78]. RF sputtering yields high-quality films at slow rates and is complex for commercial scaling. Reactive magnetron sputtering creates target poisoning, where insulating layers form on the target, leading to arcs that can damage the film and the power supply.

The pulsed magnetron sputtering (PMS) process, which pulses the magnetron discharge in the medium frequency range, addresses many of these challenges. It reduces arc formation, resulting in fewer film defects, and achieves deposition rates comparable to pure metal films. Typically, PMS uses pulsed DC power, where the target is sputtered for a set pulse-on time, preventing charging that leads to arcing. The charge dissipates during the pulse-off period [79]. The alumina films made using PMS have a dense, defect-free structure, while those made using

traditional DC sputtering are porous and sub-stoichiometric. The physical properties of PMS-produced films are also superior, with significantly better light transmission [80].

3.2 Field Emission-Scanning Electron Microscope (FE-SEM)

The scanning electron Microscope (SEM) is a powerful tool for magnifying and analyzing various properties of a specimen at the microscopic level. Electromagnetic lenses replace the glass lenses found in optical microscopes to guide the path of electrons. These lenses are made of wire coils encased in metal, which generate a magnetic field when electric current flows through them. This magnetic field allows precise control over the electron trajectory. Two main types of electromagnetic lenses are employed: the condenser and the objective lens. The condenser lens is the first to interact with the electrons, narrowing the beam before it widens again. The objective lens then refocuses the beam onto the sample. The condenser lens primarily determines the beam size and, thus, the resolution, while the objective lens focuses the beam. Additionally, scanning coils are included in the lens system to move the beam across the sample in a grid-like pattern. These lenses often use apertures to fine-tune the beam size further (Figure 3.3) [81].

The SEM operates by focusing a high-energy electron beam onto a specimen. This interaction produces backscattered electrons (BSEs) and secondary electrons (SEs), which are then detected to create a magnified image. In electron microscopy, BSEs and SEs serve different purposes. BSEs are generated from deeper within the sample and are sensitive to variations in atomic number, making them helpful in understanding a sample's crystallography, topography, and magnetic field. In contrast, SEs come from the sample's surface and result from inelastic interactions with the electron beam, offering detailed information about the surface. The SEM has multiple operational modes that can be adjusted for specific needs. For instance, a smaller

beam diameter can be used for high-resolution imaging but may compromise visibility for low-contrast features. Conversely, a higher beam current can improve visibility but may reduce resolution. The SEM also allows for a balance between depth-of-field and beam current, offering a versatile imaging experience. The technology is supported by vendor-specific and open-source software, facilitating dynamic image processing and interpretation. SEM images can provide a wealth of information, including compositional microstructure, topography, and three-dimensional visualization. Other accessible properties include crystal structure, magnetic microstructure, and electron-stimulated optical emission [82].

The interaction between an electron beam and a specimen in an SEM produces two kinds of X-ray emissions: characteristic and continuum X-rays. These emissions help identify and quantify elements within the specimen. The EDS is used to measure this X-ray spectrum, and various software tools assist in the analysis. The process involves two main steps: qualitative and quantitative analysis. The former identifies elements based on their characteristic peaks but can be challenging due to peak interferences. The latter quantifies the elements by measuring the intensity of each peak, which is influenced by various factors such as electron scattering and X-ray absorption [82].

When an electron beam hits a crystal, it can channel into a shallow layer near the surface, depending on the orientation of the crystal planes. This channeling slightly reduces the electron backscattering coefficient, allowing SEM images to reveal subtle differences in the crystal's local orientation, such as grain boundaries and deformation bands. The backscattered electrons also undergo diffraction, creating a pattern known as electron backscatter diffraction (EBSD). This pattern offers valuable insights into the crystal's local orientation and symmetry. When combined

with elemental analysis, EBSD can help identify the crystal structure of an unknown specimen [83]

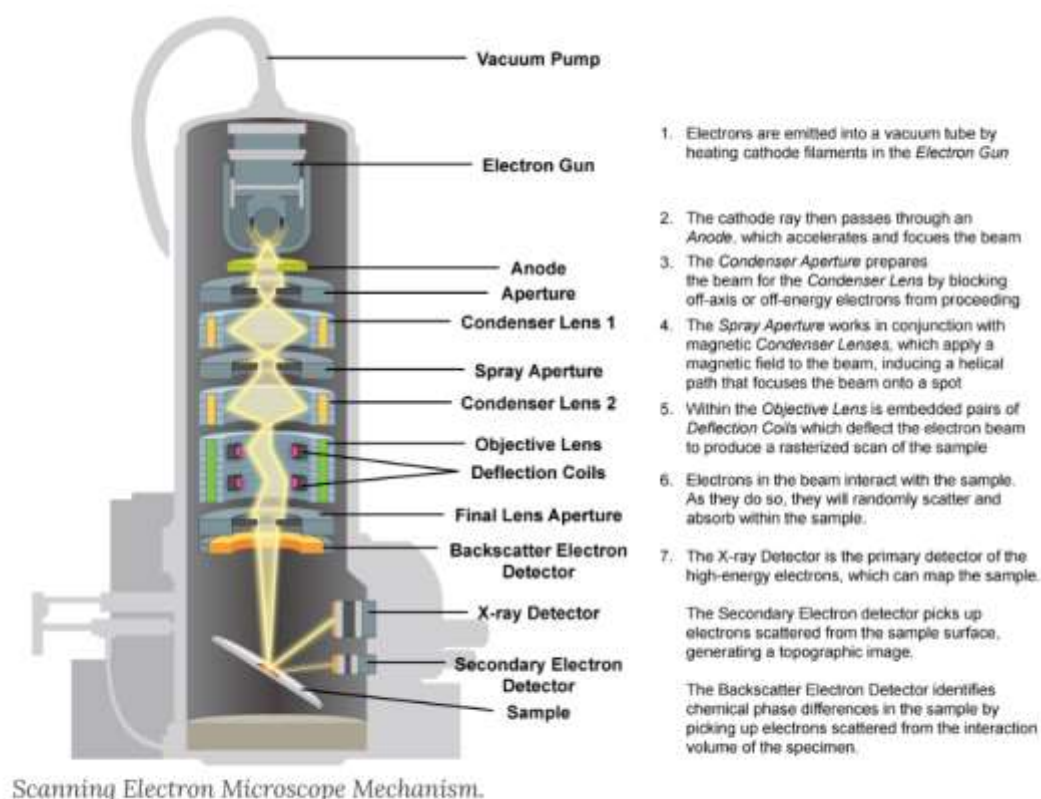


Figure 3.3 Schematic Diagram of Scanning Electron Microscopy. Reproduced with Permission [81]

3.3 X-ray Diffraction (XRD)

X-ray crystallography is a technique used to analyze the three-dimensional arrangement of atoms in a crystal. It was developed in the early 20th century, building on Wilhelm Rontgen's discovery of X-rays and Max von Laue's hypothesis about crystal lattices [84,85]. The method

relies on the diffraction of X-ray beams by the atoms in a crystal to produce a unique pattern, which can be mathematically analyzed to determine the crystal's structure.

The process involves several key components, including a source of X-rays and a detector (Figure 3.4) [86]. X-ray diffraction (XRD) is a technique that explores the arrangement of atoms in a crystal by using X-rays as electromagnetic waves. When X-rays hit the electrons in the atoms, they generate secondary waves, similar to how ocean waves create ripples when hitting a lighthouse, known as elastic scattering. In a crystal, the regular arrangement of atoms acts as a series of scatterers, producing a pattern of waves. While these waves usually cancel each other out due to destructive interference, they align constructively in specific directions, as described by Bragg's law.

$$n\lambda = 2d \sin \theta \quad (6)$$

Bragg's law mathematically defines these directions, factoring in the angle of incidence (θ), The spacing between the crystal planes (d), and the wavelength of the X-rays (λ). The result is a diffraction pattern with specific spots, known as reflections, that reveal the atomic structure of the crystal. X-rays are particularly useful for this method because their wavelengths are comparable to the distances between the atomic planes in the crystal. Although any wave could, in theory, produce diffraction when interacting with a regular array of scatterers, the sizes need to be similar for significant diffraction to occur [86].

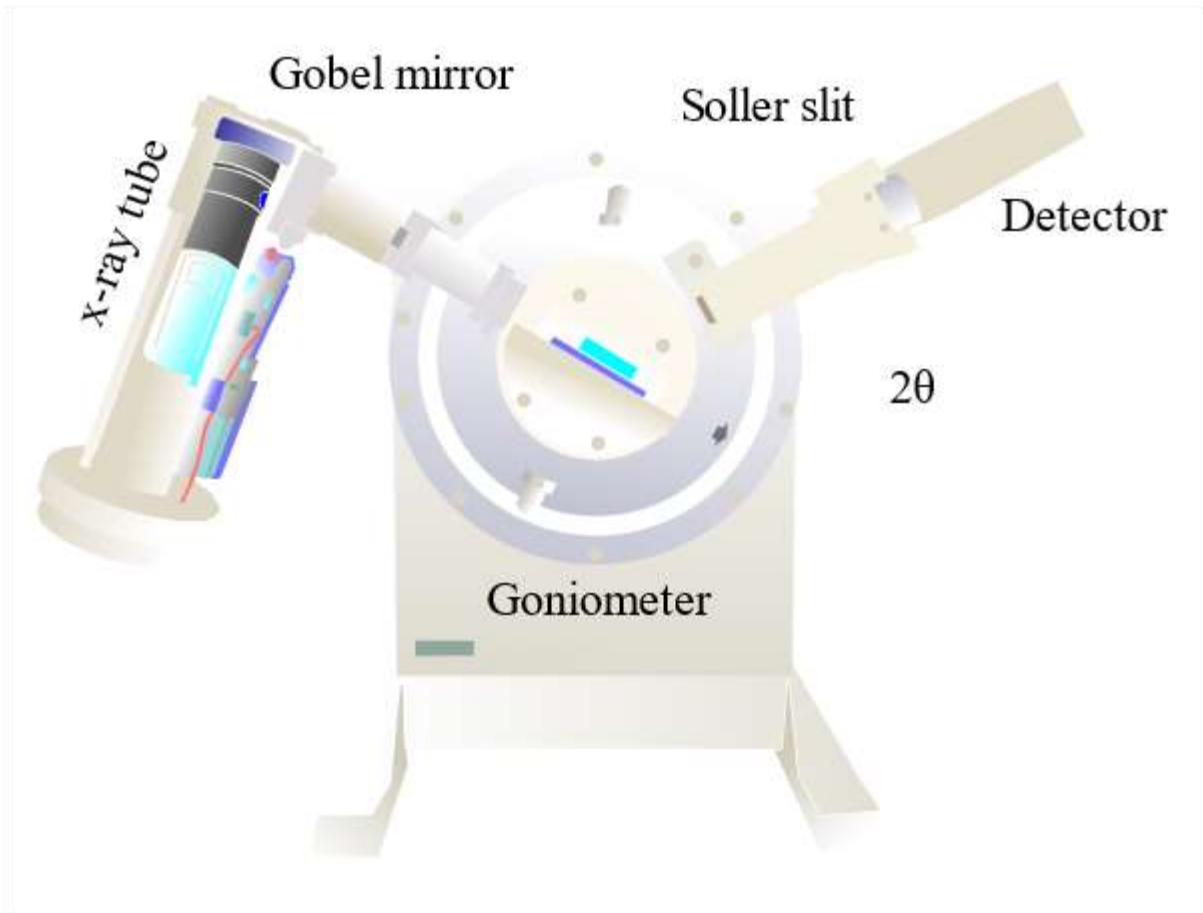


Figure 3.4 Schematic Diagram of X-ray Diffraction. Reproduced with Permission [87]

3.4 Atomic Force Microscope (AFM)

Atomic-force microscopy (AFM) is a powerful and versatile imaging technique for characterizing and manipulating a wide range of surfaces at the atomic and nanoscale levels.

AFM has captured intricate details of biological molecules such as DNA and proteins in various environments and achieved ultra-precise visuals of semiconductors and insulators while paving the way for nanoscale surface modifications [88]. This microscopy technique uses a fine tip connected to a cantilever to scan surfaces and measure forces, such as adhesion, magnetism, and mechanical properties (Figure 3.5) [89]. The tip's movements are tracked using a laser and photodiode [90].

Dynamic AFM employs two fundamental modes, amplitude modulation (AM-AFM) and frequency modulation (FM-AFM), to map surface features. AM-AFM, often used in air or liquid settings, relies on amplitude changes in a vibrating tip to gauge surface topography and material properties. FM-AFM, typically used in ultra-high vacuum conditions, uses frequency shifts for imaging and is more complex electronically. Both modes can operate in non-contact and tapping modes, but they have evolved as distinct methods with their scientific communities. The contact mode keeps the tip in constant touch with the surface, while the tapping mode allows intermittent contact, reducing shear forces. Tapping is generally preferred for imaging, and contact is used for specific force measurements. The technique can detect individual atoms by sensing subtle changes in the tip's vibration frequency due to chemical interactions. The choice of oscillation state in AM-AFM can significantly impact image quality, resolution, and sample deformation. Unlike electron microscopes, AFM offers a 3D surface profile without special sample preparation. It also operates in ambient conditions, making it more user-friendly and potentially offering higher resolution. However, AFM has limitations in the size and depth of the field it can image compared to SEM. Dynamic AFM methods offer a versatile surface analysis toolkit, each with advantages, complexities, and ideal environments [91].

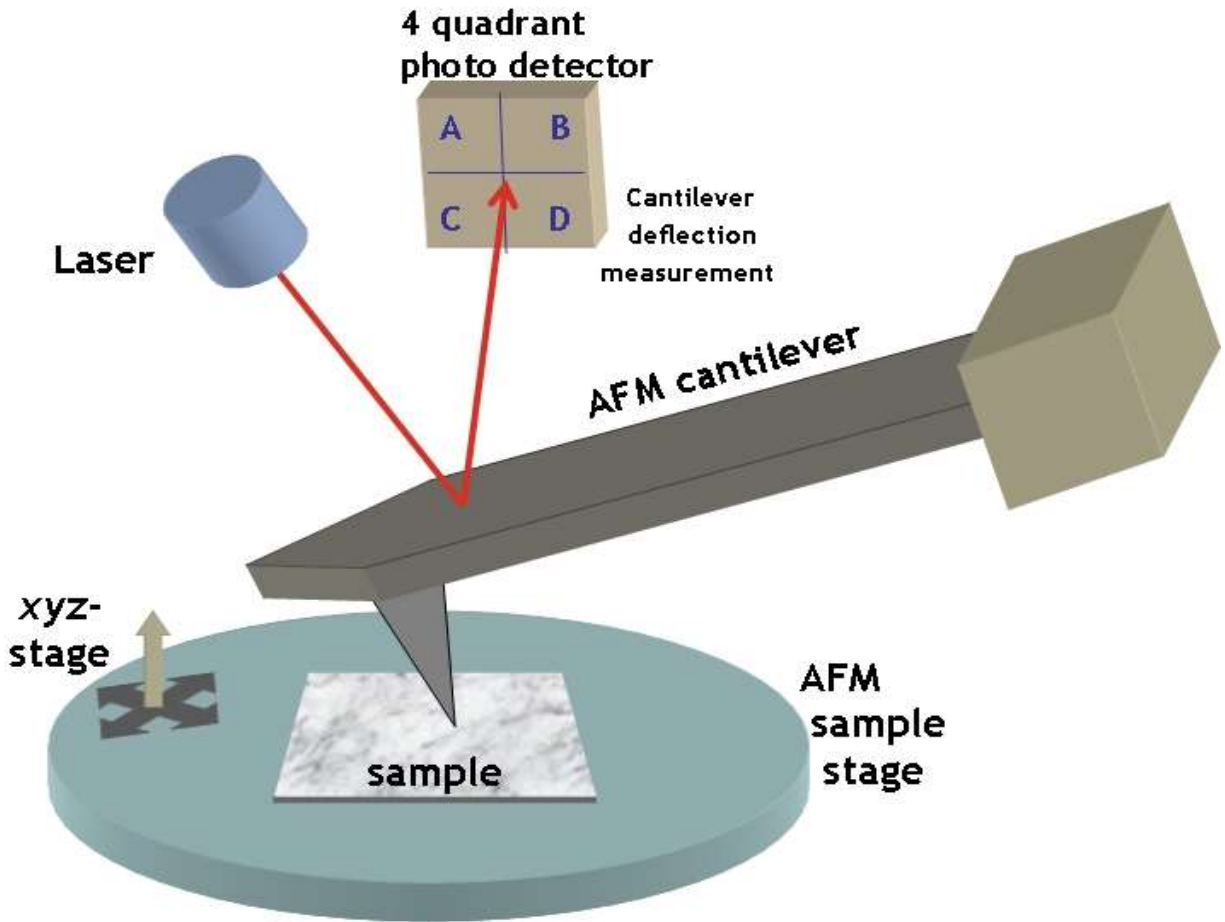


Figure 3.5 Schematic Diagram of Atomic Force Microscope. Reproduced with Permission [89]

3.5 Nanoindentation

Nanoindentation is widely used for assessing material properties such as hardness and elasticity, but its applications extend beyond these traditional metrics to include hardening rates, creep behavior, and residual stress. The technique is increasingly employed for deeper material science investigations, thanks to advancements in real-time imaging, acoustic monitoring, and high-temperature testing. These innovations enable researchers to explore nanoscale events such

as defect formation, mechanical inconsistencies, and phase changes, broadening nanoindentation's scope and potential in experimental research [92-94].

In a nanoindentation test, the key elements include the studied sample, the instruments that both exert and record force and movement, and the indenter tip. This tip is usually crafted from a diamond and is often shaped as a three-sided pyramid, known as a Berkovich pyramid, for standardization purposes. This pyramid shape is imperfect, and minor flaws can significantly impact the test results. Therefore, considerable research goes into precisely characterizing these tips to ensure accurate measurements, especially since the tip's point is never perfectly sharp but instead has a degree of bluntness [95].

The nanoindentation technique has been instrumental in overcoming the limitations of traditional hardness tests, which required measuring the contact area of the indenter's impression, a challenging task at shallow depths. Nanoindentation allows for continuous measurement of hardness and modulus throughout the indentation cycle, owing to methods such as the Oliver-Pharr method, which uses the stiffness measured during the unloading phase of the curve to determine these properties. The Oliver Pharr method fundamentally relies on calculating the contact depth by subtracting the force-to-stiffness ratio from the measured displacement, as outlined in Equation 6 [96].

$$h_c = h - \varepsilon \frac{P}{S} \quad (7)$$

The contact depth is represented by h_c , while h represents the observed displacement. The constant ε is associated with the indenter geometry, P signifies the measured force, and s denotes the stiffness. This method can calculate the contact depth and, consequently, the contact area without requiring microscopic examination of the remaining indentation. This makes it easier to conduct measurements on a tiny scale. The contact area is analytically determined as a

function of the contact depth and is influenced by the geometry of the indenter. At this point in the analysis, hardness can be computed by dividing the load by the contact area at any given depth and load. Similarly, this method calculates the reduced modulus, as outlined in the equation below [96, 97].

$$E_r = \frac{\sqrt{\pi}S}{2\beta\sqrt{A}} \quad (8)$$

While β is the geometrical constant in the order of unity and A is the projected area of the indentation at the contact depth h_c . Young's modulus is related to the reduced modulus, the indenter's modulus, and the Poisson ratios of both the indenter and the sample, as outlined in the equation below [96, 97].

$$E = \left[\frac{1-\nu^2}{E_r} - \frac{1-\nu_i^2}{E_i} \right] \quad (9)$$

The Oliver-Pharr method has proven to be a versatile tool for assessing the hardness and modulus of various materials, from brittle to elastoplastic. This method employs a load control protocol similar to traditional microhardness tests, allowing for precise calculations at specific loads and depths. Additionally, the continuous stiffness measurement (CSM), an extension of the Oliver-Pharr method, has been developed to evaluate hardness and modulus as depth functions. The CSM introduces a minor harmonic oscillation in the indenter shaft, typically resulting in a displacement of less than two nanometers and captures the dynamic response during each unloading cycle. CSM can be viewed as a sequence of load-unload displacement curves, distinct in its usage for calculating hardness and modulus at each cycle.

Hardness is not a unique, fundamental material property as it indicates their deformation resistance. In metals, for instance, hardness is linked to flow stress and work-hardening behavior [98]. Therefore, caution should be exercised when correlating hardness with yield stress, given the different stress and strain conditions in uniaxial tension and indentation tests. Despite the

simplicity of hardness tests, a mathematical model describing the deformation field around the indentation is essential for understanding its relationship to flow stress [99].

Historically, significant research efforts in the first half of the 20th century focused on developing models that relate indentation hardness to flow stress for non-strain and strain-hardening metals, using various indenter shapes. One foundational concept is Meyer hardness, defined as the load divided by the contact area, measured in Newtons [100]. Meyer's law, derived from this definition, establishes a power-law relationship between load and depth, suggesting that hardness remains constant for a geometrically self-similar indenter, irrespective of the load. Subsequent research led to the Tabor relation, which posits that hardness is generally 3 times the yield stress, a finding that holds across different indenter types and material conditions. In a standard nanoindentation experiment, the applied force and the movement of the indenter tip into the material's surface are carefully monitored and logged according to a predetermined pattern of applying and releasing pressure.

The critical metric often analyzed is the graph plotting load against displacement, commonly called the $P-h$ curve (Figure 3.4) [92]. This curve's overall form can vary depending on the tested material, usually indicating distinct mechanical characteristics. The subtle fluctuations in the $P-h$ curve are particularly intriguing, which could hint at specific physical activities occurring under the surface where the indenter tip makes contact.

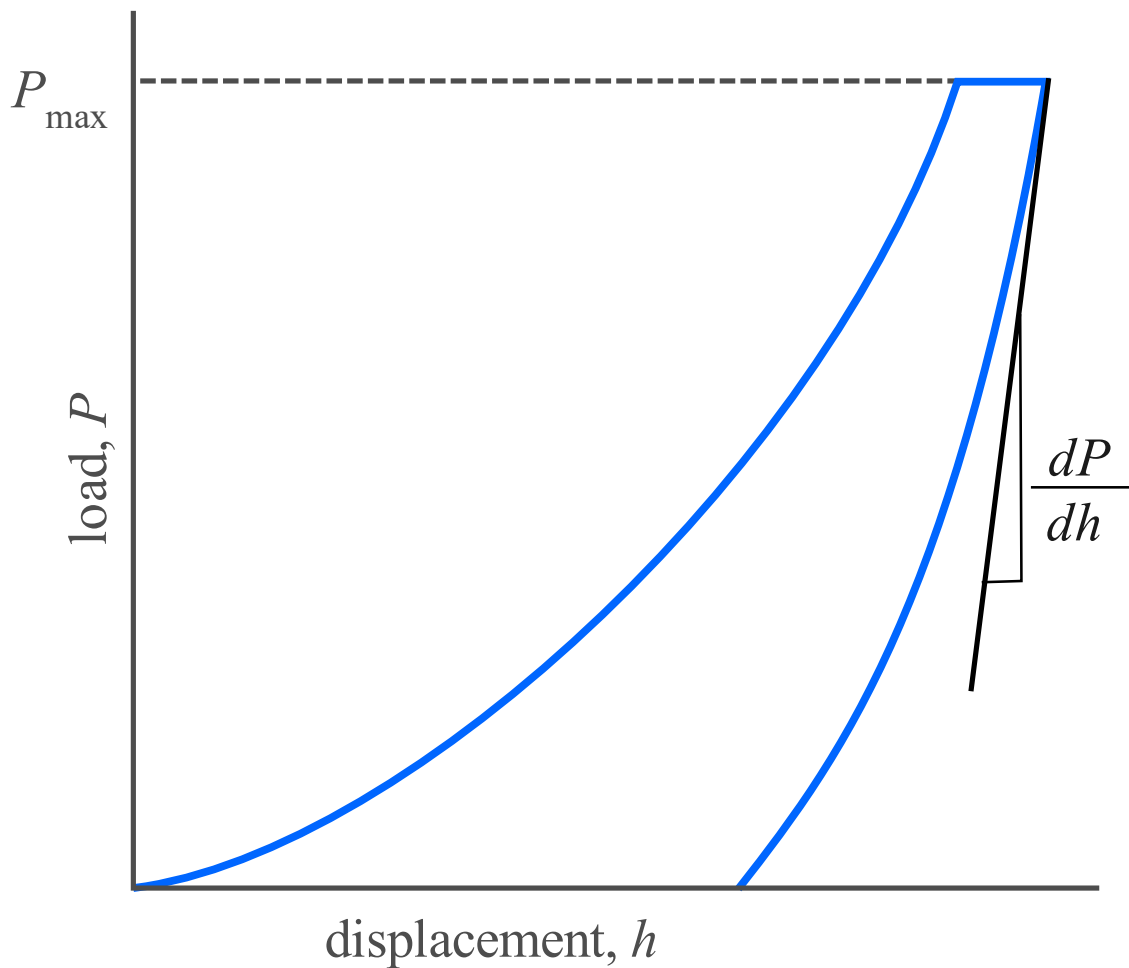


Figure 3.6 Schematic of a Load-Displacement Curve for Nanoindentation.

Reproduced with Permission [101]

3.6 Four-Point Probe (FPP)

The four-point probe is a widely-used instrument for assessing the electrical resistivity of various materials used in electronics. This method quickly and accurately evaluates sheet carrier density and mobility with minimal sample preparation. This device employs four probes: two for sending an electrical current through the material and two for measuring the resulting voltage [102]. These data are crucial for understanding material properties such as resistivity, which

varies based on area and thickness. Additionally, the FPP can reveal other material characteristics, for example, doping (positive or negative) in semiconductors and the material's electron mobility.

Various measurement methods have been developed for the traditional FPP, including but not limited to several modes: van der Pauw, collinear, square, dual probe configuration, and other enhanced modes. The collinear mode is the most frequently used [103]. The four probes are aligned straight and spaced equidistantly on the material's surface. As depicted in Figure 1, collinear mode involves sending a current through the outer pair of probes while measuring the voltage drop across the inner pair using an ultra-high impedance voltmeter. The collinear configuration leads to a voltage drop. V mainly occurs on the surface of the semiconductor due to the current, I , passing through the material. The resistance, R , is subsequently calculated using the formula $R=V/I$.

The starting premise is that the probe's tip is exceptionally tiny, to the point of being infinitesimal. At the same time, the bulk sample itself is extensive, approaching semi-infinite in size. For this bulk sample, it is essential that its thickness, t , exceeds the spacing between the probes, s . In the FPP method, the resistivity of bulk material is determined using the formula:

$$\rho = 2\pi S \frac{V}{I} \quad (10)$$

Where ρ represents resistivity, S is the constant probe spacing measured in millimeters, I is the current supplied in microamperes, and V is the measured voltage in millivolts. Electrical conductivity (σ) is given by the equation below.

$$\sigma = \frac{1}{\rho} \quad (11)$$

When measuring semiconductor crystals or thin films, the current flows through three distinct pathways: the surface state, the surface space-charge layer, and the bulk state. This

complexity makes it challenging to accurately assess the material's electrical properties due to the intertwined contributions from these channels. However, suppose the distance between the probes is smaller than the thickness of the space-charge layer. In that case, the measured current originates from the surface area, thereby reducing the impact of the bulk state. Research indicates that narrowing the gap between the probes can help mitigate the effects of leakage current and surface flaws, enhancing the sensitivity to surface properties. The resistance (R) of the thin film is calculated as

$$R = \frac{V}{2I} \quad (12)$$

The formula for resistivity (ρ) in the context of thick sheets is:

$$\rho = \frac{\pi t V}{\ln 2 I} \quad (13)$$

where \ln denotes the natural logarithm. To determine electrical conductivity (σ), the equation is:

$$\sigma = \frac{1}{\rho} \quad (14)$$

CHAPTER 4

FABRICATION OF SMOOTH SAC305 THIN FILM VIA MAGNETRON SPUTTERING

4.1 Introduction

Electronic devices consist of various components, including resistors, transistors, capacitors, and others. These components are interconnected using solders at different levels to ensure mechanical and electrical connections. The interconnection technology has progressed from conventional automated wire and tape bonding to flip-chip technology owing to reliability, high electrical performance, and package miniaturization [18]. Sn-Pb solder alloys have been widely used in electronics due to their low melting temperature and good wetting properties, but they are being phased out due to regulations [1,16,19]. SAC305 (96.5%Sn-3%Ag-0.5%Cu) solder is evolving as a promising alternative for Sn-Pb solders owing to its low melting temperature, better compatibility with other components, and excellent mechanical/structural properties.

The deposited solder's smooth and continuous surface topography is essential for optimal soldering suitability in microelectronics. The microstructure and properties of solder joints play a crucial role in determining their performance. Specifically, thin film solders free of imperfections and with a smooth surface exhibit superior electrical and thermal conductivity, strong adhesion, and exceptional reliability [5-9]. The microstructural characteristics of these micro and nanoscale solders are not fully understood. Still, knowledge in this area could lead to optimization of the joining process and improve the electrical properties and reliability of the joints through the establishment of correlations between fabrication, microstructure, and properties.

The properties of thin films depend on numerous factors, such as substrate type, substrate cleaning, pressure, gas type, gas flow, temperature, current density, and bias voltage [106]. However, altering these parameters can impact film deposition rate, adhesion, grain size, and thickness, affecting the morphology, microstructure, coating's hardness, Young's modulus, and electrical resistivity [107]. Chan and Teo (2005) showed that controlling sputtering power and deposition pressure in DC magnetron sputtering of copper films on p-type Si led to optimized growth, improved deposition rates, electrical properties, and structural quality [108]. Similarly, Shah et al. (2010) found that working pressure, temperature, and power significantly affected the microstructural characteristics of Chromium Nitride (CrN) films deposited on Si(100) substrates using reactive magnetron sputtering. The preferred orientation, grain size, crystallinity, and texture coefficient of CrN films depended on the sputtering conditions [109]. Optimizing these parameters is essential for enhancing the performance of thin solder joints in microelectronics applications.

Magnetron sputtering is one of the standard methods for depositing solder alloys onto the chip bond pads in flip-chip technology. In magnetron sputtering, materials are transformed atom by atom in a vacuum chamber from a target to the growth surface of a film being deposited onto a substrate. The film thus produced has various advantages over other PVD methods, such as excellent mechanical properties, good adhesion to the substrate, high deposition rate, good thickness uniformity, and scalability to large areas [6,7]. However, the fabrication of smooth, thin SAC305 films is usually challenging, and limited research has addressed this.

The annealing process for metals consists of three main stages: recovery, recrystallization, and grain growth. In the recovery stage, the metal's physical properties, such as thermal expansion and electrical conductivity, are restored as dislocations in the structure move

to stress-free environments. This process softens the metal and sets the stage for recrystallization. The metal is heated above its recrystallization temperature during recrystallization, allowing new stress-free grains to replace the deformed ones. The final stage, grain growth, occurs if annealing continues after recrystallization. This grain growth makes the metal's microstructure course, reducing its strength [110,111].

Abbas et al. explored the effects of annealing on silver thin films fabricated through physical vapor deposition. The films were annealed at 373.15 K to 1073.15 K in a vacuum oven for 20 min. The study found that lower annealing temperatures resulted in porous, interconnected nanoparticles, while higher temperatures led to distinct nanoparticles of various sizes and shapes [112]. Liu et al. studied the deposition of Co₄₀Fe₄₀B₁₀Dy₁₀ thin films on glass substrates using DC magnetron sputtering. The films, with 10 to 50 nm thicknesses, were heat-treated at temperatures between 100 °C and 300 °C. A notable outcome was that surface roughness (Ra) decreased as the annealing temperature increased, indicating smoother films at higher temperatures (113).

This study investigated a method to improve the surface morphology of SAC305 thin films by modulating the substrate and various parameters of magnetron sputtering to produce smooth and continuous SAC305 thin film. A comprehensive annealing treatment was carried out in a vacuum furnace to enhance the surface morphology of the films. The thin films were characterized using Field emission - Scanning Electron Microscopy images (FE-SEM) and EDS.

4.2 Experimental Setup

4.2.1 Wafer Cleaning

SAC305 thin films were fabricated on various wafers from a single target (99.99% purity) by magnetron sputtering. All the wafers were prepared by the industry-standard RCA

cleaning procedure [114]. This process involves two cleaning steps: standard cleaning-1 (SC-1) and standard cleaning-2 (SC-2). During SC-1, the Si wafer was immersed in a solution of water (H_2O), ammonium hydroxide (NH_4OH), and hydrogen peroxide (H_2O_2) in a ratio of 5:1:1 for 10 min at $80\text{ }^\circ\text{C}$. This step removes organic contaminants, oxides, and quartz surfaces from the wafer surface. Afterward, the wafer was rinsed in deionized (DI) water at room temperature. SC-2 involved immersing the wafer in a solution of H_2O , hydrochloric acid (HCl), and H_2O_2 in a ratio of 5:1:1 for 10 min at $80\text{ }^\circ\text{C}$. This step aimed to remove alkali residues and traces of metals, such as Au and Ag, from the silicon surface. The wafer was then again rinsed in DI water at room temperature. The wafer was subjected to ultrasonic cleaning in an acetone solution for 3 min to remove any remaining particles, organic components, and residual metals. A high-pressure nitrogen blower was employed to dry the substrate.

4.2.2 Magnetron Sputtering

The deposition system employed is the ATC Orion-8 Sputter Coater from AJA International, as illustrated in Figure 2.4. This chamber features 8 2-in magnetron sputter guns with mechanically controlled shutters operated by pressurized air. A high-performance turbomolecular pump can reduce the chamber's internal pressure to approximately 10^{-8} Torr. A gate valve connected to the turbomolecular pump regulates this pressure during deposition. The substrate holder is positioned at the top of the chamber, maintaining a distance of roughly 150 mm from the sputter targets. The substrate holder is designed for precise control and versatility. It offers a rotational speed range of 0-40 RPM, ensuring accurate substrate rotation and even coating. Additionally, the holder features a heating function that can reach up to $850\text{ }^\circ\text{C}$, operable in both local and remote modes. A slow temperature ramp-up is required to prevent warping of the transferable substrate carrier, with a recommended ramp time to a maximum temperature of

90 min. Argon gas is the sputtering medium, with its flow rate managed by a mass flow controller. The chamber is outfitted with three 750 W DC and two 300 W RF sputter guns for versatile sputtering options.

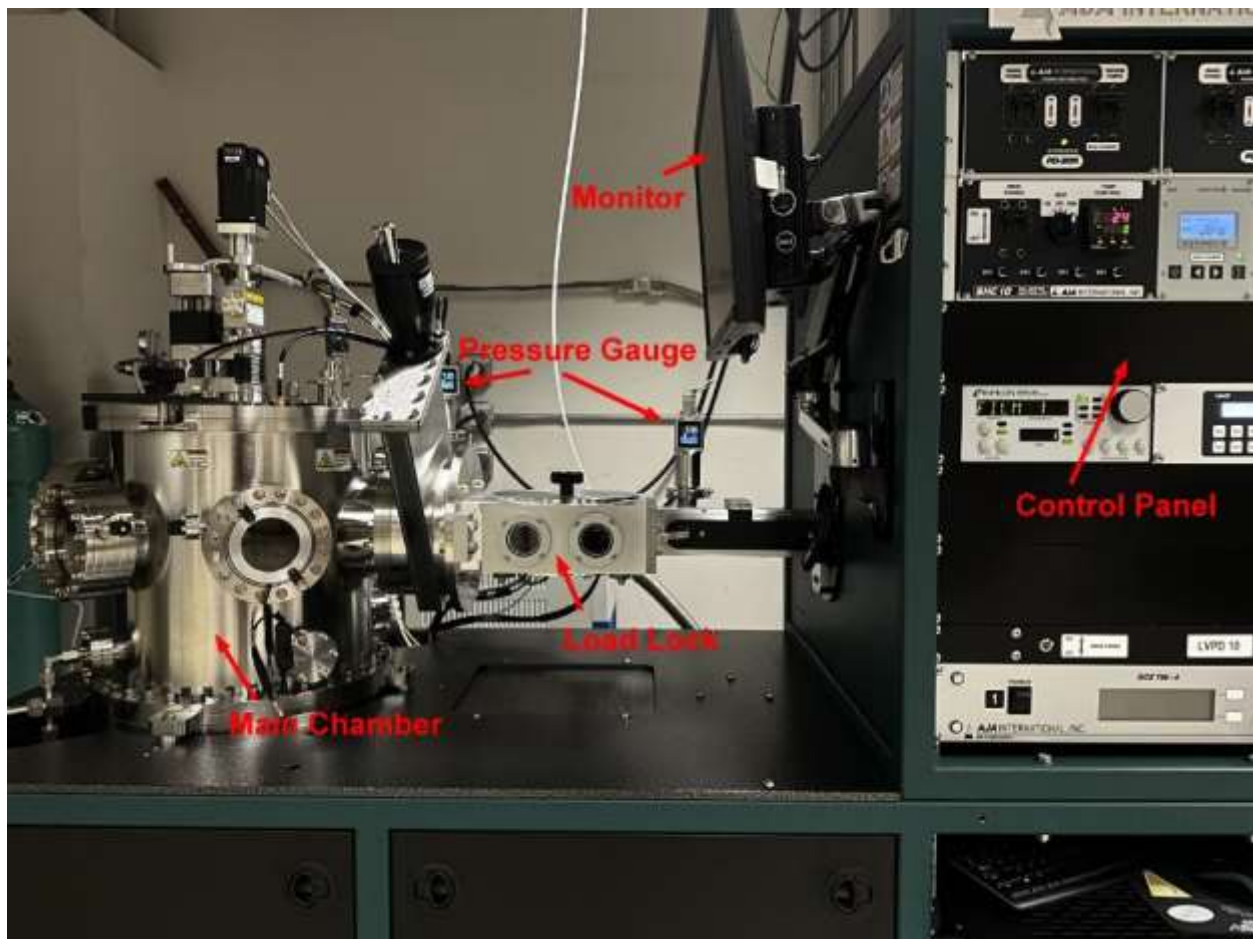


Figure 4.1 Image of ATC Orion-8 Sputtering Deposition System

After loading the clean Si wafers to the substrate holder of magnetron sputtering (Figure 4.1), the chamber was pumped down to a high vacuum pressure of $4 \times 10^{-7} - 8 \times 10^{-7}$ Torr. The

Ar flow was kept constant at 20.5 SCCM during deposition. Uniform thickness was achieved ($\pm 5\%$ error) with a 20 rpm substrate holder rotation, fixed at 16 cm from the target. The base pressure in the chamber before sputtering was 3×10^{-2} Torr. SAC305 thin films were fabricated using DC magnetron sputtering at 200 W power and 4 mTorr pressure. The deposition was conducted at room temperature (24 °C), 50 °C, and 100 °C.

The SAC305 thin film was fabricated using RF and DC magnetron sputtering at varying pressures and power levels on a Si substrate, all at room temperature. The details of the experiment are summarized in Table 4.1. The thin films were characterized using FE-SEM.

It is important to highlight that the attainable minimum pressure within the chamber during deposition was 3 mTorr. At this pressure, the minimum power required to sustain the plasma was 20 watts. The maximum power permissible for deposition at this lowest pressure was 200 watts. Exceeding the 200-watt threshold poses a potential risk of target burning, attributed to the bombardment of argon ions carrying high kinetic energy.

Table 4.1 Deposition of SAC305 Thin Film at Various Pressures and Power

Sample#	DC power (watt)	RF power (watt)	Pressure (mTorr)	Time (min)	Deposition Rate ($\text{\AA}/\text{s}$)	Thickness (μm)
1	20	-	3	120	0.35	0.25
2	80	-	3	120	1.45	1.04
3	140	-	3	120	2.7	1.94
4	200	-	3	120	3.9	2.80
5	-	20	3	120	0.33	0.24
6	-	80	3	120	1.31	0.94
7	-	140	3	120	2.16	1.56
8	-	200	3	120	2.95	2.08
9	200	-	2.4	120	4	2.88
10	200	-	8	120	3.1	2.23
11	200	-	14	120	2.24	1.61
12	200	-	20	120	1.63	1.17
13	-	200	2.4	120	3.0	2.16
14	-	200	8	120	2.3	1.65
15	-	200	14	120	1.7	1.22
16	-	200	20	120	1.42	1.0

4.2.3 Annealing

An extensive annealing process was performed on a sample deposited at room temperature within a vacuum furnace to investigate the surface morphology of thin films. The annealing process involved varying temperatures ranging from 50 to 220 °C for 1 to 3 h. Controlled heating was ensured by gradually increasing the temperature at a ramp rate of 12 °C per min. Once the annealing process was complete, the heater was turned off, and the vacuum was maintained until the sample's temperature dropped below 50 °C. The details of the experiment are summarized in Table 4.2

Table 4.2 Annealing Process of SAC 305 Thin Film at Various Temperatures.

Sample #	Temperature (°C)	Time (hr.)
1-2	120	1,3
3-4	150	1,3
5-6	180	1,3
7-8	200	1,3
9-10	210	1,3
11	220	1

4.2.4 FE-SEM

In the characterization of the surface morphology of SAC305 thin films, a Hitachi S-4700 FE-SEM was used (Figure 4.2). This high-resolution, cold FE-SEM offers a wide magnification

range, spanning from 30x to an impressive 500,000x. The instrument can achieve a spatial resolution as fine as 1.5 nm at an operating voltage of 15 kV and a working distance of 12 mm. Additionally, it can attain a resolution of 2.5 nm at 1 kV with a 2.5 mm working distance. Digital imaging is highly versatile, allowing for data capture in various file formats, including BMP, TIFF, and JPEG. Beyond morphological analysis, the Hitachi S-4700 is equipped with EDAX EDS capabilities, enabling elemental composition analysis of the samples under investigation.

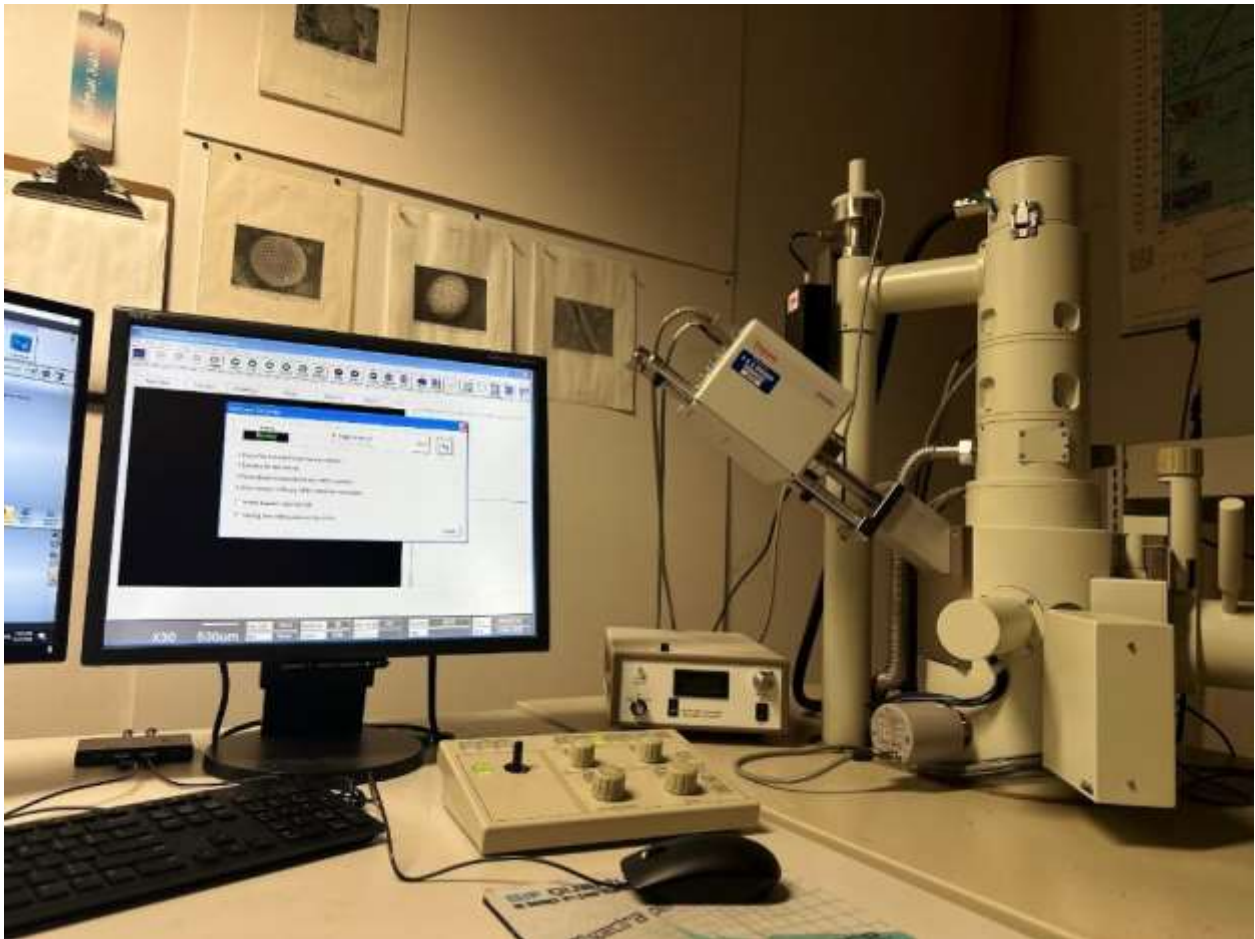


Figure 4.2 Hitachi S-4700 Field Emission Scanning Electron Microscope (FE-SEM)

4.3 Results and Discussion

4.3.1 Substrate Temperature

The process parameters were set at 200 W power and 4 mTorr pressure, and the deposition was carried out at room temperature. The resulting film exhibited a grain size of 1.65 μm (Figure 4.3a). This grain size was determined using FE-SEM images, and the measurements were analyzed using the ImageJ software. However, the film's high roughness posed challenges due to AFM tip resolution limitations, preventing accurate AFM measurements. The film's structure was notably porous, marked by distinct grain boundaries, which made nanoindentation tests infeasible. The substrate temperature was varied to enhance the film's surface morphology; the temperature was increased to 50 °C, 75 °C, and 100 °C while keeping other sputtering parameters constant. At 50 °C, the film's morphology remained unchanged. At 75 °C, more porous grains emerged due to coalescence. At 100 °C, the film exhibited disconnected spherical grains with significant grain boundaries, indicating complete melting (Figure 4.3b).

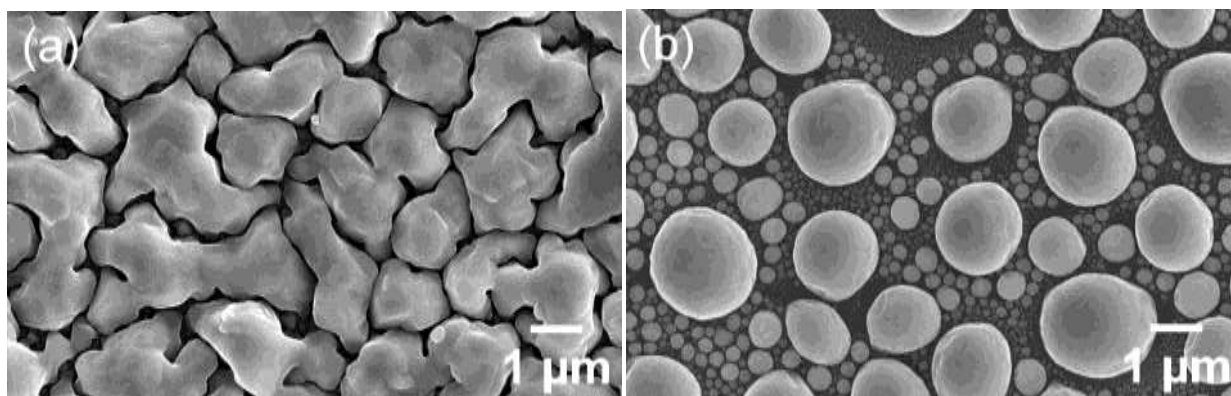


Figure 4.3 SAC 305 Deposited at (a) Room Temperature and (b) 100 °C.

4.3.2 *Annealing*

During the annealing process, it became evident that films exposed to lower temperatures for shorter durations remained unaffected. Specifically, when annealed between 120 °C and 210 °C for 1 to 3 h, the film's surface morphology showed no significant changes. Illustrations of the films annealed between 180 °C and 210 °C are presented in Figure 4.4 (a-f). However, when the annealing conditions were increased to 220 °C for an hour, the films underwent noticeable transformations (Figure 4.4g). This transformation included grain growth, the emergence of voids, and, in some instances, fragmentation into isolated islands on the substrate. Despite these changes, the annealed samples did not demonstrate a marked enhancement in film quality. These observations were consistent with the findings presented by Abbas et al. (2019) [119]. Given these results, the study's emphasis shifted to the non-annealed films, with a concentrated effort to explore the influence of varied sputtering parameters on enhancing the surface morphology of the thin films.

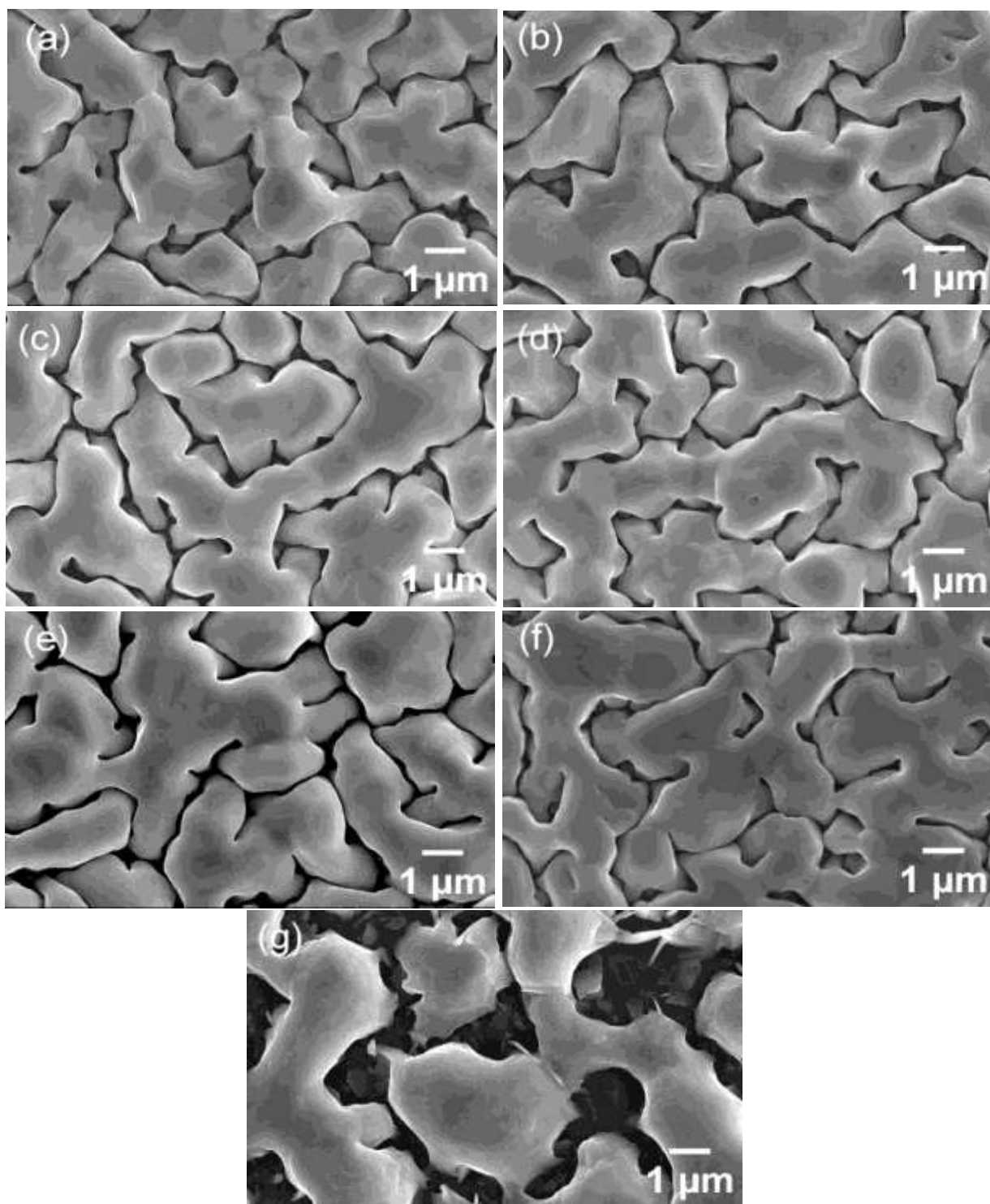


Figure 4.4 FE-SEM Images of the Thin SAC305 Films Annealed at (a) 180°C for 1 hr., (b) 180°C for 3 hr., (c) 200°C for 1 hr., (d) 200°C for 3 hr., (e) 210°C for 1 hr., (f) 210°C for 3 hr., (g) 220°C for 1 hr.

4.3.3 Sputtering Power

DC power is suitable for depositing conductive materials. Insulating material deposition leads to positive ion accumulation, increasing target potential and reducing the electric field, which halts the sputtering process. Conversely, RF power is versatile, allowing the deposition of conductive, semiconductive, and insulating materials. The RF power source alternates between positive and negative polarities. During the positive half-cycle, electrons flow to the target surface, neutralizing the accumulated positive charge and enabling positive ions to bombard the target in the negative half-cycle of the RF voltage. This process facilitates the sputtering of insulating targets. SAC305 is a conductive material well-suited for both DC and RF processes.

Figure 4.5 reveals that the deposition rate rises with increased sputtering power for both DC and RF sputtering processes. This relationship is influenced by the Ar ion flux and its average energy when it collides with the target. Elevated Ar ion flux at higher power typically leads to pronounced ion interactions with the target. Concurrently, the enhanced kinetic energy of these ions augments the chances of incident ions dislodging atoms from the target. Both factors, tied to the applied voltage and sputtering power, play pivotal roles in boosting the sputter deposition rate.

The excitation mode notably impacts the deposition rate; for instance, RF sputtering yields a lower deposition rate at equivalent discharge power than DC sputtering. At lower power levels, specifically at 20 W, the difference in deposition rates between DC and RF sputtering is negligible, amounting to a mere 0.03 Å/s. However, this difference becomes more substantial as the power increases, reaching a difference of 1.05 Å/s at 200 W. This phenomenon can be interpreted as the lower discharge voltage RF magnetrons exhibit a significantly higher ion flux relative to neutral particles than DC magnetrons. When operating at the same substrate bias

voltage and deposition rate, the energy delivered to the growing film during RF excitation is also considerably more significant than that during DC excitation. However, for the same discharge power, the deposition rate of thin films using a DC magnetron surpasses that of an RF magnetron. This difference in outcome can be attributed to the accelerating bias voltage at the cathode in a DC magnetron, which is notably higher than in an RF magnetron.

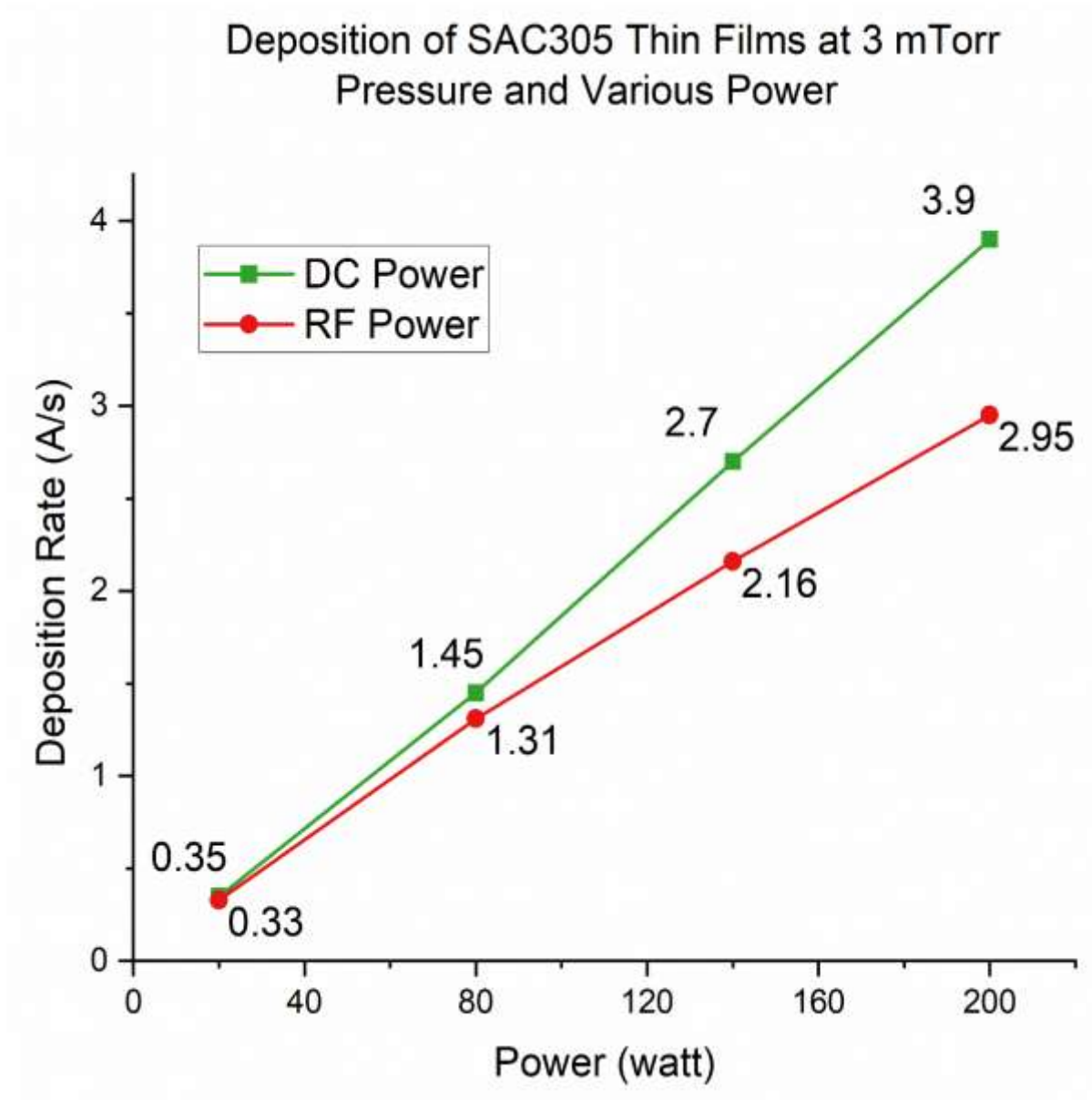


Figure 4.5 Investigating Variable Power Effects in Magnetron Sputtering Deposited SAC305 Thin Films at 3 mTorr Pressure and Various Power.

Figure 4.6 shows the FE-SEM images of the thin SAC305 films surface area deposited at 200W through DC and RF power source on Si substrate at various pressure. At a deposition

power of 20 W, SAC305 films displayed a fine-grain structure interspersed with larger grain boundaries. This characteristic of smaller grains, featured by voided boundaries, was more pronounced under RF power than DC power. However, a shift was observed when the power was elevated to 80 watts: the grain structure for the DC power supply became denser, and the grains enlarged. Interestingly, further increases to 140 and 200 watts did not significantly alter the surface morphology. In contrast, the SAC305 thin film deposited using 80 watts of RF power, though improved compared to the 20 W deposition, remained porous and lacked continuity. As the RF power was ramped up to 140 watts and 200 watts, a noticeable improvement was shown in the sample surface morphology, accompanied by an increase in grain size.

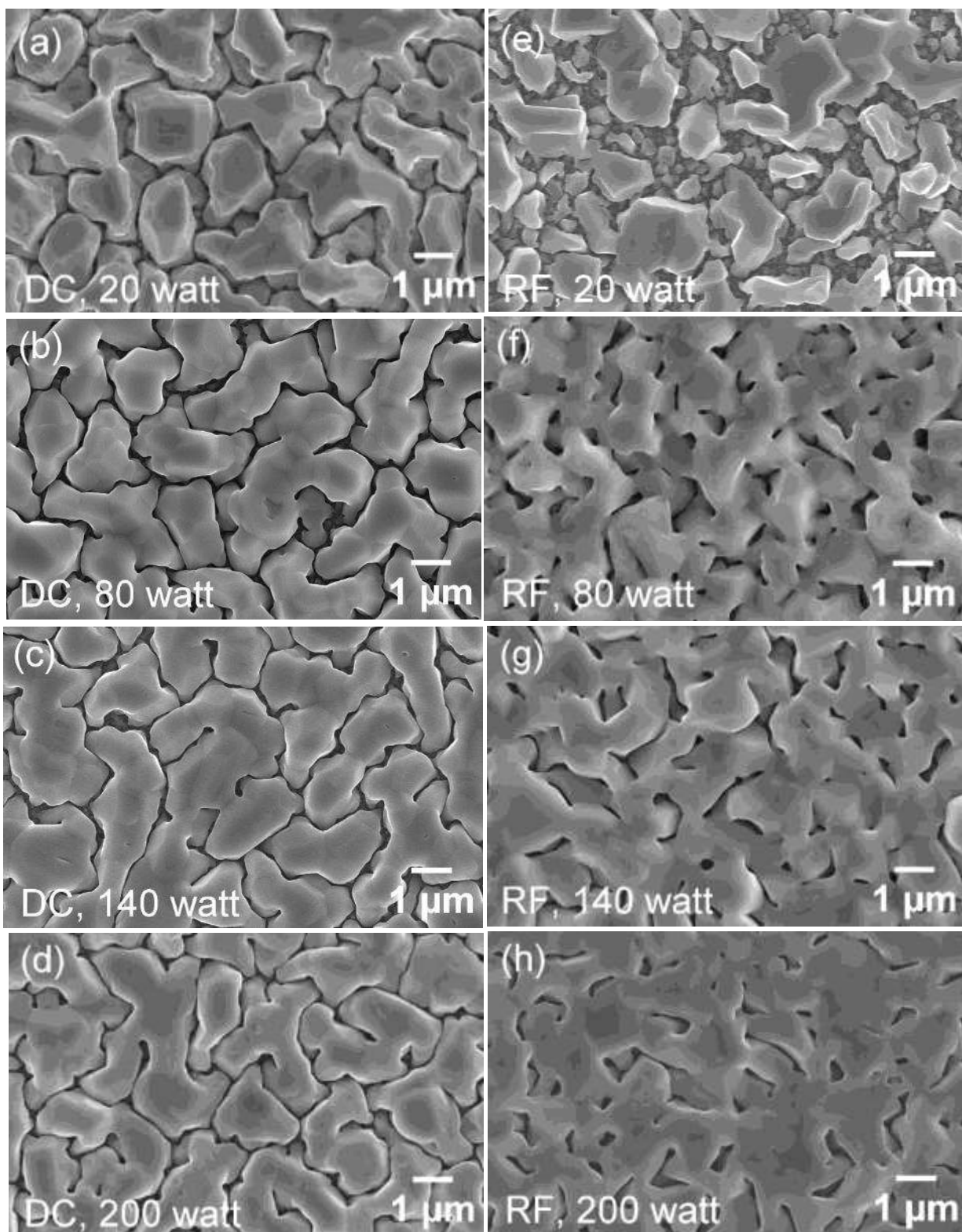


Figure 4.6 FE-SEM Images of the Thin SAC305 Films Surface Area Deposited at 200W through DC and RF Power Source on Si Substrate at Various Pressure.

4.3.4 *Sputtering Pressure*

The deposition rates of SAC305 films were investigated under varying deposition pressures ranging from 2.4 mTorr to 20 mTorr at a constant 200 W DC and RF power supply. At 2.4 mTorr and 200 W power, the deposition rate was 4 Å/s for DC power and 3.0 Å/s for RF power. However, the deposition rate declined as the pressure increased for both DC and RF power supplies. At 20 mTorr and 200 W power, the deposition rate was 1.63 Å/s for DC power and 1.42 Å/s for RF power. The observed decrease in deposition rate with increasing deposition pressure can be attributed to collisional events between the sputtered SAC305 atoms and Ar species in the deposition chamber. As the sputtering pressure increases, the collision probability between sputtered particles and gas particles typically increases, due to the shorter MFP. As a result, some sputtered SAC305 atoms are deflected away from the substrate, leading to a reduced deposition rate. Figure 4.7 illustrates the relationship between the deposition rate of SAC305 films and working pressure for both RF and DC sputtering methods. In both techniques, an increase in working pressure from 2.4 mTorr to 20 mTorr results in a decline in the deposition rate.

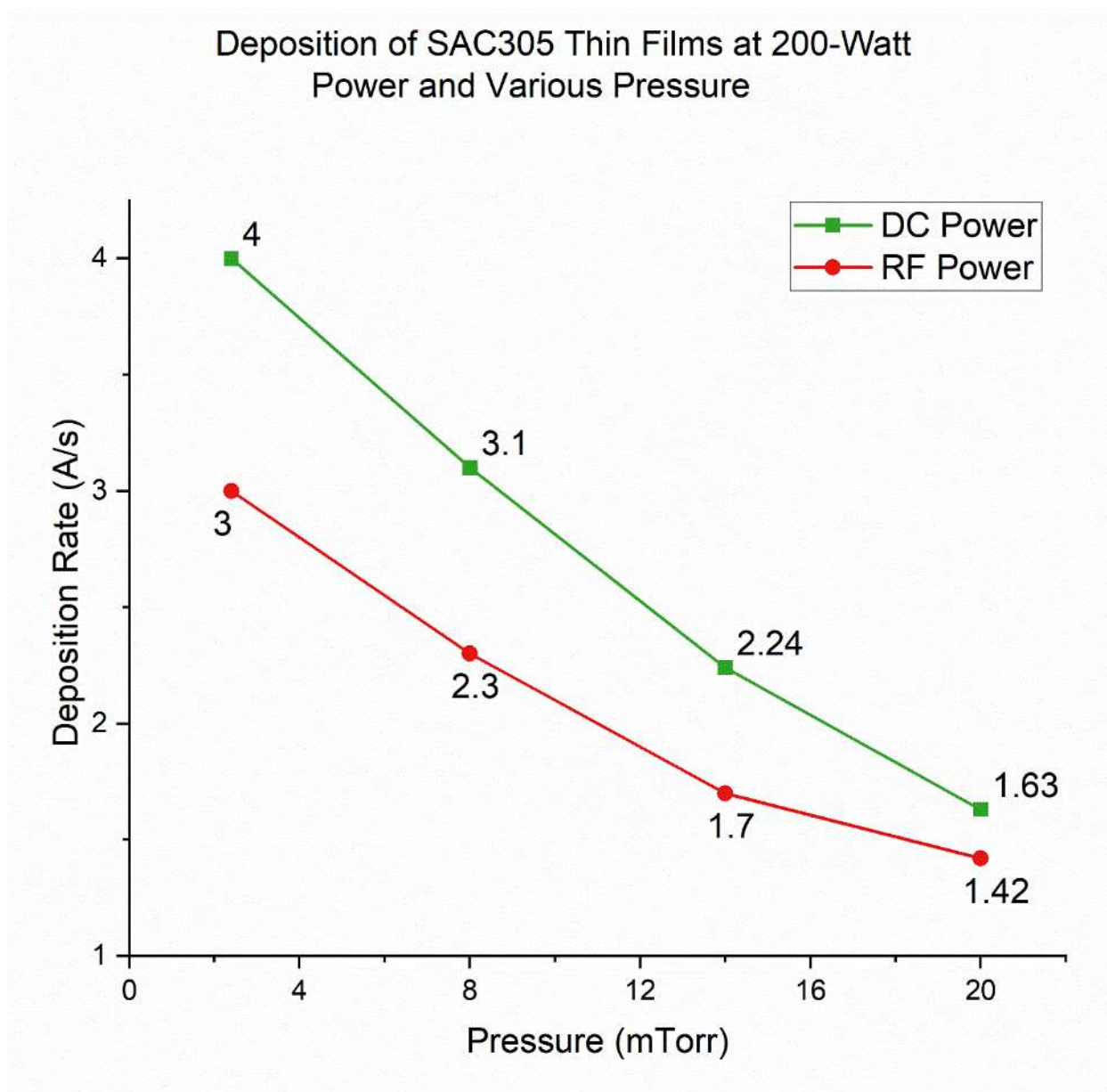


Figure 4.7 Investigating Variable Pressure Effects in Magnetron Sputtering Deposited SAC305 Thin Films at 200-Watt Power and Various Pressures.

Interestingly, the disparity in deposition rates between the two methods is minor at lower pressures, registering a difference of just 0.21 Å/s at 2.4 mTorr. However, this gap widens

significantly as the pressure increases, reaching a difference of 1 Å/s at 20 mTorr. Notably, RF sputtering exhibits a more pronounced reduction in deposition rate at higher pressures, attributed to increased atomic scattering.

At low deposition pressures (2.4 mTorr), SAC305 films exhibited a uniform and larger grain structure. However, as the pressure increased, the grain structure became less distinct, giving way to smaller grains accompanied by voided boundaries on the films. Upon reaching higher pressures (20 mTorr), a more significant number and broader extent of voided boundaries were observed. The increase in sputtering pressure leads to a decrease in the kinetic energy of sputtered adatoms as they undergo a higher number of collisions with Ar gas. This reduced kinetic energy of sputtered adatoms consequently diminishes the surface mobility of the adatoms, hindering their ability to aggregate and grow, resulting in a more porous film microstructure.

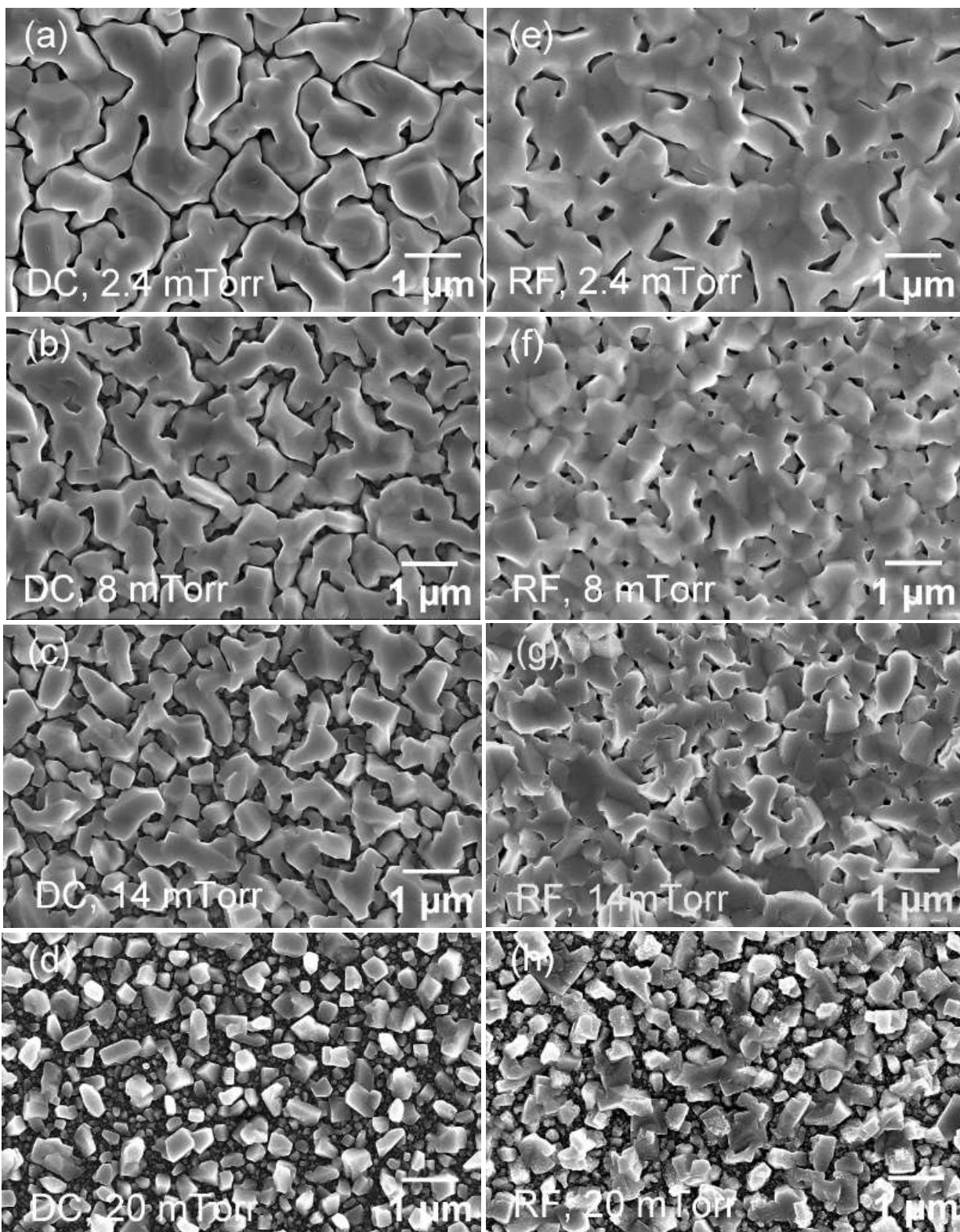


Figure 4.8 FE-SEM Images of the Thin SAC305 Film Surface Area Deposited at 200W through DC and RF Power Source on Si Substrate at Various Pressures

4.4 Conclusion

This study investigated a method to improve the surface morphology of SAC305 thin films by modulating the magnetron sputtering parameters and annealing temperatures to produce smooth SAC305 thin films. The industry-standard RCA cleaning procedure prepared Si substrates. This grain size was determined using FE-SEM images, and the measurements were analyzed using the ImageJ software. When deposited using 200-watt power and 4 mTorr pressure at room temperature, the film displayed a porous structure with pronounced grain boundaries. Elevating the substrate temperature did not enhance the film's morphology; it deteriorated. Specifically, at 50 °C, the morphology remained consistent, while at 75 °C, larger grains emerged, and at 100 °C, the grains appeared disconnected and porous, suggesting complete melting. When annealed at varying temperatures and durations, films showed minimal changes up to 210 °C for 1 to 3 h. However, the film underwent significant changes at 220 °C for an hour, including grain growth and fragmentation. Despite these changes, the overall film quality remained unchanged, prompting a shift in focus to non-annealed films and the exploration of sputtering parameters. The SAC305 films were deposited at various pressures and power.

With increased sputtering power, the deposition rate correspondingly increased for both DC and RF sputtering techniques. This trend was driven by the Ar ion flux and its energy during target collisions. Higher power intensifies ion-target interactions and the likelihood of ions removing target atoms, which are linked to the voltage and power, thereby enhancing the deposition rate. Lower power levels produced porous films with smaller grain sizes for both techniques, but RF films exhibited more voids than films deposited with DC power. As power was increased, DC films displayed denser grains, while improvements in RF films were more

pronounced at higher power. Finally, the optimal surface morphology for SAC305 was achieved using an RF power source with a 200 W power at room temperature.

The deposition rates of SAC305 films were investigated under varying deposition pressures ranging from 2.4 mTorr to 20 mTorr at a constant 200 W DC and RF power supply. The deposition rate decreased as the deposition pressure for SAC305 films increased from 2.4 mTorr to 20 mTorr, using both DC and RF power supplies set at 200 W. This decline is attributed to increased collisions between sputtered SAC305 atoms and Ar ions in the chamber, especially at higher pressures. Due to a shorter MFP, the heightened collision likelihood causes some sputtered particles to deviate from the substrate, resulting in a slower deposition rate.

At lower pressures, such as 2.4 mTorr, the films display a more uniform and larger grain structure. However, as the pressure was increased, the grain structure became less distinct, leading to the emergence of smaller grains and pronounced voided boundaries. This transformation becomes even more evident at pressures as high as 20 mTorr. The underlying reason for these morphological changes is the reduced kinetic energy of the sputtered adatoms due to increased collisions with Ar gas at higher pressures. This energy reduction limits the adatoms' surface mobility, impeding their coalescence and growth, resulting in a porous film structure.

CHAPTER 5

FABRICATION AND CHARACTERIZATION OF MAGNETRON SPUTTERED SAC305 THIN FILMS

5.1 Introduction

The preceding chapter focused on optimizing the surface morphology of SAC305 thin films deposited on Si(100) substrates. Fine-tuning various magnetron sputtering parameters, including substrate conditions, achieved this result. The study concluded that the most favorable surface morphology was obtained under low chamber pressure and high power supplied by an RF power source. Specifically, a film deposited at a chamber pressure of 2.4 mTorr and an RF power level of 200 W demonstrated superior surface characteristics compared to other samples before polishing. However, even the best-performing sample exhibited a surface that was still too rough for precise AFM measurements. This limitation was attributed to the constraints in the resolution of the AFM tip. The current chapter explores additional techniques to enhance the surface morphology of SAC305 thin films.

The substrate's surface properties, including its surface energy and crystal structure, affect the nucleation and growth of the thin film, which, in turn, influences its microstructure, morphology, and properties. A substrate with high surface energy can promote adhesion and nucleation of the thin film, leading to a smoother and more uniform film. On the other hand, a substrate with low surface energy can result in poor adhesion and uneven film growth. If the lattice structure of the substrate matches that of the thin film, it can lead to epitaxial growth, resulting in a high-quality, ordered film. However, if the substrate's crystal structure differs from

the thin films, it can result in polycrystalline or amorphous films with lower quality and irregularities. [115-118]

Silicon, gallium arsenide, and sapphire are used in the semiconductor industry for various applications. Silicon is the most widely used semiconductor material because it is abundant, easy to process, and has good electrical properties. Silicon is used to fabricate most integrated circuits, which are the building blocks of electronic devices and solar cells [119]. Gallium arsenide is a compound semiconductor with higher electron mobility and a wider bandgap than silicon, making it better suited for high-frequency and high-power applications. Gallium arsenide is used in microwave, radio-frequency, and optoelectronic devices [120]. Sapphire is a crystalline form of aluminum oxide (Al_2O_3) used as a semiconductor material. Sapphire has a high thermal conductivity, which makes it useful in high-temperature applications, and it is transparent in the visible and infrared regions of the electromagnetic spectrum, which makes it useful in optoelectronics [121].

In this research, SAC305 films were deposited on silicon (Si), gallium arsenide (GaAs), aluminum oxide (Al_2O_3), and glass (SiO_2) to examine their surface morphology. The films exhibiting the most optimal surface morphology were then polished using an abrasive colloidal silica (SiO_2) suspension with a particle diameter of $0.02 \mu\text{m}$ to attain a smoother film surface. The Sn films' surface morphology and crystal structure were analyzed using FE-SEM and XRD, and their roughness was measured with an AFM.

5.2 Experimental Setup

5.2.1 Substrate

This study's methodology and deposition parameters are consistent with those detailed in Chapter 4. Before deposition, all the wafers underwent a standard RCA cleaning process followed by ultrasonic cleaning in acetone for 3 min. Ten cm diameter substrates were acquired from University Wafers, from which a 2 cm by 2 cm was sectioned for deposition. A 2-in diameter SAC305 target with a thickness of 0.25 in and 99.99% purity was acquired from ACI alloys. SAC305 films were deposited at room temperature using an ATC Orion-5 magnetron sputtering machine with a 20 SCCM constant flow rate of Ar gas. Before deposition, the chamber base pressure ranged between 3×10^{-5} Pa and 9×10^{-5} Pa. Specifically, and samples were deposited at a chamber pressure of 2.4 mTorr and an RF power level of 200 W, conditions that have been previously shown to produce superior surface morphology.

5.2.2 Polishing

An allied multi-prep high-precision mechanical polishing system using high-density, non-woven, low-nap porous cloth was used to polish the SAC305 thin film (Figure 5.1). A mixture of abrasive colloidal Silica (SiO_2) suspension of 0.02 μm diameter and red lube in a 1:3 ratio was used for an ultra-fine surface finish. The polishing was performed at a minimum load for 2 min, removing 400 nm of surface material. The polished sample was then cleaned with ethanol in an ultrasonic cleaner for 3 min and dried with a high-pressure nitrogen blower to remove SiO_2 suspension particles.

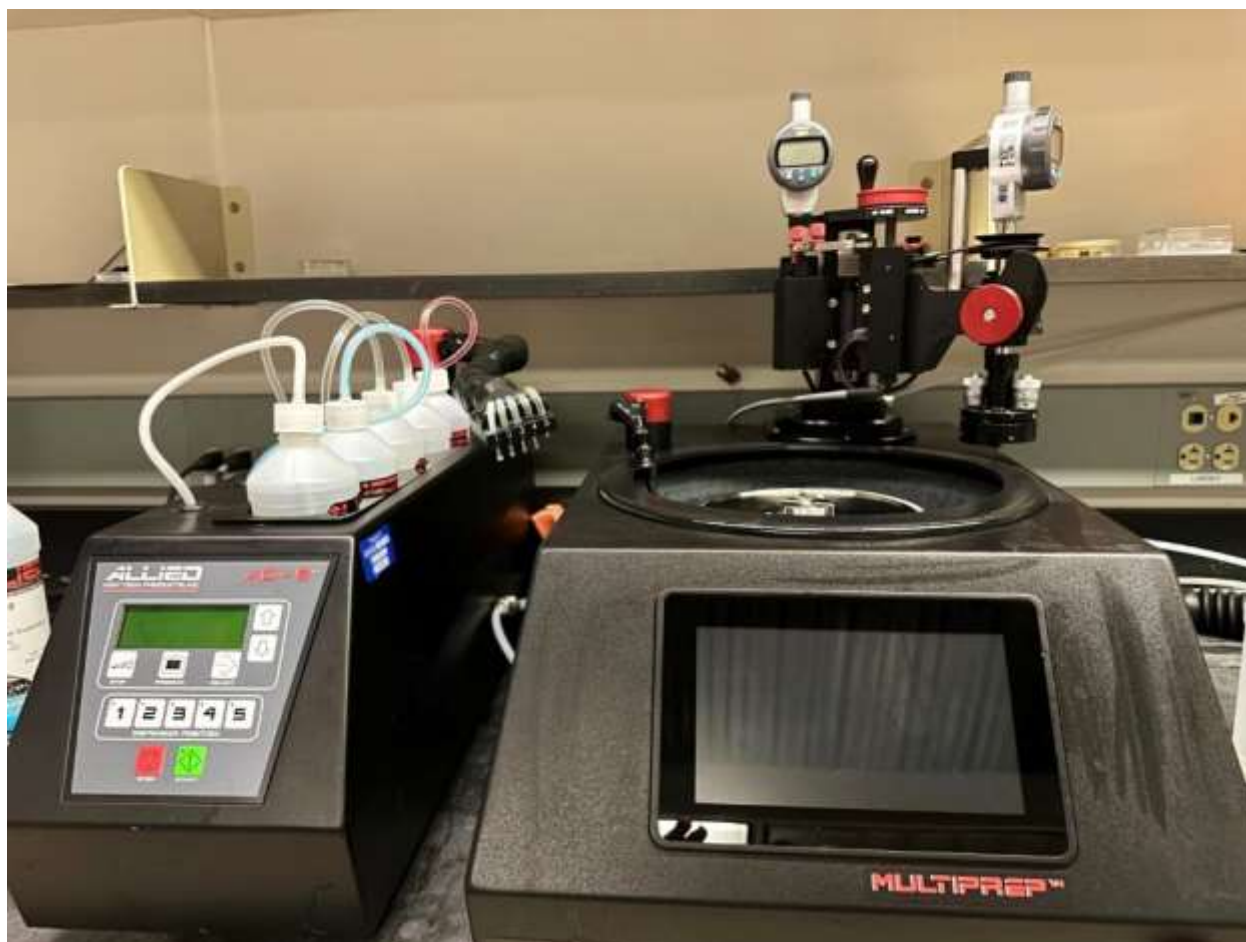


Figure 5.1 Allied High-Tech Multi-Prep Polishing System and Automatic Fluid Dispenser

5.2.3 *FE-SEM and EDS*

A comprehensive discussion of the Hitachi S-4700 FE-SEM can be found in the preceding chapters. Beyond morphological analysis, the Hitachi S-4700 is equipped with EDAX EDS capabilities, enabling elemental composition analysis of the samples investigation. After polishing the thin films using SiO₂ suspension particles, traces of these particles were found on the film's surface. The films were cleaned with ethanol and ultrasonic to eliminate the SiO₂ particles. EDS analysis was conducted to verify the complete removal of the SiO₂ particles post-cleaning

5.2.4 XRD

The crystal structures of the films were studied by XRD (Miniflex II, Rigaku, Japan) using CuK α radiation ($\lambda = 1.54056 \text{ \AA}$) (Figure 5.1). The XRD patterns of the films obtained before and after polishing and the diffraction peaks of the as-deposited SAC305 films on various substrates were compared to understand Nb₃Sn formation after annealing. Scherrer's equation calculated the average crystallite size of different diffraction orders from the peak broadening.

$$D = \frac{K\lambda}{B \cos \theta} \quad (15)$$

In this equation, K represents the shape factor, while λ is the wavelength of the incoming X-ray. B denotes the full width at half maximum (FWHM) of the diffraction peak, expressed in radians, and θ is the angle of diffraction. The lattice parameter was subsequently determined based on the following equation.

$$\frac{1}{d^2} = \frac{h^2+k^2+l^2}{a^2} \quad (16)$$

where d is the lattice spacing, a is the lattice parameter, and h, k, l are Miller indices representing the crystal plane.



Figure 5.2 Image of XRD (Miniflex II, Rigaku, Japan)

5.2.5 AFM

The roughness of the sample surfaces was measured using a Dimension 3100 AFM from Veeco (Figure 5.3). The AFM tip, composed of monolithic silicon, features a tip radius under 10 nm, a force constant of 40 N/m, and a resonant frequency ranging from 200 to 400 kHz. Data were gathered from samples in tapping mode, with a scan dimension of 30 μm x 30 μm . Both the root mean square (RMS) roughness and the variations in height from peak to valley across the films were computed through the analysis of AFM images, utilizing Nasoscope Analysis version 2.0 for image processing.



Figure 5.3 Atomic Force Microscope (AFM)

5.3 Results and Discussion

5.3.1 FE-SEM

Figure 5.4 shows the FE-SEM image of the SAC305 thin films deposited on (a) silicon, (b) gallium arsenide, (c) sapphire, and (d) glass substrates. Samples deposited on silicon (Si), gallium arsenide (GaAs), and aluminum oxide (Al_2O_3) substrates exhibited porous structures with interconnected nanoparticles. In contrast, those on glass substrates (SiO_2) resulted in

distinct, variably sized, and shaped nanoparticles. This discrepancy may be attributed to the lower wettability of tin (Sn) particles on glass substrates [122].

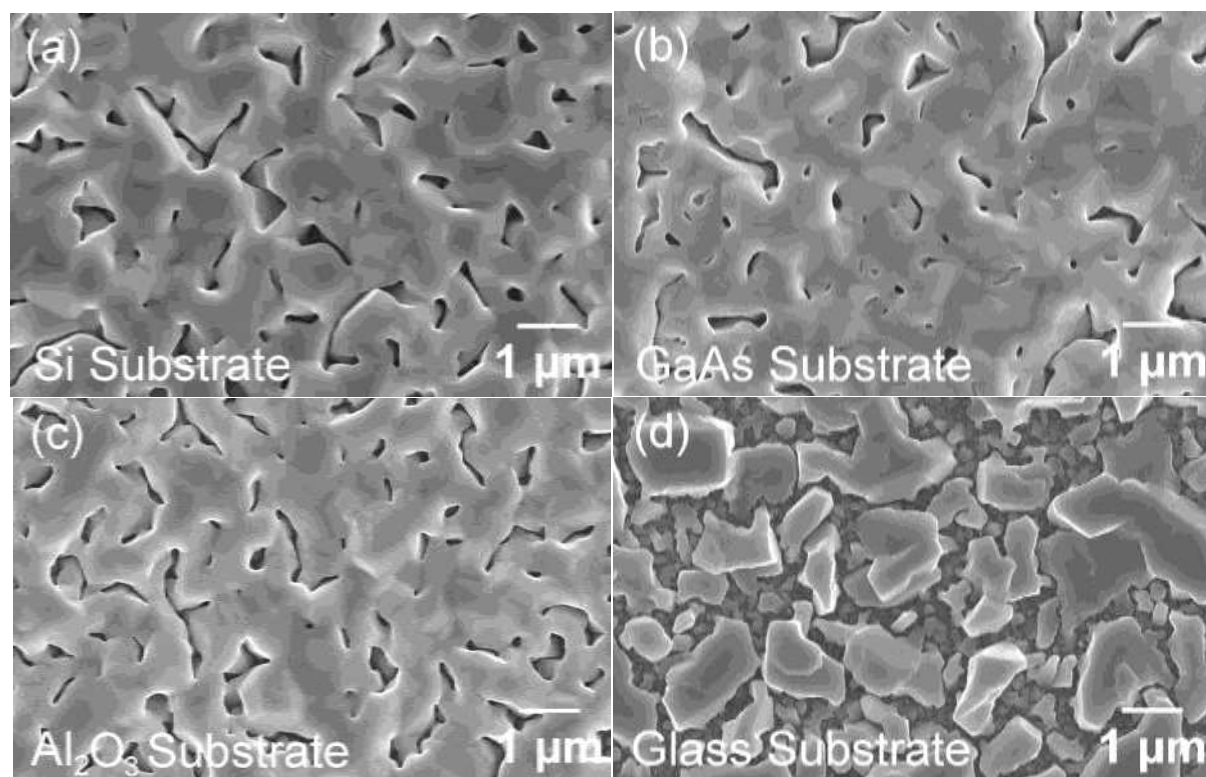


Figure 5.4 FE-SEM Images of the Thin SAC305 Film's Surface Area Deposited at 2.3 mTorr Pressure through 200W RF Power on Various Substrates.

5.3.2 XRD

Figure 5.5 displays the $2\theta/\omega$ XRD diffraction pattern for SAC305 thin film on various substrates. Samples were composed of polycrystalline β -Sn grains, with a preferred orientation at 2θ of 30.70° diffracting from the (200) plane. Weaker peaks of β -Sn were observed at 2θ of 32.09° , 43.97° , 45.00° , 55.46° , 63.93° , 72.59° , and 73.34° , corresponding to diffractions from

the (101), (220), (211), (301), (400), (420), and (411) plane. Ag peaks were not present in the XRD pattern; however, weak peaks of Ag₃Sn were observed at 2θ of 37.60° and 39.59° , corresponding to diffractions from the (020) and (211) plane. The XRD diffraction pattern outcomes indicate that sputtered Ag adatoms are completely alloyed with the Sn layer. No other peaks attributed to Cu and Cu₆Sn₅ were found. The absence of an Ag peak could be because wt.% of Cu in SAC305 is 0.5%, significantly lower than the 2% detection limit of the XRD.

The Si substrate exhibited a prominent peak at an angle of 69.15° , corresponding to the (400) plane. In contrast, a less intense peak was observed at 33.04° , associated with the (200) plane. For GaAs, a peak was detected at 31.46° , originating from the (200) plane. Notably, no peaks corresponding to Al₂O₃ and SiO₂ were observed in the case of sapphire and glass substrates.

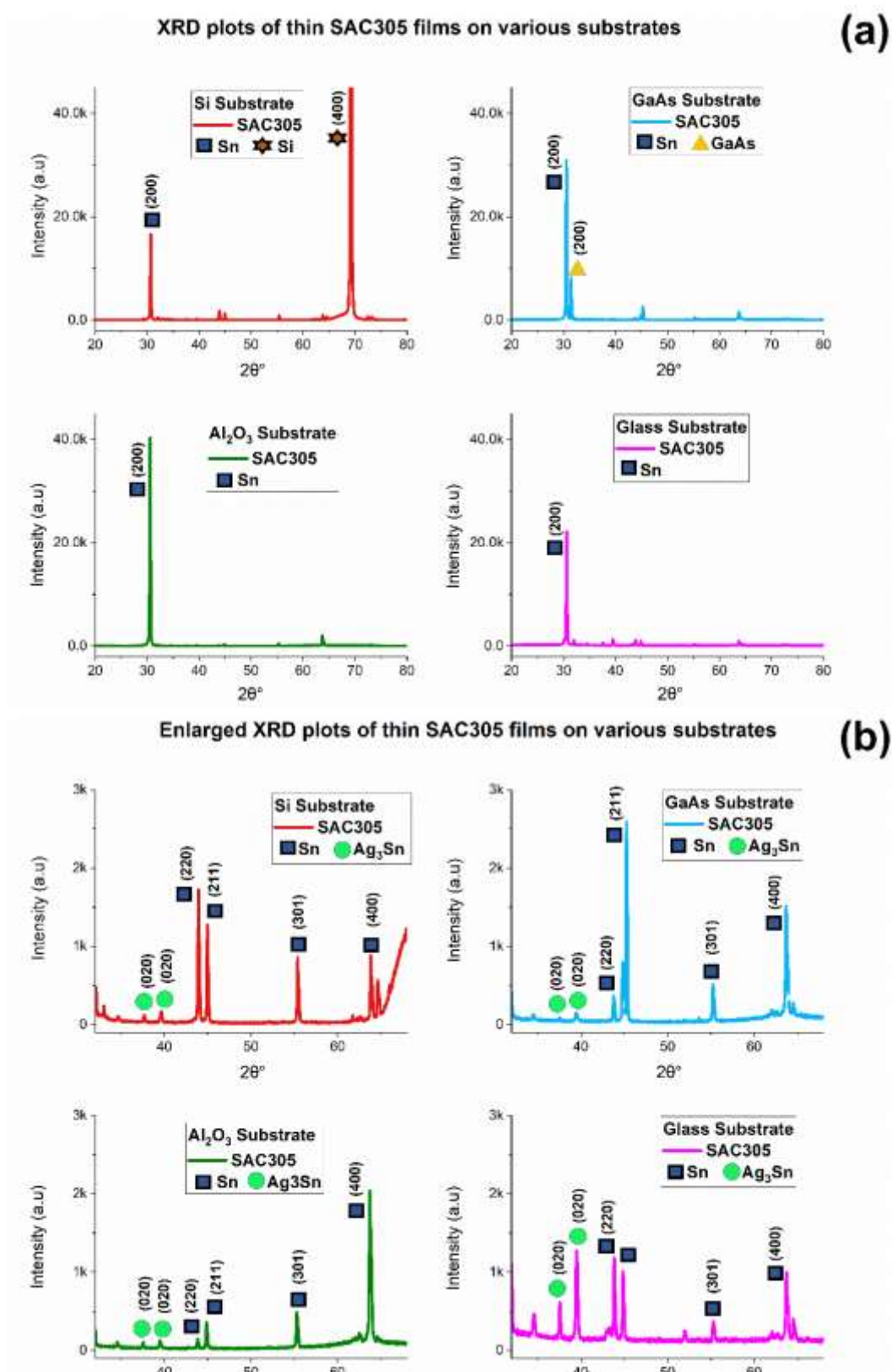


Figure 5.5 (a) XRD Plot of the Thin SAC305 Films on Various Substrates.

(b) Enlarged Plots.

5.3.3 *Polishing*

Attention was redirected towards polishing SAC305 thin films to enhance the surface morphology. A SAC305 thin film deposited on a Si substrate was explicitly selected for this polishing treatment. Sample #4, deposited with an RF power source at a pressure of 2.4 mTorr and a power of 200 W, demonstrated the most optimal surface morphology among all the samples.

Figure 5.6 illustrates the FE-SEM images of the SAC305 thin film (sample #4) deposited on a Si(100) substrate before and after polishing, including the top surface morphology and cross-sectional area. Specifically, Figure 5.6 (a) and (c) show the top surfaces before and after polishing, respectively, while Figure 5.6 (b) and (d) represent the cross-sectional areas before and after polishing, respectively. Before polishing, the sample exhibited a polycrystalline structure with a grain size of approximately 1 μm in diameter, as shown in Figure 5.6 (a). The cross-sectional image of the 2 μm thick film shown in Figure 5.6 (b) revealed narrow cones and deep valleys with a peak-to-valley distance of 400 nm. Five hundred nm of top surface material was removed, succeeding a 2-min polishing period.

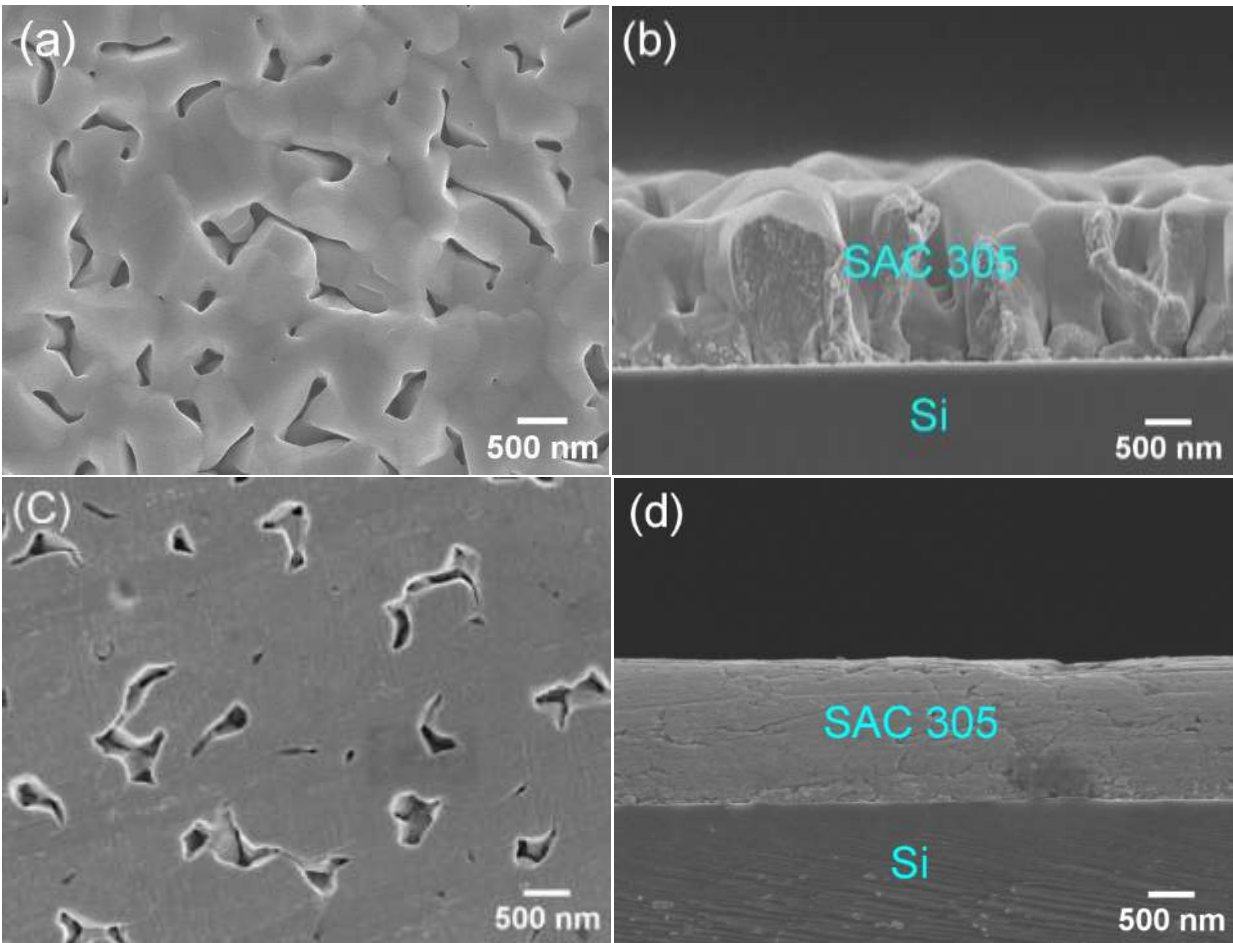


Figure 5.6 FE-SEM Image SAC305 Thin Film Deposited at 200W RF Power and 2.4 mtorr Pressure on Si Substrate. (a) The Surface Area Before Polishing. (b) Cross Section Area Before Polishing. (c) Surface Area After Polishing for 2 mins. (d) Cross Section Area After Polishing for 2 mins. Reproduced with Permission from Manish Ojha, Yousuf Mohammed, Donald Stone, and A.A. Elmustafa, *JVST B* 41 (5), 10.1116/6.0002949,

The sample was subsequently cleaned with ethanol in an ultrasonic cleaner for 3 min to remove any SiO₂ suspension particles. The polishing process resulted in a smooth and continuous surface with a uniform thickness of 1700 nm. No traces of Si particles were detected by EDS, indicating that the ultrasonic cleaning process had completely removed SiO₂ particles. The elemental distribution of Sn, Ag, and Cu are represented by cyan, green, and yellow colors, respectively (Figure 5.7).

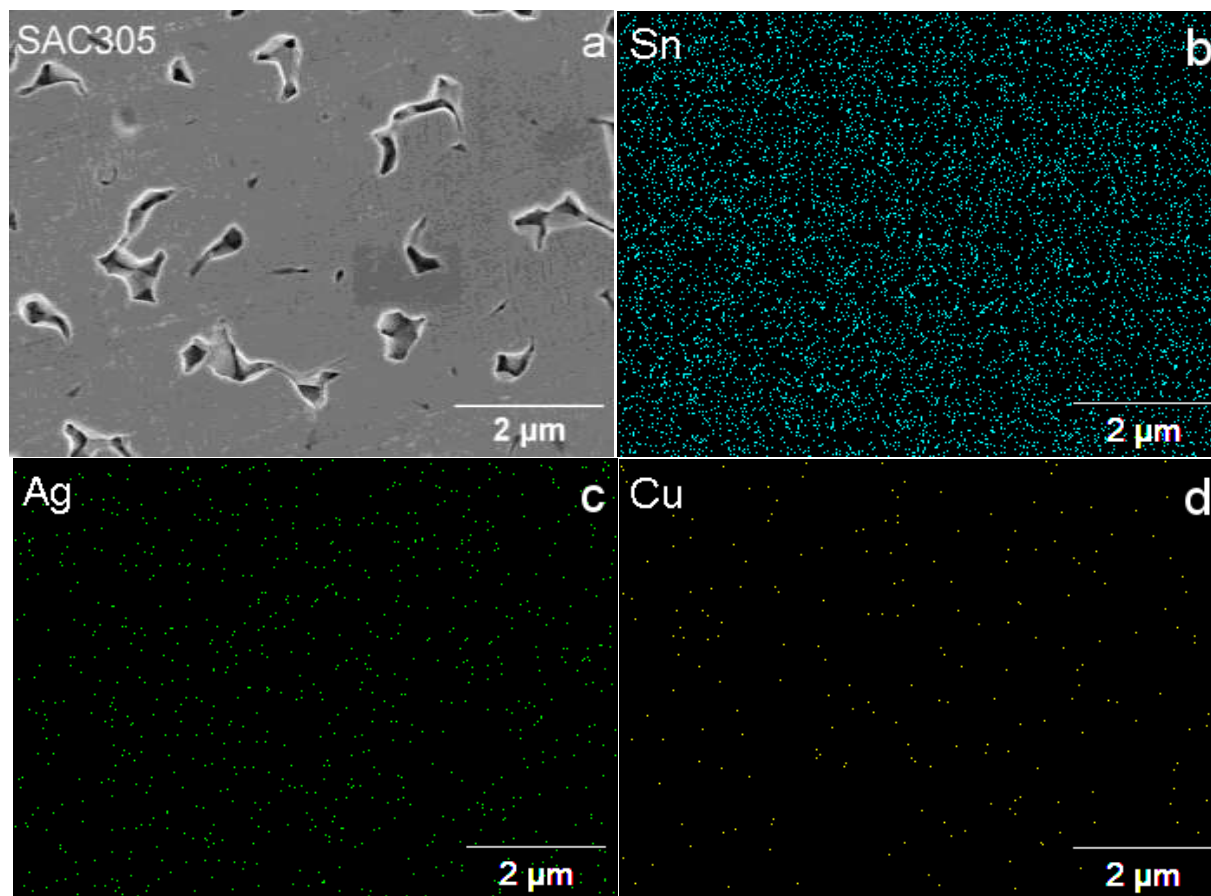


Figure 5.7 The EDS Spectral Analysis for the Elemental Composition of Polished SAC305 Thin Film After Ultrasonic Cleaning. (a) Mapping Surface Area, (b) Elemental Distribution of Sn, (c) Elemental Distribution of Ag, (d) Elemental Distribution of Cu. Reproduced with permission from Manish Ojha, Yousuf Mohammed, Donald Stone, and A.A. Elmustafa,

5.3.4 AFM

Figure 5.8 shows an AFM image measuring a $30\ \mu\text{m} \times 30\ \mu\text{m}$ scan area and a z-thickness (height) profile of a SAC305 polished film. Accurate AFM measurements of the rough, unpolished SAC305 thin film could not be obtained due to the limitations in AFM tip resolution.

The reported values for the polished SAC305 thin film for mean roughness (Ra) and root-mean-square roughness (Rq) are 16.9 nm and 24.6 nm, respectively. These roughness values show the significant improvement in surface roughness achieved by polishing the SAC305 thin films.

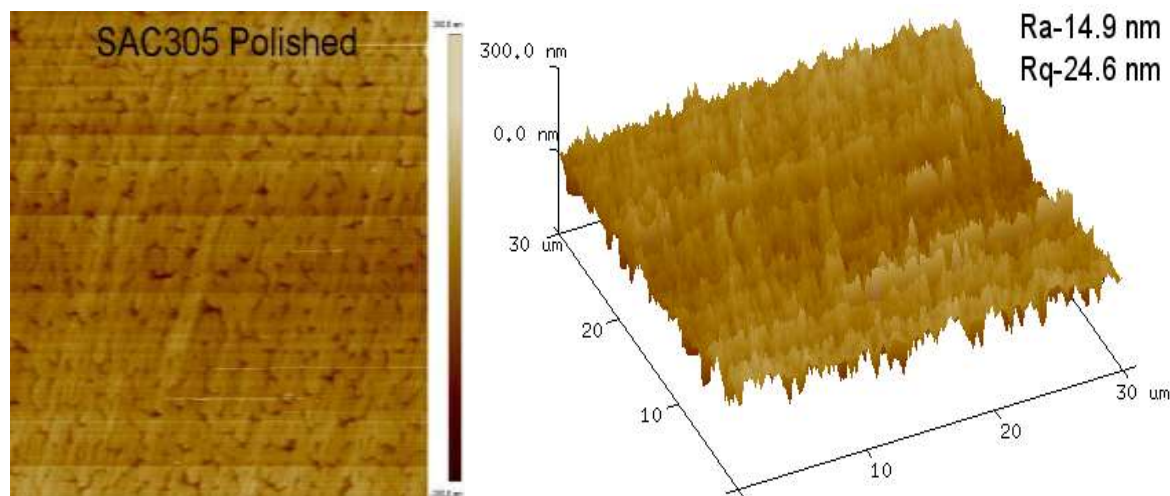


Figure 5.8 AFM images of ($30\mu\text{m} \times 30\mu\text{m}$) scan size of polished SAC305 films on Si substrate. Reproduced with permission from Manish Ojha, Yousuf Mohammed, Donald Stone, and A.A. Elmustafa, *JVST B* 41 (5), 10.1116/6.0002949, (2023). Copyright 2023

5.4 Conclusion

This study examined the properties of SAC305 thin films deposited on (a) silicon, (b) gallium arsenide, (c) sapphire, and (d) glass substrates. Samples on Si, GaAs, and Al_2O_3 substrates showed porous structures with linked nanoparticles. However, samples on glass (SiO_2) depicted rough surfaces with variably sized and shaped nanoparticles. The difference might be due to tin (Sn) particles' reduced wettability on a glass substrate.

XRD diffraction patterns showed polycrystalline β -Sn grains with a primary orientation at 2θ of 30.70° from the (200) plane. While Ag peaks were absent, suggesting a complete alloying of sputtered Ag adatoms with the Sn layer, weak peaks of Ag_3Sn were detected. The absence of Cu and Cu_6Sn_5 peaks is likely due to the low wt.% of Cu in SAC305, below the XRD's detection limit. The Si substrate displayed a significant peak for the (400) plane, whereas GaAs showed a peak for the (200) plane. Interestingly, no peaks were identified for Al_2O_3 and SiO_2 in sapphire and glass substrates, respectively.

The film, deposited using an RF power source at 2.4 mTorr and 200 W on a Si substrate, was chosen for polishing. This decision was based on its superior surface morphology compared to other samples before polishing. After polishing, the sample surface exhibited a uniform, robust, and continuous film. The polishing process involved using abrasive SiO_2 suspension particles, which were then completely removed by ultrasonic cleaning with ethanol. The AFM's limitations in tip resolution prevented precise measurements of the unpolished SAC305 thin film's roughness. However, after polishing, the SAC305 thin film markedly improved surface roughness, with mean roughness (R_a) and root-mean-square roughness (R_q) values recorded at 16.9 nm and 24.6 nm, respectively. The result shows the significant improvement in surface roughness achieved by polishing the SAC305 thin films.

CHAPTER 6

MECHANICAL AND ELECTRICAL CHARACTERIZATION OF MAGNETRON SPUTTERED SAC305 THIN FILMS

6.1 Introduction

The previous chapter detailed the optimization of SAC305 thin film surface morphology on Si(100) substrates by adjusting magnetron sputtering parameters and substrate conditions. The best surface was achieved at 2.4 mTorr chamber pressure and 200 W RF power. This film showed superior traits before polishing, and post-polishing, the sample surface exhibited a uniform, robust, and continuous film.

This chapter examines the influence of length scales (grain size and volume of deformed material) on the time-dependent stress-deformation response of SAC305 thin films. The nanoindentation creep methods described below investigated microscopic structures' local properties and deformation mechanisms, such as solder joints. This study employed these methods to investigate the hardness and strain rate sensitivity of the hardness in thin films and bulk SAC305 solder alloys. In addition, the study reported the electrical resistivity of the thin films and SAC305 bulk material using a FPP.

6.2 Experimental Details

6.2.1 Nanoindentation

A nanoindenter XP equipped with a three-sided diamond Berkovich probe was used in conjunction with the CSM in-depth and load control modes to perform nanoindentation creep experiments and measure the hardness and creep properties of the SAC solder materials (Figure 6.1). The CSM technique uses a stock method (G-Series CSM Standard Hardness, Modulus, and

Tip Cal) that produces the evolution of hardness as a continuous function of the penetration depth into the surface by superimposing a small harmonic force oscillation, resulting in a harmonic displacement oscillation of 1 nm or less, on the tip during the loading cycle. The data acquisition rate was varied for different segments of the tests to enable adequate data collection depending on the segment's duration. A time constant of 1 ms was employed for faster loading tests, enabling faster data acquisition. For CSM tests, a series of indents possessing different combinations of strain rates of loading, PHT, and unload were employed. These nanoindentation parameters allowed contact stiffness and the sample's mechanical properties to be continuously evaluated by analyzing the harmonic force and displacement data, as detailed by Oliver and Pharr [96]. Thermal drift and strain rates during loading were set at 0.05 nm/s and 0.05 s^{-1} , respectively. A stock method was used for the creep experiments to penetrate the films to a desired load or penetration depth. Tests were performed with and without the CSM approach. A single-step loading-unloading approach with the CSM mode off was used for load control tests. The maximum load was kept constant at 10 mN for loading/unloading times of 100, 10, 1, and 0.25 s, corresponding to loading/unloading rates of 0.1, 1, 10, 40, and 100 and strain rates of 0.5, 2, and 5 s^{-1} . The slope of the load and displacement data during the test's unloading segment determined the stiffness of contact. The data were used to determine the sample's mechanical properties using the Oliver–Pharr analysis [96]. The results of this test technique provide the hardness at a specific load and penetration depth. A series of indents with different load combinations, peak hold, and unload times were completed. The surface approach sensitivity was set at 20%, and the allowable drift rate was defined as 0.05 nm/s.



Figure 6.1 Nanoindenter XP Equipped with a Three-Sided Diamond Berkovich Probe.

6.2.2 *Four-Point Probe*

The FPP technique is a widely accepted approach in material science and the semiconductor industries for examining the electrical properties of solids and thin films. Its popularity stems from its minimal sample preparation requirements and high accuracy. Various measurement methods or modes have been established for the traditional FPP, including the van der Pauw, collinear [123], square [124], and probe configuration modes [125]. Among these, the

collinear mode is the most frequently employed method. The principle of the collinear FPP involves directing a current through the outer probe pair.

In contrast, the voltage drop across the internal pair is recorded using a high-impedance voltmeter. The effects of extraneous contact resistances, which can arise from surface oxidation or moisture, are negated by employing four contact points rather than just two. As a result, no added voltage drop occurs due to contact resistance, ensuring an accurate measurement of the sheet resistance. This voltage drop, denoted V , mainly arises on the semiconductor surface because the current, I , flows through the sample. The FPP's resistance, represented by R , is calculated using the formula.

$$R = \frac{V}{I} \quad (17)$$

For a thin film with a uniform thickness (t_s) and an electrical conductivity (σ), the electrical resistivity (R_s) is given by,

$$R_s = \frac{1}{\sigma t_s} \quad (18)$$

The electrical resistivity of the thin film in terms of voltage and current by the collinear FPP method is given by

$$R_s = 4.532 \frac{V}{I} \quad (19)$$

Where 4.532 is the correction factor for thin films.

A bulk sample was obtained to compare the mechanical and electrical resistivity of the deposited SAC305 thin films to that of bulk SAC305 material. This sample was cut from a SAC305 spool wire, 1 mm in diameter, purchased from a local Radio Shack store. The SAC305 film and bulk material resistivities were measured using a FPP.

6.3 Experimental Results

6.3.1 Nanoindentation

The CSM technique was utilized to create an array of 20-25 indentations, following the methodology described in the previous section for both the SAC305 bulk and thin films. This technique ensures a constant loading rate, $\left(\frac{P}{t}\right)$. On the test surface, a default rate of 0.05/s is employed. Constant load creep experiments were conducted using the Load Control Method to determine the creep properties of the films. The loads obtained from the CSM experiments were utilized for these experiments. The details of the indentation creep experiments are provided in Table 6.1. The loading and unloading times were varied between 0.25 seconds and 100 seconds, resulting in different loading and unloading rates. For each loading/unloading combination, the peak load time was set at 10, 30, or 70 s. The combination of loading and unloading strain rates indicated in Table 6.1 are based on

$$(dp/dt)/P = \frac{1}{2(\text{loading or unloading time})} \quad (20)$$

Where dp/dt is the loading or unloading rate, and P is the maximum load. The rate of change of strain with time is given by.

$$\dot{\epsilon} = \frac{1}{\sqrt{A}} \frac{d\sqrt{A}}{dt} \quad (21)$$

Where A is the projected contact area of indentation. The strain rate monitors the changes in the size of the plastic zone beneath the indenter tip. Although it is possible to use two separate values for the loading/unloading strain rates, we used the same strain rate values for loading and unloading.

The substrate effect on the mechanical properties of thin films and coatings cannot be overlooked. Some researchers suggest that to measure the mechanical properties of thin film, the

indentation depth should not exceed 10%–33% of the film thickness [126, 127]. To accurately measure the SAC305 film properties, we fabricated films as thick as 2.2 μm . Furthermore, to conduct a comprehensive analysis, indentations ranging from 10% to 33% of the film thickness were performed on the thin film, and the results of up to 660 nm are well within the acceptable range of obtaining the mechanical properties of the films without the substrate effect.

The nanoindenter tip was driven to 1500 nm, 300 nm short of reaching the Si substrate. The Si substrate undoubtedly impacts the measurements beyond the 600 nm mark. The CSM method was used, and the tip was driven to 1500 nm to obtain information at a maximum depth of indentation of 600 nm. The indentation was used to analyze the mechanical properties of the SAC305 films without the substrate effect. Constant load creep experiments were employed to evaluate the behavior of the thin films utilizing loads ranging from 0.18 to 9.5 mN, as outlined in Table 6.1. Therefore, the analysis conducted in this research is strictly confined to results within the limits of the properties of the thin film without the substrate effect. In the range of loads reported for the creep experiments, the hardness was independent of load and is reported as 175 ± 25 MPa, indicating that the substrate does not influence the reported results.

Table 6.1 Creep Experiments for Bulk and Thin Films.

SAC305 Bulk									
ML	LT	LR	PH	ULT	ULR	ULT/	LSR	ULSR	Experiment
(mN)	(s)	(mN/s)	(s)	(s)	(mN/s)	PHT	(1/s)	(1/s)	method
10	100	0.1	70	100	0.1	1.429	0.005	0.005	LC
10	10	1	70	10	1	0.143	0.05	0.05	LC
10	1	10	70	1	10	0.014	0.5	0.5	LC
10	0.25	40	70	0.25	40	0.004	2	2	LC
10	0.1	100	70	0.1	100	0.001	0.05	0.05	LC
10	0.01	1000	70	0.01	1000	0.001	0.05	0.05	LC
22	117	0.2	30	17	1.3	0.6	0.05	0.05	CSM
SAC305 Thin Films									
9.5	15	0.63	30	15	0.63	0.5	N/A	N/A	LC
5.5	15	0.37	30	15	0.37	0.5	N/A	N/A	LC
1.5	15	0.10	30	15	0.10	0.5	N/A	N/A	LC
0.5	15	0.03	30	15	0.03	0.5	N/A	N/A	LC
0.18	15	0.01	30	15	0.01	0.5	N/A	N/A	LC
0.35	45	0.01	10	3	0.1	0.3	0.05	0.05	CSM

Figure 6.3 illustrates the linear regression analysis of the $\log(H)$ vs. $\log(\dot{\epsilon})$ results for all the indentations on thin films. The slope of this line is 0.12, with a standard error of 0.02, resulting in a strain rate sensitivity of $m = 0.12 \pm 0.02$.

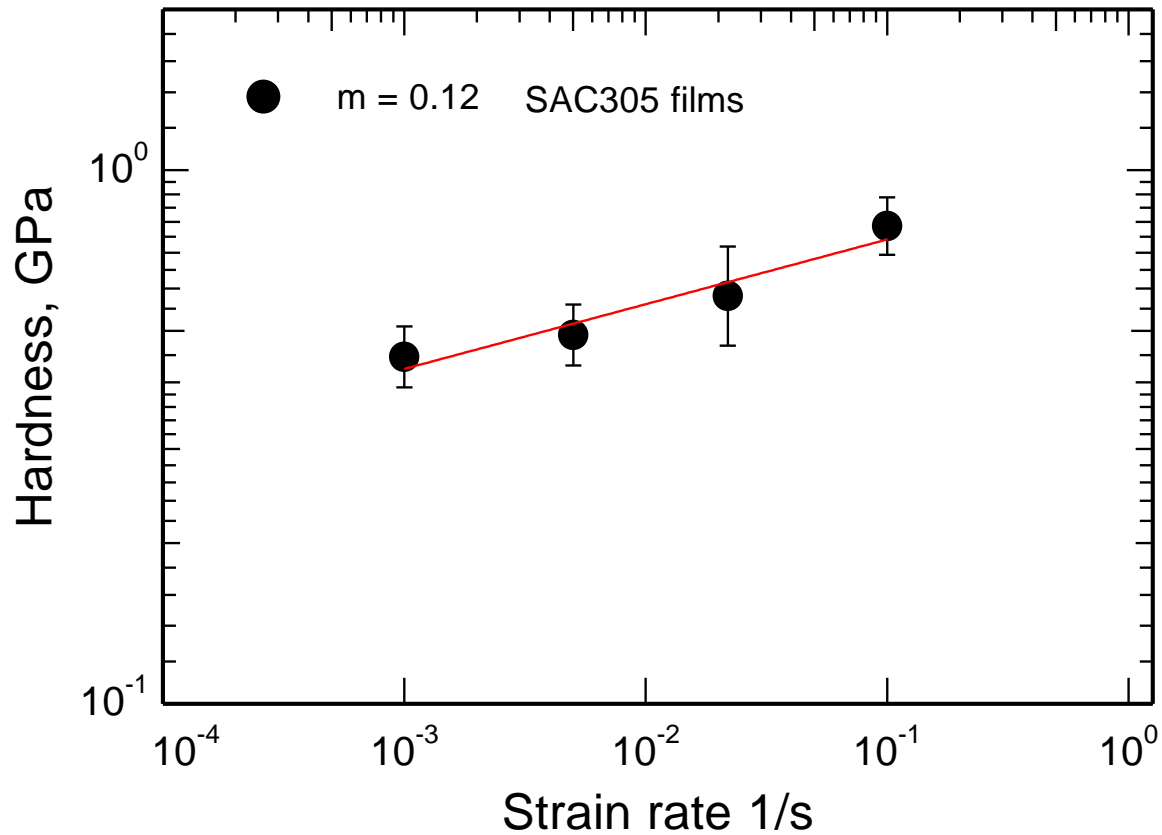


Figure 6.3 SAC305 Thin Film Log (H) vs. Log ($\dot{\epsilon}$) Plot

The data in Figure 6.4 illustrate a series of experiments conducted on bulk SAC305 samples. The initial set of experiments, shown in Figure 6.4a, involved subjecting the samples to loading rates of 0.1, 1, 10, and 40 mN/s, corresponding to 100, 10, 1, and 0.25 s, respectively. The time at peak load was maintained constant at 70 s. Notably, an increase in loading rate was found to increase creep, as demonstrated by the data in Figure 6.4a. In the subsequent experiments, as presented in Figure 6.4b, the loading rate was kept constant at 1 s^{-1} , while the peak hold time was varied between 10 and 70 s. It is concluded that changing the peak hold time has no bearing on the creep deformation. Stegall and Elmustafa (2018) demonstrated that different hold times do not affect the creep properties of the indentation hardness [128]. Finally,

the results obtained for a strain rate of 0.05 s^{-1} and a hold time of 30 s revealed that the creep deformations exhibited reproducibility, leading to similar creep deformation patterns. This observation suggests that various curves have the potential to collapse into a single curve, as illustrated in Figure 6.4c.

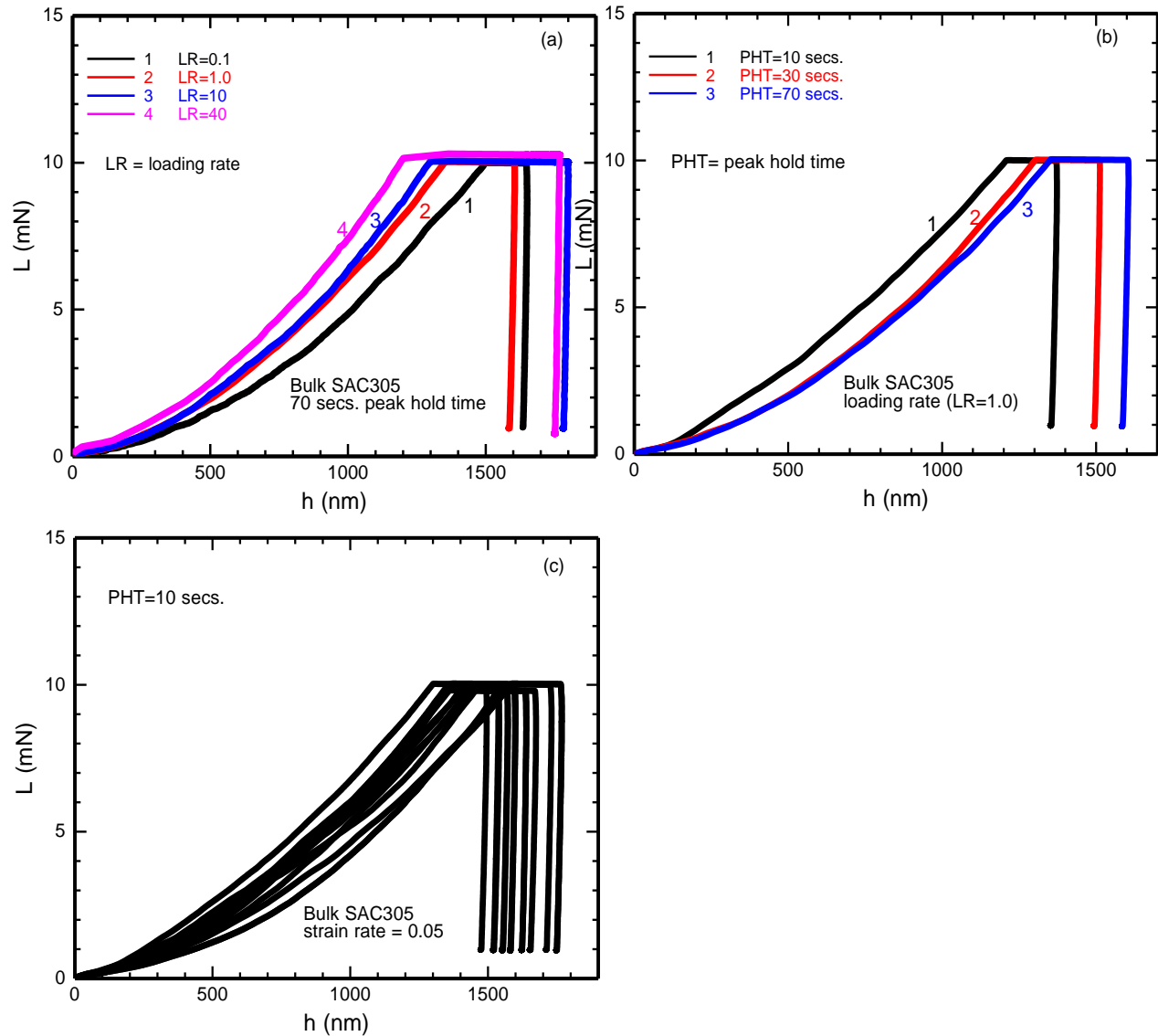


Figure 6.4 Load vs. Total Depth of Penetration in a Creep Experiment for Bulk SAC305 Samples. (a) The Loading Rate (LR) is Varied Between 0.1 mN/s and 40 mN/s While the Unloading Time (ULT) and the Peak Hold Time (PHT) are Held Constant. (b) The LR and ULT are Held Constant While the PHT is Varied Between 10 and 70 sec. (c) The PHT was Set at 10 sec for A Strain Rate of 0.05 1/s. Reproduced with Permission from Manish Ojha, Yousuf Mohammed, Donald Stone, and A.A. Elmustafa, JVST B 41

(5). 10.1116/6.0002949. (2023)

Similar trends for SAC305 thin films were observed, as indicated in Figure 6.5. The load-depth curves represent both constant strain rate and constant load creep experiments conducted on SAC305 thin films with a film thickness of $2.2 \mu\text{m}$. Notably, the loading-unloading curves followed a similar trend to the constant load creep curves while experiencing additional plastic deformation at each constant load, i.e., creep.

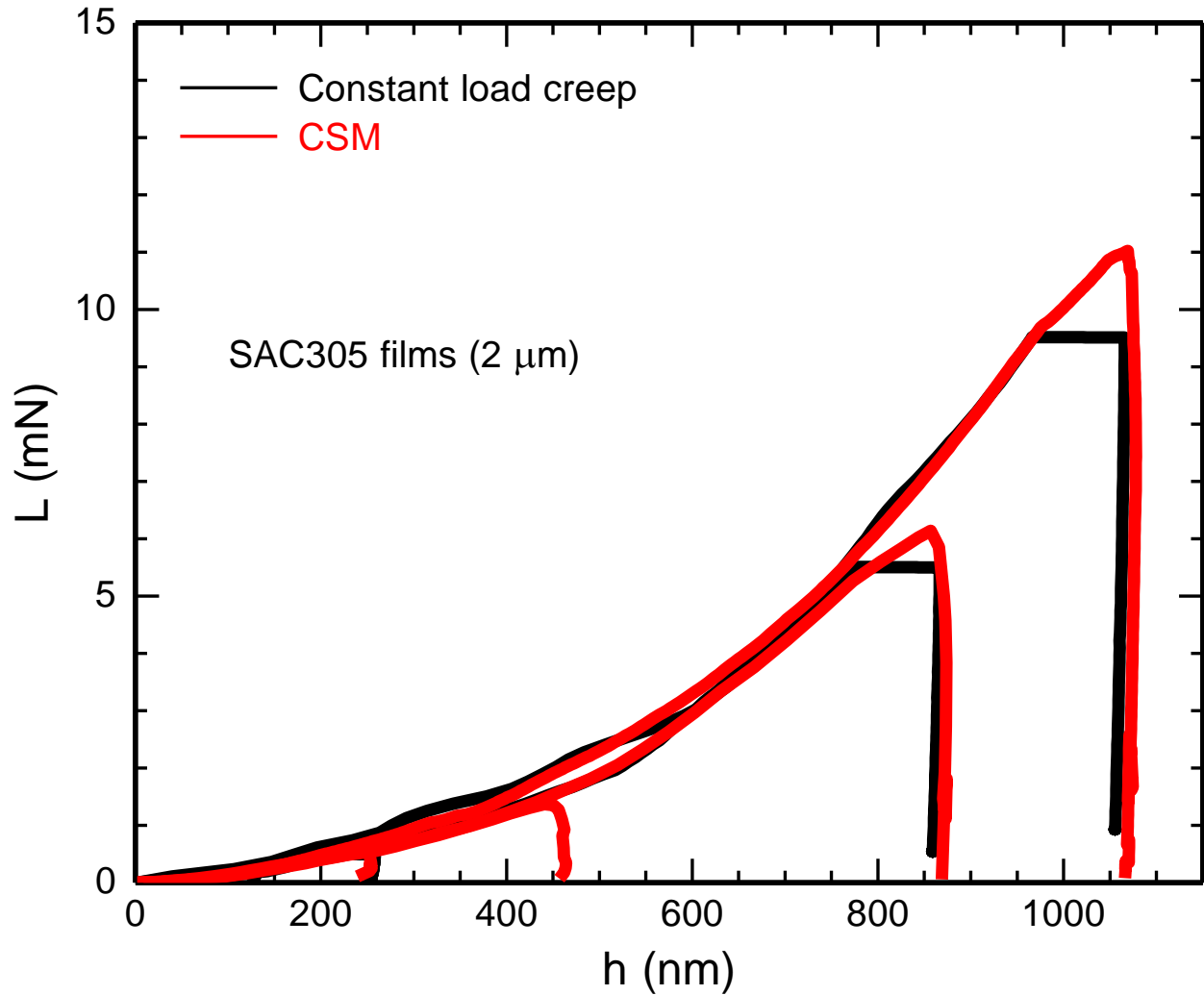


Figure 6.5 Load vs. Total Depth of Penetration in a CSM and Creep Experiments for Thin SAC305 Films. Reproduced with Permission from Manish Ojha, Yousuf

Mohammed, Donald Stone, and A.A. Elmustafa, *JVST B* 41 (5), 10.1116/6.0002949, (2023)

The depth versus time and load versus time curves are plotted in Figure 6.6 from experiments performed at a depth of indentation from 250 to 1100 nm for a total of 60 s for SAC305 thin films. The depth versus time plot depicts the different depths of indentations during

the creep time of 31 s for the different constant loads of 0.5, 1.5, and 5.5 mN, respectively. The penetration depth increased by about 50 nm during the constant load creep, as shown in Figure 6.6 (a).

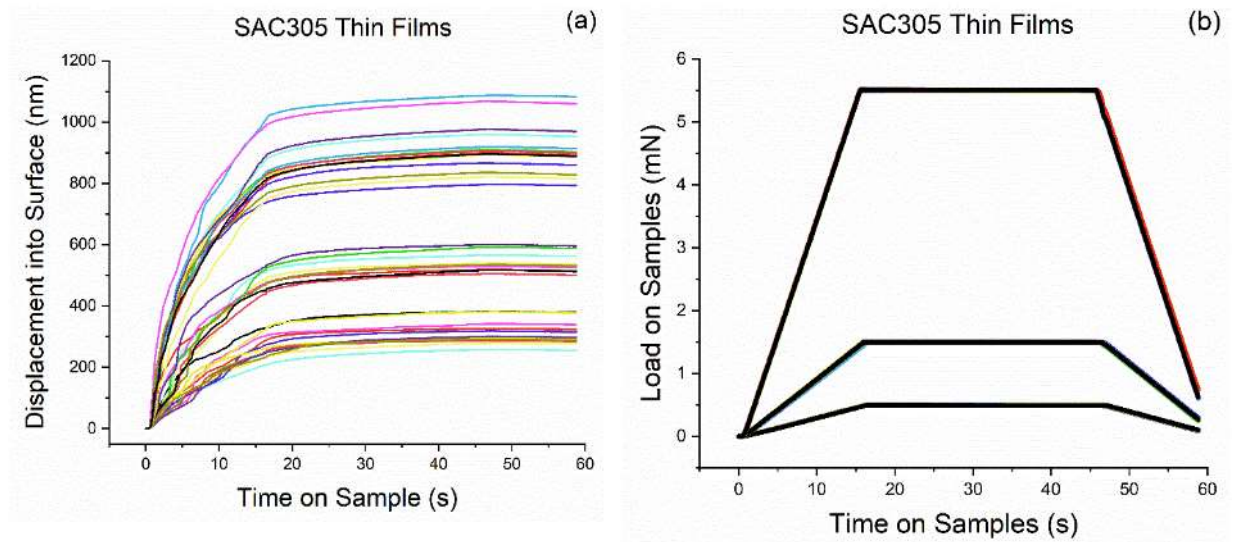


Figure 6.6 (a) Displacement into Surface vs. Time. (b) Load on Samples vs. Time.

Reproduced with Permission from Manish Ojha, Yousuf Mohammed, Donald Stone, and A.A. Elmustafa, JVST B 41 (5), 10.1116/6.0002949, (2023)

The strain rate sensitivity of the hardness, m_H is defined as the slope of the hardness data when plotted versus strain rate. Strain rate is a measure of the creep properties of materials, and each material possesses a unique value of m_H . The strain rate sensitivity is given by [129]

$$m_H = \frac{d \ln H}{d \ln \dot{\epsilon}} \quad (22)$$

The strain rate sensitivity in both bulk and thin film of SAC305 has been evaluated using the CSM and constant load control techniques. The outcomes of these investigations are presented in Figure 6.7, alongside comparative data obtained from conventional testing, as documented in the works of Kariya et al. [130] and Mysore et al.[131].

The data derived from conventional testing of SAC305 concurs closely with the nanoindentation data acquired from both bulk and thin films, as demonstrated in Figure 6.7. The indentation strain rate does not influence the creep properties of SAC305 bulk and thin films during indentation, i.e., the strain rate sensitivity in indentation creep. For most metals, the deformation behavior is assumed to be stress-dependent and, for practical purposes, regarded as time-independent. Consequently, the findings in Figure 6.7 suggest that the strain rate sensitivity of hardness, denoted by the reciprocal slope of the linear regression model fitted to the data, falls within the range of 0.08 - 0.12. Notably, the conventional experimental data reported by Kariya et al. and Mysore et al. [130-131] seamlessly aligns with the nanoindentation data obtained in the present study. Moreover, the strain rate sensitivity results obtained from constant load creep nanoindentation tests conducted on bulk and thin films strongly agree with strain rate sensitivity data obtained from conventional testing methods, as documented in Table 6.2. Specifically, the values of m obtained from the current study range between 0.08 and 0.12.

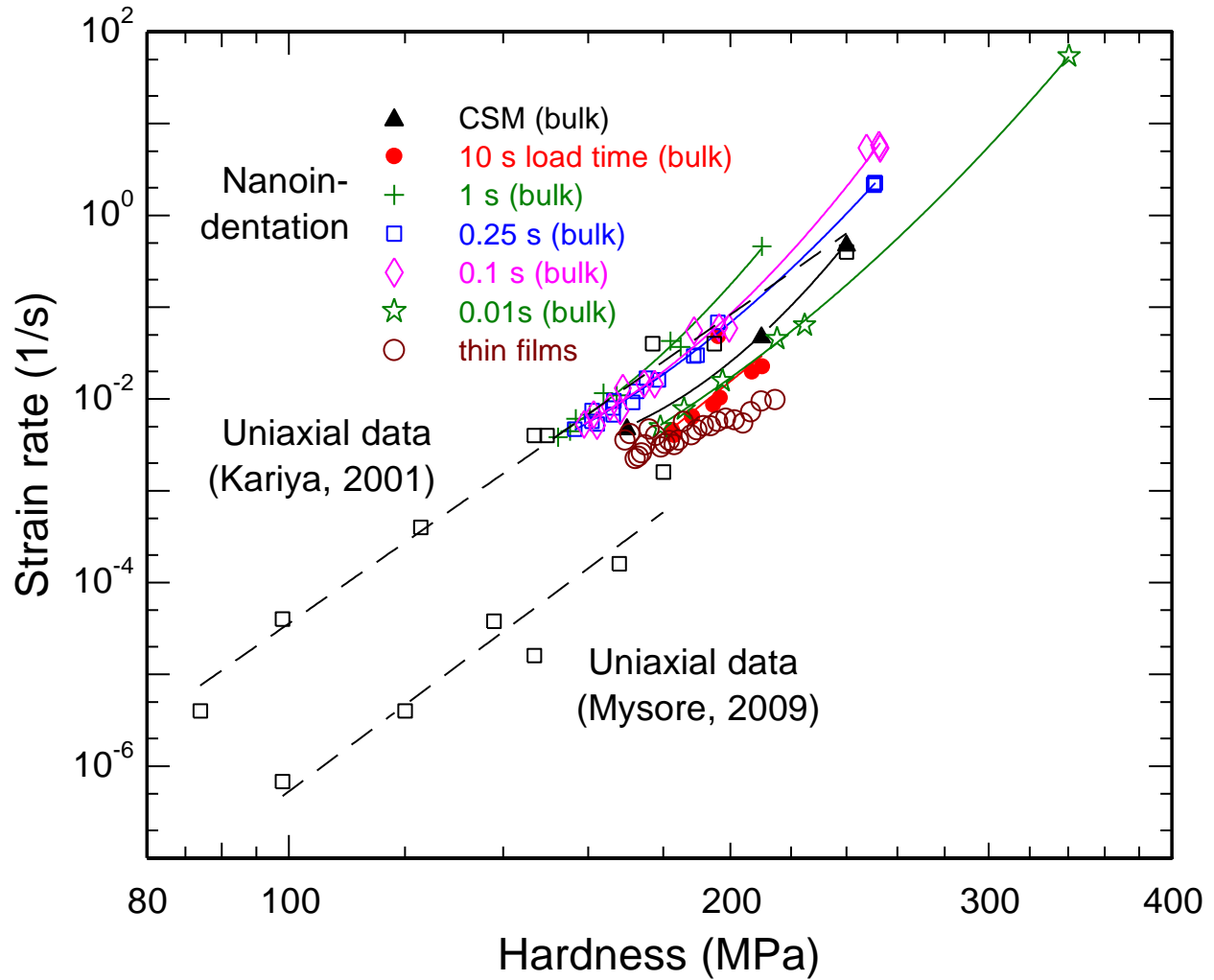


Figure 6.7 Strain Rate of the Indentation Hardness in Nanoindentation Creep and Conventional Testing of SAC305 Bulk and Thin Film Samples. Reproduced with Permission from Manish Ojha, Yousuf Mohammed, Donald Stone, and A.A. Elmustafa, JVST B 41 (5), 10.1116/6.0002949, (2023)

Table 6.2 Strain Rate Sensitivity of the Hardness Results.

Test	Strain rate sensitivity, m_H
Bulk	
CSM	~ 0.11
10 s	~ 0.11
1	~ 0.11
0.25	~ 0.12
0.1	~ 0.11
0.01	~ 0.12
Kariya et al., 2001	~ 0.12
Mysore et al., 2009	~ 0.12
Thin films	~ 0.12

6.3.2 Four-Point Probe

A series of resistivity measurements were conducted at various probe positions on the sample surface. The average electrical resistivity of the polished SAC305 thin film was found to be 19.6

$\mu\Omega$ cm, while the bulk material exhibited a resistance of $13.7 \mu\Omega$ cm. The observed higher resistivity of the thin film is attributed to numerous factors, including surface and grain boundary scattering, interfaces, stresses, and underlying substrates [132-135]. The measured electrical resistance of the SAC305 bulk material closely matches the value of $13 \mu\Omega$ cm reported in the literature [136].

6.4 Conclusion

The mechanical properties and electrical resistivity of the polished thin SAC305 film and bulk material were investigated in this chapter. The electrical resistivity measurement using a FPP on the polished SAC305 thin film and bulk samples revealed slightly higher resistivity for the thin film, attributed to surface and grain boundary scattering, interfaces, stresses, and underlying substrates.

The strain rate sensitivity of the hardness was evaluated for SAC305 bulk and thin film samples using constant load indentation creep and CSM experiments. The average calculated (m) value $\approx 0.10 \pm 0.02$, agrees with literature data from Kariya et al. and Mysore et al., who used conventional methods to obtain similar results.

CHAPTER 7

CONCLUSION

7.1 Conclusion

SAC305 (96.5% Sn-3% Ag-0.5% Cu) is the leading alternative to the traditional Sn-Pb solder eutectic alloy owing to its low melting temperature, better compatibility with other components, and excellent mechanical/structural properties. Numerous studies have discussed the mechanical and electrical properties of SAC305 in its bulk form. However, there has been limited research on SAC305 thin films, which differ significantly from bulk materials due to interfaces, stresses, thickness, microstructure, and underlying substrates. Furthermore, solder interconnects with increased roughness have reduced strength and a higher tendency for creep and can experience brittle fractures due to electric currents. Additionally, surface roughness adversely influences the solder's wetting properties. Thus, it is crucial to have a thin film solder that has a smooth, continuous, and void-free surface.

This study investigated a method to improve the surface morphology of SAC305 thin films. Depositing on various substrates, varying annealing processes, modulating magnetron sputtering parameters, and polishing techniques were used to achieve a smooth and continuous SAC305 thin film. Advanced characterization techniques were employed, including FE-SEM,

EDS, XRD, and AFM. Furthermore, the mechanical and electrical properties of both SAC305 bulk solder and thin film were analyzed using nanoindentation and the FPP method.

Increasing the substrate temperature affected the film's structure, with deterioration evident at higher temperatures. Annealing showed minimal film changes up to 210 °C, but significant alterations occurred at 220 °C. Despite these changes, the film's overall quality remained consistent, leading to a focus on non-annealed films and sputtering parameters. The deposition rate of SAC305 films increased with sputtering power due to enhanced ion-target interactions. However, as deposition pressure rose, the rate decreased due to more collisions between sputtered atoms and chamber ions. Films at lower pressures had a uniform grain structure, but higher pressures resulted in smaller grains and more voids. The results were due to the reduced energy of sputtered particles from increased collisions, leading to a porous film. The best SAC305 film quality was achieved using an RF power source at 200 watts and 2.4 mTorr pressure at room temperature.

SAC305 thin films on four substrates: silicon, gallium arsenide, sapphire, and glass were analyzed. Films on silicon, gallium arsenide, and sapphire had porous structures with interconnected nanoparticles. In contrast, those on glass had a rougher surface with voided nanoparticles, due to Sn's reduced wettability on glass. XRD patterns revealed polycrystalline β -Sn grains with no Ag peaks, indicating full alloying with the Sn layer. Despite weak Ag₃Sn peaks, Cu-related peaks were missing due to SAC305's low copper content. While silicon and gallium arsenide substrates showed specific peaks, sapphire and glass did not.

The film, deposited using an RF power source at 2.4 mTorr and 200 W on a Si substrate, was chosen for polishing due to its superior initial surface quality. Post-polishing, the film exhibited a uniform, robust, and continuous film. The polishing utilized abrasive SiO₂ particles,

which were later removed by ultrasonic cleaning with ethanol. While the AFM could not accurately measure the unpolished film's roughness, the polished sample showed a significant improvement, with roughness values of 16.9 nm (Ra) and 24.6 nm (Rq), underscoring the benefits of the polishing process.

The mechanical and electrical properties of the polished SAC305 thin film were compared to its bulk counterpart. Electrical tests showed that the thin film had a slightly higher resistivity, influenced by grain boundaries and underlying substrates. The strain rate sensitivity of the hardness was evaluated for SAC305 bulk and thin film samples using constant load indentation creep and CSM experiments. The average calculated (m) value $\approx 0.10 \pm 0.02$, of SAC305 thin film and bulk material agrees with literature data.

7.2 Future Work

Further research is essential to enhance the surface morphology of the thin film. The study indicated that increasing the negative substrate bias voltage during deposition can reduce the films' deposition rate, grain size, and surface roughness. However, the impact of this voltage varies based on the material and deposition method. Exploring the effects of opposing substrate (RF) biased voltage might further refine surface roughness. While this research focused on the SAC05 (96.5%Sn-3%Ag-0.5%Cu) thin film's surface morphology, crystallinity, and mechanical and electrical properties, future studies could examine SAC thin films with different compositions, such as 95.5Sn-3.8Ag-0.7Cu, 95.5Sn-3.9Ag-0.6Cu, and 95.5Sn-4Ag-0.5Cu. While the current study assessed properties at room temperature, consideration should be given to thin films exposed to higher temperatures during thermal cyclic loading. Understanding their properties under such conditions is vital.

REFERENCES

1. Suganuma, K. (2001). Advances in Lead-Free Electronics Soldering. *Current Opinion in Solid State and Materials Science*, 5(1), 55–64. [https://doi.org/10.1016/S1359-0286\(00\)00036-X](https://doi.org/10.1016/S1359-0286(00)00036-X)
2. Bellinger D. C. (2008). Very low lead exposures and children's neurodevelopment. *Current opinion in pediatrics*, 20(2), 172–177. <https://doi.org/10.1097/MOP.0b013e3282f4f97b>
3. European Union. (2003). Directive 2002/95/EC of the European Parliament and of the Council of January 27, 2003, on the restriction of the use of certain hazardous substances in electrical and electronic equipment. *Official Journal of the European Union*, L37, 19–23.
4. Abtew, M., & Selvaduray, G. (2000). Lead-Free Solders in Microelectronics. *Materials Science and Engineering*, 27, 95–141. [https://doi.org/10.1016/S0927-796X\(00\)00010-3](https://doi.org/10.1016/S0927-796X(00)00010-3)
5. Cheng, S., Huang, C. M., & Precht, M. (2017). A Review of Lead-Free Solders for Electronics Applications. *Microelectronics Reliability*, 75, 77–95. <https://doi.org/10.1016/j.microrel.2017.06.016>

6. L. M. Lee, A. A. Mohamad. (2013) Interfacial Reaction of Sn-Ag-Cu Lead-Free Solder Alloy on Cu: A Review. *Advances in Materials Science and Engineering*, 2013, 1-11. <http://dx.doi.org/10.1155/2013/123697>
7. Kim, K. S., Huh, S. H., & Sukanuma, K. (2003). Effects of Intermetallic Compounds on Properties of Sn–Ag–Cu Lead-Free Soldered Joints. *Journal of Alloys and Compounds*, 352(1–2), 226–236. [https://doi.org/10.1016/S0925-8388\(02\)01166-0](https://doi.org/10.1016/S0925-8388(02)01166-0)
8. Yoon, J. W., Kim, S. W., & Jung, S. B. (2005). IMC Morphology, Interfacial Reaction and Joint Reliability of Pb-Free Sn–Ag–Cu Solder on Electrolytic Ni BGA Substrate. *Journal of Alloys and Compounds*, 392(1–2), 247–252. <https://doi.org/10.1016/J.JALLCOM.2004.09.045>
9. Yu, D. Q., & Wang, L. (2008). The Growth and Roughness Evolution of Intermetallic Compounds of Sn–Ag–Cu/Cu Interface During Soldering Reaction. *Journal of Alloys and Compounds*, 458(1–2), 542–547. <https://doi.org/10.1016/J.JALLCOM.2007.04.047>
10. Yasmin, T., & Sadiq, M. (2014). Impact Of Lanthanum Doping on SAC305 Lead-Free Solders for High-Temperature Applications. *Journal of Engineering and Applied*, 33. <https://api.semanticscholar.org/CorpusID:136260930>
11. Kim, Y. R., Osmanson, A. T., Madanipour, H., Kim, C.-U., Thompson, P. F., & Chen, Q. (2020). Effects of UBM Thickness and Current Flow Configuration on Electromigration Failure Mechanisms in Solder Interconnects. *2020 IEEE International Reliability Physics Symposium (IRPS)*, 2020, 354-359. <https://doi.org/10.1109/irps45951.2020.9129337>
12. Lee, L. M., & Mohamad, A. A. (2013). Interfacial reaction of Sn-Ag-Cu lead-free solder alloy on Cu: A review. In *Advances in Materials Science and Engineering*, 2, 1-12. <https://doi.org/10.1155/2013/123697>

13. Rhee, H., Lucas, J. P., & Subramanian, K. N. (2002). Micromechanical Characterization of Thermomechanical Fatigued Lead-Free Solder Joints. *Journal of Materials Science: Materials in Electronics*, 13(8), 477–484.
<https://doi.org/10.1023/A:1016108120365/METRICS>
14. Lucas, J. P., Rhee, H., Guo, F., & Subramanian, K. N. (2003). Mechanical Properties of Intermetallic Compounds Associated with Pb-Free Solder Joints Using Nanoindentation. *Journal of Electronic Materials*, 32(12), 1375–1383. <https://doi.org/10.1007/S11664-003-0104-4/METRICS>
15. Sun, Y., Xu, Z. H., Li, X., Shanguan, D., & Liang, J. (2010). Mechanical Properties of Lead-Free Solder Alloy Measured by Nanoindentation. *2007 Proceedings of the ASME InterPack Conference, IPACK 2007* (2), 415–421. <https://doi.org/10.1115/IPACK2007-33988>
16. Gao, F., & Takemoto, T. (2006). Mechanical Properties Evolution of Sn-3.5Ag Based Lead-Free Solders by Nanoindentation. *Materials Letters*, 60(19), 2315–2318.
<https://doi.org/10.1016/J.MATLET.2005.12.132>
17. Chromik, R. R., Vinci, R. P., Allen, S. L., & Notis, M. R. (2003). Measuring the Mechanical Properties of Pb-Free Solder and Sn-Based Intermetallics by Nanoindentation. *The Journal of The Minerals, Metals & Materials Society*, 55(6), 66–69. <https://doi.org/10.1007/S11837-003-0144-5/METRICS>
18. Kelly, M. B., Maity, T., Nazmus Sakib, A. R., Frear, D. R., & Chawla, N. (2020). Influence of Substrate Surface Finish Metallurgy on Lead-Free Solder Joint Microstructure with Implications for Board-Level Reliability. *Journal of Electronic Materials*, 49(5), 3251–3258. <https://doi.org/10.1007/S11664-020-08013-0>

19. Peng, W., Monlevade, E., & Marques, M. E. (2007). Effect of Thermal Aging on The Interfacial Structure of SnAgCu Solder Joints on Cu. *Microelectronics Reliability*, 47(12), 2161–2168. <https://doi.org/10.1016/J.MICROREL.2006.12.006>
20. Cmglee, CC BY-SA 3.0 <<https://creativecommons.org/licenses/by-sa/3.0/>>, via Wikimedia Commons.
https://commons.wikimedia.org/wiki/File:Comparison_semiconductor_process_nodes.svg#file
21. Lau, J. H., & Pao, Y. H. (1997). *Solder Joint Reliability of BGA, CSP, Flip Chip, and Fine Pitch SMT Assemblies*. McGraw-Hill.
22. Sergei Gorbikov (<https://electronics.stackexchange.com/users/80820/sergei-gorbikov>), What's the difference between WLP and BGA (IC packages)?, URL (version: 2017-01-27). <https://electronics.stackexchange.com/q/282743>
23. Ulrich, R. K., & Brown, W. D. (2006). *Advanced Electronic Packaging*. Wiley-IEEE
24. Glazer, J. (1995). Metallurgy of low temperature Pb-free solders for electronic assembly. *International Materials Reviews*, 40, 65-93.
<https://api.semanticscholar.org/CorpusID:135552092>
25. Lea, C. (1988). *A scientific guide to surface mount technology*. Electrochemical Publications Ltd, 378-379. <https://api.semanticscholar.org/CorpusID:135855568>
26. ASM International. (1989). *Electronic Material Handbook*, ASM International 14, 1161-1162.
27. Lee, J. E., Kim, K. S., Inoue, M., Jiang, J., & Suganuma, K. (2008). Effects of Ag and Cu addition on microstructural properties and oxidation resistance of Sn–Zn eutectic alloy.

- Journal of Alloys and Compounds*, 454(1–2), 310-320.
<https://doi.org/10.1016/j.jallcom.2006.12.037>
28. Mei, Z., Morris, J.W. (1992). Superplastic creep of low melting point solder joints. *Journal of Electronic Materials* 21, 401–407. <https://doi.org/10.1007/BF02660403>
29. McCormack, M.T., Jin, S., Kammlott, G.W., & Chen, H.S. (1993). New Pb-free solder alloy with superior mechanical properties. *Applied Physics Letters*, 63, 15-17.
<https://api.semanticscholar.org/CorpusID:120748527>
30. McCormack, M.T., Jin, S.J., & Kammlott, G.W. (1995). The design of new, Pb-free solder alloys with improved properties. *Proceedings of the 1995 IEEE International Symposium on Electronics and the Environment ISEE (Cat. No.95CH35718)*, 171-176.
<https://api.semanticscholar.org/CorpusID:109734019>
31. Ventura, T., Terzi, S., Rappaz, M., & Dahle, A. K. (2011). Effects of solidification kinetics on microstructure formation in binary Sn–Cu solder alloys. *Acta Materialia*, 59(4), 1651-1658. <https://doi.org/10.1016/j.actamat.2010.11.032>
32. Van Vlack, L.H. (1970). *Materials Science for Engineers*. Addison-Wesley.
33. Hwang, J.S. (1989). *Solder Paste in Electronic Packaging*. Van Nostrand Reinhold.
34. Frear, D.R. (1996). The mechanical behavior of interconnect materials for electronic packaging. *Journal of Materials Science and Engineering* 48(3), 49-53.
<https://doi.org/10.1007/BF03222944>
35. Morris, J.W., Jr., Goldstein, J.L.F., & Mei, Z. (1993). Microstructure and mechanical properties of Sn-In and Sn-Bi solders. *Journal of Materials Science and Engineering* 45, 25-27. <https://doi.org/10.1007/BF03222376>

36. Darveaux, R., & Banerji, K. (1992). Constitutive relations for tin-based solder joints. *IEEE Transactions on Components, Hybrids, and Manufacturing Technology* 15(6), 1014-1022. <https://doi:10.1109/33.206925>.
37. Glazer, J. (1995). Metallurgy of low temperature Pb-free solders for electronic assembly. *International Materials Reviews*, 40, 65-93.
<https://api.semanticscholar.org/CorpID:135552092>
38. Strauss, R., & Smernos, S. (1984). Low Temperature Soldering. *Circuit World* 10, 23-25.
<https://api.semanticscholar.org/CorpusID:110350180>
39. Marshall, J.L., & Walter, S.R. (1987). *International Journal of Hybrid Microelectronics* 10, 11-17.
40. Thwaites, C. J. (1968). *Soft-solders and soldering in the electrical industry*. International Tin Research Institute.
41. Tin-Lead Eutectic Solder (63Sn-37Pb), Drop Solder (UNS L13630). (n.d). *Matweb*.
<https://www.matweb.com/search/datasheet.aspx?matguid=06a31d97bb734b509043d81cf131b280&ckck=1>
42. Tojima, K. (1999). Wetting Characteristics of Lead-free Solders, Materials Engineering Department, San Jose State University.
43. Lee, N.C., Slattery, J., Sovinsky, J., Artaki, I., & Vianco, P. (1995). *A novel lead-free solder replacement*. *Circuits Assembly*, 6(10), 36-44.
<https://api.semanticscholar.org/CorpusID:137940088>
44. Hua, F., & Glazer, J. (1997). Lead-free solders for electronic assembly, design, and reliability of solders and solder interconnections. *The Minerals, Metals and Materials Society*, 65-74.

45. Antimonial-Tin Solder (95Sn-5Sb), ASTM B 32 Grade S65 (UNS L13950). (n.d).
Matweb.
<https://www.matweb.com/search/DataSheet.aspx?MatGUID=afed5f7caae14509b505617128296bcc&ckck=1>
46. Minges, M. L. (1989). *Electronic Materials Handbook: Packaging, 1*, 640. ASM International.
47. Cook, B.A., Anderson, I.E., Harringa, J.L., & Kang, S.K. (2003). Isothermal aging of near-eutectic Sn-Ag-Cu solder alloys and its effect on electrical resistivity. *Journal of Electronic Materials*, 32, 1384-1391. <https://api.semanticscholar.org/CorpusID:94943248>
48. Wang, F., O'Keefe, M.J., & Brinkmeyer, B. (2009). Microstructural evolution and tensile properties of Sn-Ag-Cu mixed with Sn-Pb solder alloys. *Journal of Alloys and Compounds*, 477, 267-273. <https://api.semanticscholar.org/CorpusID:137470688>
49. Anderson, I.E., Cook, B.A., Harringa, J.L. et al. (2002). Sn-Ag-Cu solders and solder joints: Alloy development, microstructure, and properties. *Journal of Materials Science and Engineering*, 54, 26-29. <https://doi.org/10.1007/BF02701845>
50. El-Daly, A.A., El-Hosainy, H., Elmosalami, T.A., & Desoky, W.M. (2015). Microstructural modifications and properties of low-Ag-content Sn-Ag-Cu solder joints induced by Zn alloying. *Journal of Alloys and Compounds*, 653, 402-410.
<https://doi.org/10.1016/j.jallcom.2015.09.033>.
51. Manko, H. H. (1992). *Solders and soldering: Materials, design, production, and analysis for reliable bonding*. McGraw-Hill
52. He, S., Gao, R., Shen, YA., et al. (2020). Wettability, interfacial reactions, and impact strength of Sn-3.0Ag-0.5Cu solder/ENIG substrate used for fluxless soldering under

- formic acid atmosphere. *Journal of Materials Science and Engineering*, 55, 3107–3117.
<https://doi.org/10.1007/s10853-019-04153-9>.
53. Hua, F., Zhang, X., & Ma, H. (2008). Oxidation behavior of Sn–Ag–Cu lead-free solder. *Journal of Alloys and Compounds*, 450(1-2), 486-491.
<https://doi.org/10.3390/electronics12122709>
54. Ashby, M. F., & Jones, D. R. H. (2018). *Engineering Materials 1: An Introduction to Properties, Applications, and Design* (5th ed.). Elsevier
55. Lee, K.O., Yu, J., Park, T.S., & et al. (2004). Low-cycle fatigue characteristics of Sn-based solder joints. *Journal of Electronic Materials*, 33, 249–257.
<https://doi.org/10.1007/s11664-004-0130-x>
56. Smith, D. R., & Fickett, F. R. (1995). Low-Temperature Properties of Silver. *The Journal of Research of NIST*, 100(2), 119–171. <https://doi.org/10.6028/jres.100.012>.
57. Zeng, G., Xue, S., Zhang, L., et al. (2010). A review on the interfacial intermetallic compounds between Sn–Ag–Cu based solders and substrates. *Journal of Materials Science: Materials in Electronics*, 21(5), 421-440. [10.1007/s10854-010-0086-y](https://doi.org/10.1007/s10854-010-0086-y)
58. Guo, F., Choi, S., Lucas, J.P., et al. (2000). Effects of reflow on wettability, microstructure, and mechanical properties in lead-free solders. *Journal of Electronic Materials*, 29, 1241-1248. <https://doi.org/10.1007/s11664-000-0019-2>.
59. Miller, C.M., Anderson, I.E., & Smith, J.F. A viable tin-lead solder substitute: Sn-Ag-Cu. *Journal of Electronic Materials* 23, 595–601 (1994).
<https://doi.org/10.1007/BF02653344>
60. Caron, R.N. (2001). Copper: Alloying. In KH Jürgen Buschow, R.W. Cahn, M.C. Flemings, B. Ilshner, E.J. Kramer, S. Mahajan, & P. Veysière, *Encyclopedia of*

- Materials: Science and Technology*, 1652-1660. <https://doi.org/10.1016/B0-08-043152-6/00289-8>
61. Kang, S. K., et al. (2002). Interfacial reaction studies on lead (Pb)-free solder alloys. *IEEE Transactions on Electronics Packaging Manufacturing*, 25(3), 155-161. <https://doi.org/10.1109/TEPM.2002.801165>
62. Frear, D.R., Jang, J.W., Lin, J.K., et al. (2001). Pb-free solders for flip-chip interconnects. *The Journal of The Minerals, Metals & Materials Society*, 53(1), 28-33. <https://doi.org/10.1007/s11837-001-0099-3>
63. Choi, S., Lee, J.G., Guo, F., et al. (2001). Creep properties of Sn-Ag solder joints containing intermetallic particles. *The Journal of The Minerals, Metals & Materials Society*, 53(1), 22-26. <https://doi.org/10.1007/s11837-001-0098-4>.
64. Andersson, C., Lai, Z., Liu, J., Jiang, H., & Yu, Y. (2005). Comparison of isothermal mechanical fatigue properties of lead-free solder joints and bulk solders. *Materials Science and Engineering: A*, 394(1-2), 20-27. <https://doi.org/10.1016/j.msea.2004.10.043>
65. W. Kittidacha, A. Kanjanavikat, and K. Vattananiyom, "Effect of SAC Alloy Composition on Drop and Temp cycle Reliability of BGA with NiAu Pad Finish," 2008 10th Electronics Packaging Technology Conference, Singapore, 2008, 1074-1079. <https://doi:10.1109/EPTC.2008.4763572>.
66. Anderson, I. E., Cook, B. A., Haringa, J., Terpstra, R. L., Foley, J. C., & Unal, O. (2002). Effects of Alloying in Near-Eutectic Tin-Silver-Copper Solder Joints. *Materials Transactions*, 43(8), 1827-1832. <https://doi.org/10.2320/matertrans.43.1827>

67. Vinci, R. P., & Vlassak, J. J. (1996). Mechanical behavior of thin films. *Annual Review of Materials Science*, 26(1), 431-462.
<https://doi.org/10.1146/annurev.ms.26.080196.002243>
68. Rodríguez Pulecio, S. A., Moré Farias, M. C., & Souza, R. M. (2010). Finite element and dimensional analysis algorithm for the prediction of mechanical properties of bulk materials and thin films. *Surface and Coatings Technology*, 205(5), 1386-1392.
<https://doi.org/10.1016/j.surfcoat.2010.07.039>
69. Rupp, J. L. M., & Gauckler, L. J. (2006). Microstructures and electrical conductivity of nanocrystalline ceria-based thin films. *Solid State Ionics*, 177(26–32), 2513-2518.
<https://doi.org/10.1016/j.ssi.2006.07.033>
70. Ding, X., Ko, W. H., & Mansour, J. M. (1990). Residual stress and mechanical properties of boron-doped p+-silicon films. *Sensors and Actuators A: Physical*, 23(1–3), 866-871.
[https://doi.org/10.1016/0924-4247\(90\)87048-N](https://doi.org/10.1016/0924-4247(90)87048-N)
71. Rossnagel, S. M. (2020). Magnetron sputtering. *Journal of Vacuum Science & Technology A*, 38(6). <https://doi.org/10.1116/6.0000594>
72. Kukla, R., Krug, T.G., Ludwig, R., & Wilmes, K. (1990). A highest rate self-sputtering magnetron source. *Vacuum*, 41, 1968-1970.
[https://doi.org/10.1016/0042-207X\(90\)94147-I](https://doi.org/10.1016/0042-207X(90)94147-I)
73. Almeida, J.B. (1989). Design of magnetrons for dc sputtering. *Vacuum*, 39(7–8), 717-721. [https://doi.org/10.1016/0042-207X\(89\)90023-7](https://doi.org/10.1016/0042-207X(89)90023-7).
74. Wasa, K. (2012). *Handbook of Sputter Deposition Technology: Fundamentals and Applications for Functional Thin Films, Nanomaterials and MEMS*. William Andrew. 114-116.

75. Almeida, J.B. (1989). Design of magnetrons for dc sputtering. *Vacuum*, 39(7–8), 717-721. [https://doi.org/10.1016/0042-207X\(89\)90023-7](https://doi.org/10.1016/0042-207X(89)90023-7).
76. Baig, N., Kammakakam, I., & Falath, W. (2021). Nanomaterials: A review of synthesis methods, properties, recent progress, and challenges. *Materials Advances*, 2(6), 1821-1871. <https://doi.org/10.1039/D0MA00807A>
77. Ellmer, K. (2000). Magnetron sputtering of transparent conductive zinc oxide: relation between the sputtering parameters and the electronic properties. *Journal of Physics D: Applied Physics*, 33(4), R17. <https://doi.org/10.1088/0022-3727/33/4/201>
78. Scherer, M., Schmitt, J., Latz, R., & Schanz, M. (1992). Reactive alternating current magnetron sputtering of dielectric layers. *Journal of Vacuum Science & Technology A: Vacuum, Surfaces, and Films*, 10(4), 1772-1776.
79. Kelly, P.J., Abu-Zeid, O.A., Arnell, R.D., & Tong, J. (1996). The deposition of aluminium oxide coatings by reactive unbalanced magnetron sputtering. *Surface and Coatings Technology*, 86–87(1), 28-32. [https://doi.org/10.1016/S0257-8972\(96\)02997-0](https://doi.org/10.1016/S0257-8972(96)02997-0).
80. Henderson, P. S., Kelly, P. J., & Arnell, R. D. (1999, April). Optimizing the deposition conditions for reactively pulsed magnetron sputtered oxide" lms. In *International Conference on Metallic Coatings and Thin Films, ICMCTF99, San Diego, April* (Vol. 12, p. 15).
81. Bruslind, L. (2019). *General Microbiology* (pp. 10-20). Oregon State University. Retrieved from [Microscopes – General Microbiology \(oregonstate.education\)](https://www.oregonstate.edu/microscopes-general-microbiology)
82. Zhou, W., Apkarian, R., Wang, Z.L., & Joy, D. (2006). Fundamentals of Scanning Electron Microscopy (SEM). In W. Zhou & Z.L. Wang (Eds.), *Scanning Microscopy for Nanotechnology* (pp. 1-40). Springer. https://doi.org/10.1007/978-0-387-39620-0_1

83. Kanaya, K., & Okayama, S. (1972). Penetration and energy-loss theory of electrons in solid targets. *Journal of Physics D: Applied Physics*, 5(1), 43.
<https://doi.org/10.1088/0022-3727/5/1/308>
84. Stoddart, C. (2022, March 1). Structural biology: How proteins got their close-up. *Knowable Magazine*. <https://doi.org/10.1146/knowable-022822-1>
85. Friedrich, W., Knipping, P., & von Laue, M. (1912). Interferenz-Erscheinungen bei Röntgenstrahlen. *Sitzungsberichte der Mathematisch-Physikalischen Classe der Königlich-Bayerischen Akademie der Wissenschaften zu München*, 303.
86. Chauhan, A., & Chauhan, P. (2014). Powder XRD technique and its applications in science and technology. *Journal of Analytical & Bioanalytical Techniques*, 5(5), 1-5.
<https://doi.org/10.4172/2155-9872.1000212>
87. DrBoStefanov. (2020). Drawing of an XRD diffractometer in grazing incidence x-ray diffraction configuration [Image]. Wikimedia Commons.
https://upload.wikimedia.org/wikipedia/commons/0/06/XRD_diffractometer.svg
88. Martin, Y., Williams, C. C., & Wickramasinghe, H. K. (1987). Atomic force microscope–force mapping and profiling on a sub 100-Å scale. *Journal of Applied Physics*, 61(10), 4723-4729. <https://doi.org/10.1063/1.338807>
89. Yashvant. (2013). Typical atomic force microscope (AFM) setup [Image, CC-BY-2.5]. Opensource Handbook of Nanoscience and Nanotechnology. Wikimedia Commons.
<https://upload.wikimedia.org/wikipedia/commons/5/5e/AFMsetup.jpg>
90. Zhong, Q., Inniss, D., Kjoller, K., & Elings, V. B. (1993). Fractured polymer/silica fiber surface studied by tapping mode atomic force microscopy. *Surface Science Letters*, 290(1-2), 688-692. [https://doi.org/10.1016/0167-2584\(93\)90906-Y](https://doi.org/10.1016/0167-2584(93)90906-Y)

91. Albrecht, T. R., Grütter, P., Horne, D., & Rugar, D. (1991). Frequency modulation detection using high-Q cantilevers for enhanced force microscope sensitivity. *Journal of Applied Physics*, 69(2), 668-673. <https://doi.org/10.1063/1.347347>
92. Liu, K., Ostadhassan, M., & Bubach, B. (2016). Applications of nano-indentation methods to estimate nanoscale mechanical properties of shale reservoir rocks. *Journal of Natural Gas Science and Engineering*, 35, 1310-1319. <https://doi.org/10.1016/j.jngse.2016.09.068>
93. Kontomaris, S. V. (2018). The Hertz model in AFM nanoindentation experiments: applications in biological samples and biomaterials. *Micro and Nanosystems*, 10(1), 11-22. <https://doi.org/10.2174/1876402910666180426114700>
94. Van Helvert, S., & Friedl, P. (2016). Strain stiffening of fibrillar collagen during individual and collective cell migration identified by AFM nanoindentation. *ACS applied materials & interfaces*, 8(34), 21946-21955. <https://doi.org/10.1021/acsami.6b01755>
95. Pharr, G. M., & Cook, R. F. (1990). Instrumentation of a conventional hardness tester for load-displacement measurement during indentation. *Journal of Materials Research*, 5, 847-851. <https://doi.org/10.1557/JMR.1990.0847>
96. Oliver, W. C., & Pharr, G. M. (2004). Measurement of hardness and elastic modulus by instrumented indentation: Advances in understanding and refinements to methodology. *Journal of Materials Research*, 19(1), 3-20. <https://doi.org/10.1557/jmr.2004.19.1.3>
97. Oliver, W. C., & Pharr, G. M. (1992). An improved technique for determining hardness and elastic modulus using load and displacement sensing indentation experiments. *Journal of Materials Research*, 7(6), 1564-1583. <https://doi.org/10.1557/JMR.1992.1564>

98. Meyers, M. A., & Chawla, K. K. (2009). *Mechanical Metallurgy Principles and Applications* (2nd ed.). Cambridge University Press.
<http://www.cambridge.org/9780521866750>
99. Argon, A. S., Backer, S., McClintock, F. A., & Reichenbach, G. S. (1966). *Mechanical behavior of materials*. Addison-Wesley Publishing Co., Inc.; Reading, MA.
100. Meyer, E. (1908). Hardness testing and hardness. *VDI Zeitschrift*, 52, 645-654.
101. Nicoguardo. (2020). Schematic of a load-displacement curve for nanoindentation [Image].
[Wikipedia.https://upload.wikimedia.org/wikipedia/commons/6/6c/Load_disp_indentation.svg](https://upload.wikimedia.org/wikipedia/commons/6/6c/Load_disp_indentation.svg)
102. Wells, J. W., Kallehauge, J. F., & Hofmann, P. (2007). Thermal switching of the electrical conductivity of Si (111) Ag due to a surface phase transition. *Journal of Physics: Condensed Matter*, 19(17), 176008. <https://doi.org/10.1088/0953-8984/19/17/176008>
103. Thorsteinsson, S., Wang, F., Petersen, D. H., Hansen, T. M., Kjær, D., Lin, R., ... & Hansen, O. (2009). Accurate microfour-point probe sheet resistance measurements on small samples. *Review of Scientific Instruments*, 80(5). <https://doi.org/10.1063/1.3125050>
104. SpinningSpark. (2009, November 30). Arrangement of probes in a Wenner electrode array [Image]. Inkscape. https://en.wikipedia.org/wiki/File:Wenner_electrode_array.svg
105. Hofmann, P., & Wells, J. W. (2008). Surface-sensitive conductance measurements. *Journal of Physics: Condensed Matter*, 21(1), 013003. <https://doi.org/10.1088/0953-8984/21/1/013003>

106. Baptista, A., Silva, F., Porteiro, J., Míguez, J., & Pinto, G. (2018). Sputtering physical vapour deposition (PVD) coatings: A critical review on process improvement and market trend demands. *Coatings*, 8(11), 402. <https://doi.org/10.3390/coatings8110402>
107. Hogmark, S., Jacobson, S., & Larsson, M. (2000). Design and evaluation of tribological coatings. *Wear*, 246(1-2), 20-33. [https://doi.org/10.1016/S0043-1648\(00\)00505-6](https://doi.org/10.1016/S0043-1648(00)00505-6)
108. Chan, K. Y., & Teo, B. S. (2005). Sputtering power and deposition pressure effects on the electrical and structural properties of copper thin films. *Journal of materials science*, 40, 5971-5981. <https://doi.org/10.1007/s10853-005-1362-8>
109. Shah, H. N., Jayaganthan, R., & Kaur, D. (2010). Effect of sputtering pressure and temperature on DC magnetron sputtered CrN films. *Surface Engineering*, 26(8), 629-637. <https://doi.org/10.1179/174329409X389326>
110. Freund, L. B., & Suresh, S. (2004). *Thin film materials: stress, defect formation and surface evolution*. Cambridge university press.
111. González-González, A., Alonzo-Medina, G. M., Oliva, A. I., Polop, C., Sacedón, J. L., & Vasco, E. (2011). Morphology evolution of thermally annealed polycrystalline thin films. *Physical Review B*, 84(15), 155450. <https://doi.org/10.1103/PhysRevB.84.155450>
112. Abbas, N., Shad, M. R., Hussain, M., Mehdi, S. M. Z., & Sajjad, U. (2019). Fabrication and characterization of silver thin films using physical vapor deposition, and the investigation of annealing effects on their structures. *Materials Research Express*, 6(11), 116437. <https://doi.org/10.1088/2053-1591/ab4c4f>
113. Liu, W. J., Chang, Y. H., Chiang, C. C., Chen, Y. T., Wang, Y. Z., Wu, C. L., & Ou, S. L. (2023). Thickness, Annealing, and Surface Roughness Effect on Magnetic and

- Significant Properties of Co₄₀Fe₄₀B₁₀Dy₁₀ Thin Films. *Materials*, 16(17), 5995.
<https://doi.org/10.3390/ma16175995>
114. Kern, W. (1990). The evolution of silicon wafer cleaning technology. *Journal of the Electrochemical Society*, 137(6), 1887. <https://doi.org/10.1149/1.2086825>
115. Ma, Z. L., & Gourlay, C. M. (2017). Nucleation, grain orientations, and microstructure of Sn-3Ag-0.5 Cu soldered on cobalt substrates. *Journal of Alloys and Compounds*, 706, 596-608. <https://doi.org/10.1016/j.jallcom.2017.02.243>
116. Pradhan, G., Dey, P. P., & Sharma, A. K. (2020). Growth dynamics of pulsed laser deposited WS₂ thin films on different substrates. *Applied Physics A*, 126, 1-7.
<https://doi.org/10.1007/s00339-020-03650-y>
117. Saha, R., & Nix, W. D. (2002). Effects of the substrate on the determination of thin film mechanical properties by nanoindentation. *Acta materialia*, 50(1), 23-38.
[https://doi.org/10.1016/S1359-6454\(01\)00328-7](https://doi.org/10.1016/S1359-6454(01)00328-7)
118. Thanikaikarasan, S., Mahalingam, T., Ahamad, T., & Alshehri, S. M. (2020). Role of substrate on film thickness, structural, compositional and magnetic properties of CoNi thin alloy films by low temperature electrodeposition technique. *Journal of Saudi Chemical Society*, 24(12), 955-962. <https://doi.org/10.1016/j.jscs.2020.10.003>
119. Sburlan, I. C., Vasile, I., & Tudor, E. (2021, October). Comparative study between semiconductor power devices based on silicon Si, silicon carbide SiC and gallium nitrate GaN used in the electrical system subassembly of an electric vehicle. In *2021 International Semiconductor Conference (CAS)* (pp. 107-110). IEEE.
<https://doi.org/10.1109/CAS52836.2021.9604127>

120. Tanaka, A. (2004). Toxicity of indium arsenide, gallium arsenide, and aluminium gallium arsenide. *Toxicology and applied pharmacology*, *198*(3), 405-411.
<https://doi.org/10.1016/j.taap.2003.10.019>
121. Akselrod, M. S., & Bruni, F. J. (2012). Modern trends in crystal growth and new applications of sapphire. *Journal of crystal growth*, *360*, 134-145.
<https://doi.org/10.1016/j.jcrysgr.2011.12.038>
122. Nguyen, T. T. N., Sasaki, M., Tsutsumi, T., Ishikawa, K., & Hori, M. (2020). Formation of spherical Sn particles by reducing SnO₂ film in floating wire-assisted H₂/Ar plasma at atmospheric pressure. *Scientific Reports*, *10*(1), 17770. <https://doi.org/10.1038/s41598-020-74663-z>
123. Kazani, I., De Mey, G., Hertleer, C., Banaszczyk, J., Schwarz, A., Guxho, G., & Van Langenhove, L. (2013). About the collinear four-point probe technique's inability to measure the resistivity of anisotropic electroconductive fabrics. *Textile Research Journal*, *83*(15), 1587-1593. <https://doi.org/10.1177/0040517512452951>
124. Kanagawa, T., Hobara, R., Matsuda, I., Tanikawa, T., Natori, A., & Hasegawa, S. (2003). Anisotropy in conductance of a quasi-one-dimensional metallic surface state measured by a square micro-four-point probe method. *Physical Review Letters*, *91*(3), 036805.
<https://doi.org/10.1103/PhysRevLett.91.036805>
125. Thorsteinsson, S., Wang, F., Petersen, D. H., Hansen, T. M., Kjær, D., Lin, R., ... & Hansen, O. (2009). Accurate microfour-point probe sheet resistance measurements on small samples. *Review of Scientific Instruments*, *80*(5). <https://doi.org/10.1063/1.3125050>

126. Sundgren, J. E., & Hentzell, H. G. (1986). A review of the present state of art in hard coatings grown from the vapor phase. *Journal of Vacuum Science & Technology A: Vacuum, Surfaces, and Films*, 4(5), 2259-2279. <https://doi.org/10.1116/1.574062>
127. Cammarata, R. C., Schlesinger, T. E., Kim, C., Qadri, S. B., & Edelstein, A. S. (1990). Nanoindentation study of the mechanical properties of copper-nickel multilayered thin films. *Applied Physics Letters*, 56(19), 1862-1864. <https://doi.org/10.1063/1.103070>
128. Stegall, D. E., & Elmustafa, A. A. (2018). The contribution of dislocation density and velocity to the strain rate and size effect using transient indentation methods and activation volume analysis. *Metallurgical and Materials Transactions A*, 49, 4649-4658. <https://doi.org/10.1007/s11661-018-4817-7>
129. Elmustafa, A. A., & Stone, D. S. (2007). Strain rate sensitivity in nanoindentation creep of hard materials. *Journal of Materials Research*, 22(10), 2912-2916. <https://doi.org/10.1557/JMR.2007.0374>
130. Kariya, Y., & Plumbridge, W. J. P. W. J. (2001, February). Mechanical properties of Sn-3.0 mass% Ag-0.5 mass% Cu alloy. In *Proc. of the 7th Symposium on Microjoining and Assembly Technology in Electronics* (Vol. 7, pp. 383-388).
131. Mysore, K., Subbarayan, G., Gupta, V., & Zhang, R. (2009). Constitutive and aging behavior of Sn3.0Ag0.5Cu solder alloy. *IEEE Transactions on Electronics Packaging Manufacturing*, 32(4), 221-232. <https://doi.org/10.1109/TEPM.2009.2024119>
132. Nix, W. D. (1989). Mechanical properties of thin films. *Metallurgical Transactions A*, 20, 2217-2245. <https://doi.org/10.1007/BF02666659>
133. Heremans, P., Tripathi, A. K., de Jamblinne de Meux, A., Smits, E. C., Hou, B., Pourtois, G., & Gelinck, G. H. (2016). Mechanical and electronic properties of thin-film transistors

- on plastic, and their integration in flexible electronic applications. *Advanced Materials*, 28(22), 4266-4282. <https://doi.org/10.1002/adma.201504360>
134. Cook, B. A., Anderson, I. E., Harringa, J. L., & Terpstra, R. L. (2002). Effect of heat treatment on the electrical resistivity of near-eutectic Sn-Ag-Cu Pb-free solder alloys. *Journal of Electronic Materials*, 31, 1190-1194. <https://doi.org/10.1007/s11664-002-0009-7>
135. Gain, A. K., & Zhang, L. (2019). Effects of Ni nanoparticles addition on the microstructure, electrical and mechanical properties of Sn-Ag-Cu alloy. *Materialia*, 5, 100234. <https://doi.org/10.1016/j.mtla.2019.100234>
136. Ismail, N., Jalar, A., Afdzaluddin, A., & Bakar, M. A. (2021). Electrical resistivity of Sn–3.0 Ag–0.5 Cu solder joint with the incorporation of carbon nanotubes. *Nanomaterials and Nanotechnology*, 11. <https://doi.org/10.1177/1847980421996539>

APPENDIX A

COPYRIGHT PERMISSIONS

The material presented in Chapters Five and Six of this dissertation is sourced from works published in the following journals. The copyright holders have granted permission for publication.

Ojha, M., Mohammed, Y., Stone, D. S., & Elmustafa, A. A. (2023). Microstructure, creep properties, and electrical resistivity of magnetron sputtering deposited SAC305 thin films.

Journal of Vacuum Science & Technology B, 41(5), 052205. <https://doi.org/10.1116/6.0002949>

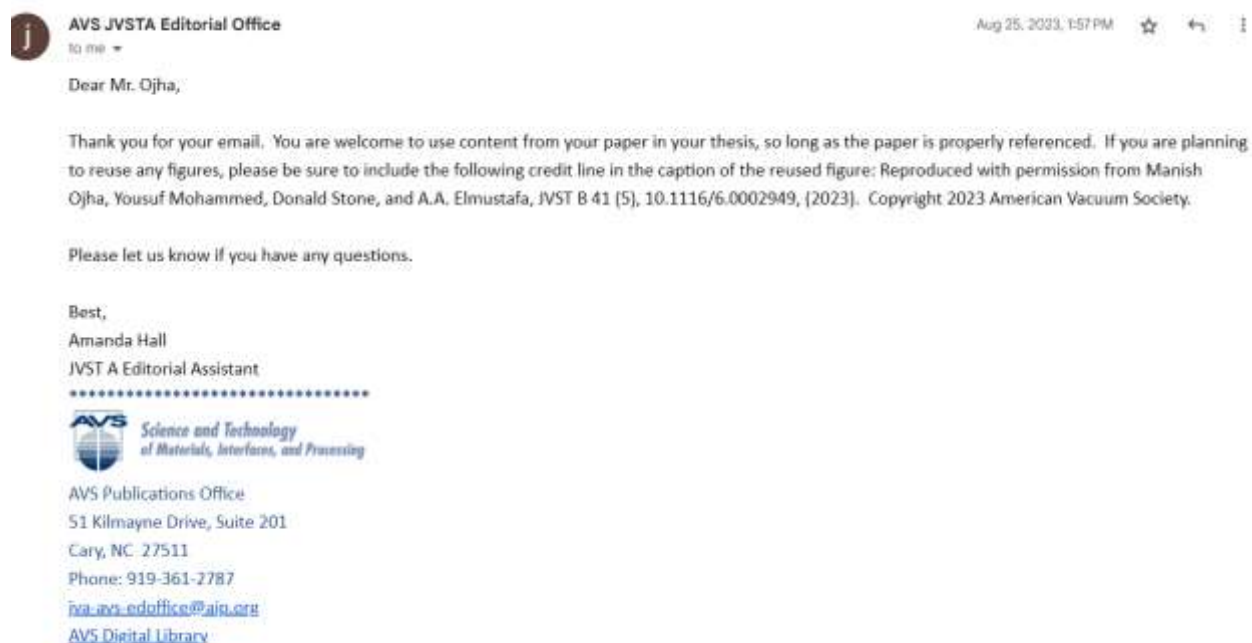


Figure A1 Permission to use figures in chapter 5 and 6

Permission to use Figures 1.1, 2.1, 3.2, 3.3, 3.4, 3.5, 3.6, and 3.7 from

<https://creativecommons.org/licenses/by/3.0/>

8/21/23, 7:05 PM

Creative Commons — Attribution-ShareAlike 3.0 Unported — CC BY-SA 3.0

This page is available in the following languages:



Creative Commons License De
Attribution-ShareAlike 3.0 Unported (CC BY-SA 3.0)



This is a human-readable summary of (and not a substitute for) the [license](#).

You are free to:

Share — copy and redistribute the material in any medium or format

Adapt — remix, transform, and build upon the material

for any purpose, even commercially.

The licensor cannot revoke these freedoms as long as you follow the license terms.

Under the following terms:



Attribution — You must give appropriate credit, provide a link to the license, and indicate if changes were made. You may do so in any reasonable manner, but not in any way that suggests the licensor endorses you or your use.



ShareAlike — If you remix, transform, or build upon the material, you must distribute your contributions under the same license as the original.

No additional restrictions — You may not apply legal terms or technological measures that legally restrict others from doing anything the license permits.

Notices:

You do not have to comply with the license for elements of the material in the public domain or where your use is permitted by an applicable exception or limitation.

No warranties are given. The license may not give you all of the permissions necessary for your intended use. For example, other rights such as publicity, privacy, or moral rights may limit how you use the material.

<https://creativecommons.org/licenses/by-sa/3.0/deed.en>

1/1

Figure A2 Permission to use Figures 1.1, 2.1, 3.2, 3.3, 3.4, 3.5, 3.6, and 3.7

VITA

Manish Ojha
 Department of Mechanical and Aerospace Engineering
 The Applied Research Center-Thomas Jefferson National Accelerator Facility
 Old Dominion University
 Norfolk, VA 23529

EDUCATION

- Ph.D. in Mechanical Engineering, Old Dominion University, Norfolk, VA, USA, 2021 – 2023.
- M.Sc. in Mechanical Engineering, Grand Valley State University, Grand Rapids, MI, USA, 2018 – 2020.
- B.Sc. in Mechanical Engineering, Kurukshetra University, India, 2012 – 2016.

JOURNAL PUBLICATIONS

- Ojha, M., Mohammed, Y., Stone, D. S., & Elmustafa, A. A. (2023). Microstructure, creep properties, and electrical resistivity of magnetron sputtering deposited SAC305 thin films. *Journal of Vacuum Science & Technology B*, 41(5), 052205. <https://doi.org/10.1116/6.0002949>
- Ojha, M., Al-Allaq, A. H., Mohammed, Y., Bhukya, S. N., Wu, Z., & Elmustafa, A. A. (2023). Elastic properties of the non-mixing copper donor-assisted material in friction stir welding of aluminum alloys using nanoindentation. *Frontiers in Metals and Alloys*, 2, 1129126. <https://doi.org/10.3389/ftmal.2023.1129126>
- Bhukya, S. N., Wu, Z., Elmustafa, A.A., Al-Allaq, A., Ojha, M., & Mohammed, Y. (2023). Cu donor material assisted friction stir welding of AA2024 and AA6061 dissimilar alloys: Effect on the downward force, temperature profile, and mechanical properties. *The International Journal of Advanced Manufacturing Technology*, 127, 3839–3851. <https://doi.org/10.1007/s00170-023-11778-3>
- Al-Allaq, A., Ojha, M., Mohammed, Y., Bhukya, S. N., Wu, Z., & Elmustafa, A.A. (2023) Post Weld Heat Treatment Effects on Microstructure, Crystal Structure, and Mechanical Properties of Donor Stir Assisted Friction Stir Welding Material of AA6061-T6 Alloy, *International Journal of Advanced Manufacturing Technology* [Preprint]. <https://doi.org/10.21203/rs.3.rs-2720330/v1>

AWARDS

- The first prize winner of the Mid-Atlantic chapter student poster competition held by the American Vacuum Society (AVS).
- Prabhu Endowed Graduate Scholarship in Mechanical Engineering.